SUPERHEAT CONTROL FOR AIR CONDITIONING AND REFRIGERATION SYSTEMS:

SIMULATION AND EXPERIMENTS

BY

RICHARD JAMES OTTEN

THESIS

Submitted in partial fulfillment of the requirements
for the degree of Master of Science in Mechanical Engineering
in the Graduate College of the
University of Illinois at Urbana-Champaign, 2010

Urbana, Illinois

Advisor:

Professor Andrew Alleyne

Abstract

Ever since the invention of air conditioning and refrigeration in the late nineteenth century, there has been tremendous interest in increasing system efficiency to reduce the impact these systems have on global energy consumption. Efficiency improvements have been accomplished through component design, refrigerant design, and most recently control system design. The emergence of the electronic expansion valve and variable speed drives has made immense impacts on the ability to regulate system parameters, resulting in important strides towards efficiency improvement.

This research presents tools and methodologies for model development and controller design for air conditioning and refrigeration systems. In this thesis, control-oriented nonlinear dynamic models are developed and validated with test data collected from a fully instrumented experimental system. These models enable the design of advanced control configurations which supplement the performance of the commonly used proportional-integral-derivative (PID) controller. Evaporator superheat is a key parameter considered in this research since precise control optimizes evaporator efficiency while protecting the system from component damage. The controllers developed in this thesis ultimately provide better transient and steady state performance which increases system efficiency through low superheat set point design. The developed controllers also address the classical performance versus robustness tradeoff through design which preserves transients while prolonging the lifetime of the electronic expansion valve. Another notable contribution of this thesis is the development of hardware-in-the-loop load emulation which provides a method to test component and software control loop performance. This method alleviates the costs associated with the current method of testing using environmental test chambers.

To my friends and family

Acknowledgements

The contributions of this thesis were made possible by a countless number of individuals. First and foremost, I would like to thank the unwavering support of my family. I would like to thank my parents for supporting me with each decision I have made. I am very grateful for their encouragement and inspiration. I want to thank my sisters Erica and Margot for teaching me life-long lessons while growing up. I also want to thank my brother Russ who has always been right next to me to face the next challenge. All three of you serve as great examples to live by. I would also like to thank Dawn for all of her encouragement and support. Without this amazing group of people I would not be in such a great position.

I would like to thank my advisor, Professor Andrew Alleyne, for inviting me to join the Alleyne Research Group. His guidance and mentorship over the past two years has been fundamental to my success as a researcher and professional. The Alleyne Research Group (ARG) has been an outstanding place to study over the course of my graduate program. The ARG is filled with extremely talented people who are passionate about engineering and science. Creative insight into even the most basic problems can always be found within this group.

During my time in the Alleyne Research Group I benefited greatly from the knowledge of my lab mates. I would like thank: Sandipan Mishra, Kira Barton - and Alex Shorter - for their valuable experience and guidance, Dave Hoelzle for the humor he brought into lab every morning, and Tim Deppen for his engineering insight. Thanks, also, to those I collaborated with most, Neera Jain for the engaging discussions we had on research and science, Bin Li for teaching me how to operate the experimental system while also providing insight to research tools, and Vikas Chandan for teaching me to realize the larger impact projects have. Our discussions have served to inspire creativity in all of our work. I also want to thank Tom Mckinley for his insight during the short duration our time in the lab overlapped. I have enjoyed

my time with Yangmin Xie, Nanjun Liu, and Erick Sutanto who I have gotten to know well through classes and research. I want to wish everyone in the ARG the best of luck in all future endeavors.

Table of Contents

Chapter 1

Introduction

The invention of air conditioning and refrigeration (AC&R) in the late nineteenth century has contributed to the higher standard of living that we are provided with today [1]. Everyday, society relies on air conditioning systems for human comfort whether it is in our homes, offices, or automobiles. Refrigeration systems have also transformed the way we live. For example, these systems allow perishable goods to be transported spatially throughout the world which would otherwise be nearly impossible. These few examples are among a countless list of applications which rely on AC&R systems.

Systems that use vapor compression cycles, such as air conditioners and refrigerators, account for significant portions of the overall energy consumption of industrial, commercial, and residential applications. According to a study released in 2005, 33.2% of residential energy consumption and 34% of commercial energy consumption is from cooling and refrigeration [2]. This study has also reported that the average household spends about $1800 a year on air conditioning and refrigeration alone. Without doubt, air conditioning and refrigeration systems have made an enormous impact on our society and will continue to do so into the foreseeable future.

Since the development of the first AC&R systems there has been tremendous interest in improving the efficiency of the vapor compression cycle (VCC). Past research efforts have focused on investigating the effects of refrigerant type, heat exchanger design, component design, and more recently control system design.

Improved efficiency of vapor compression systems may be realized through advanced control design [3],[4]. As sensors, computers, and actuators become more cost effective,

electronic system control is increasingly more practical for implementation on AC&R systems. Research in this field focuses on determining methods to best use sensor information to control system parameters during system-wide operation. The ability to precisely control system parameters improves efficiency while also extending the systems lifetime since harmful operating conditions can be avoided [5].

This thesis makes contributions to both evaporator superheat control design and the development of an alternative AC&R testing method. Evaporator superheat is a key parameter in the vapor compression cycle that is controlled to maximize evaporator efficiency while protecting the system from component damage. A goal of this research is to identify, examine, and further develop the state of the art evaporator superheat control configuration.

Another significant contribution of this thesis is the development of hardware-in-the-loop load emulation which provides an alternative method for testing AC&R systems. This method has been developed to test control algorithms and system performance to conditions that are representative of environments that the AC&R system may be subjected to while operating in the field. This method provides a flexible environment for testing with a reduced need for full scale environmental test chambers.

The remainder of this chapter is organized as follows. Section 1.1 discusses the basic operation of the vapor compression cycle. Section 1.2 summarizes the vapor compression system control objectives. Hardware-in-the-loop load emulation is discussed in Section 1.3. Finally, the organization of this thesis is presented in Section 1.4.

1.1   Vapor Compression Cycle

The vapor compression cycle transfers heat from a lower temperature region to a higher temperature one through the compression and expansion of a working fluid referred to as refrigerant. The basic vapor compression cycle consists of four main components: a compressor, a condenser, an expansion device, and an evaporator. Figure 1.1 presents the vapor compression cycle component configuration where heat is transferred from the cooled space to the surrounding environment through the refrigerant. Figure 1.2 presents the pressure-enthalpy diagram of the basic vapor compression cycle where the numbered points correspond to those in Figure 1.1.
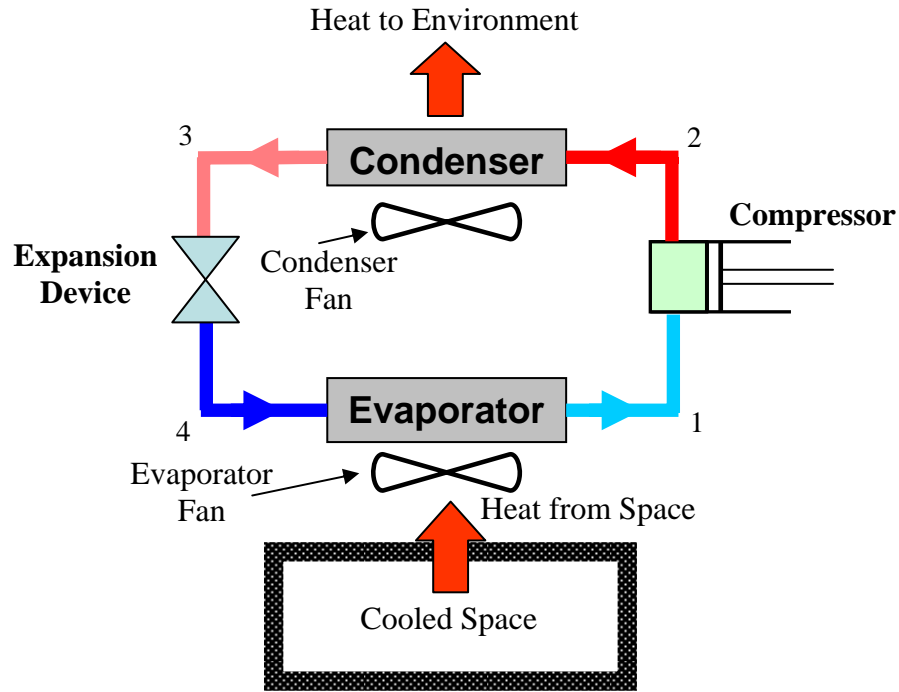
Figure 1.1   Vapor compression cycle diagram

A short description of the VCC is given here. The refrigerant enters the compressor in a completely vaporized state referred to as a superheated state.   The refrigerant exits the compressor at a much higher pressure and temperature. The high-pressure, high-temperature vaporized refrigerant enters the condenser where heat is rejected to the surrounding environment. As the vaporized refrigerant rejects heat to the surrounding environment it begins to condense and exits the condenser in a liquid form.   The refrigerant, in a liquid state, then enters the expansion device where the pressure significantly decreases. The decrease in pressure causes the temperature to also decrease significantly. The refrigerant enters the evaporator in a two phase form, consisting of liquid and vaporized refrigerant.   The low-pressure, low-temperature refrigerant absorbs heat from the cooled space, boiling as it flows through the evaporator. In the ideal cycle the refrigerant is completely vaporized at the exit of the evaporator. The vaporized refrigerant then enters the compressor and the cycle repeats.
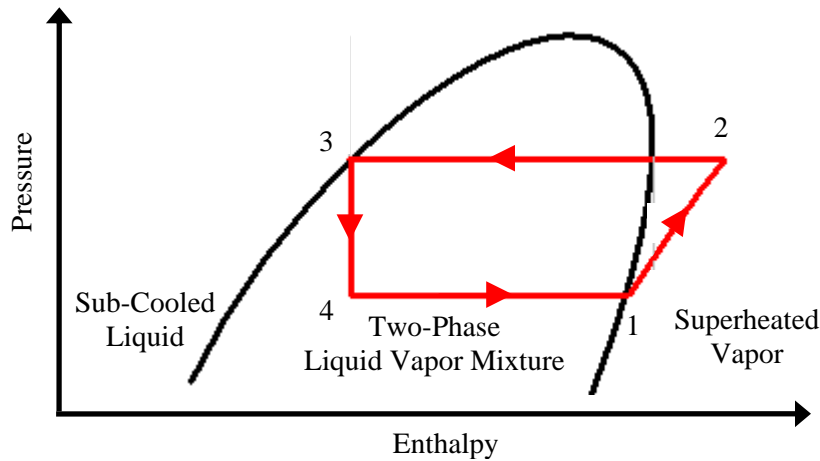
Figure 1.2   P-h diagram for the ideal vapor compression cycle

The vapor compression cycle illustrated in Figure 1.1 presents only the components of the basic cycle. Additional components are used in certain applications to improve system performance and prevent component damage. An accumulator is one common component that is used in some AC&R systems. An accumulator ensures that the refrigerant entering the compressor is completely vaporized to minimize the risk of liquid refrigerant damaging the compressor. A receiver is another component that is used in some AC&R systems. This device is placed in the refrigerant flow path between the condenser and the expansion device to ensure the refrigerant entering the expansion device is in a completely saturated state. A liquid line heat exchanger is another component used in some systems to sub cool the refrigerant entering the expansion device and to further heat the superheated vapor entering the compressor.

1.2   Control of Vapor Compression Systems

Vapor compression systems consume large amounts of electricity which make it essential for these systems to meet their cooling objectives as efficiently as possible. The vapor compression systems must accomplish this even during fluctuating environmental conditions, loads, and user set points. Historically, system capacity has been controlled with on-off operation, where the compressor is turned on and off to meet the temperature demands set by the user. With the emergence of variable speed compressors, higher efficiency cooling is possible due to better load matching [6],[4]. These studies have shown that variable speed systems may provide an energy savings between 20% and 40%. The increased ability for variable speed

systems to better meet capacity demands comes at the cost of an increase in the nonlinear dynamic response and also an increase in the coupling between control parameters. In order to maintain performance, advanced control techniques are developed to account for the inherent nonlinear dynamics and strong coupling.

Along with system capacity, evaporator superheat is another key parameter in the vapor compression cycle which influences the efficiency of the system. Evaporator superheat is a measure of the temperature at which the refrigerant is above its saturation temperature at the outlet of the evaporator. An evaporator superheat of 0 indicates that the refrigerant is in a saturated state, consisting of a vaporized and liquid portion. If liquid refrigerant enters the compressor damage may occur, including oil losses and physical damage. The expansion device is used to control the level of superheat by influencing the refrigerant mass flow rate. An adequate amount of superheat ensures that no liquid refrigerant will exit the evaporator and later damage the compressor. However, in the evaporator the heat transfer coefficient between the two-phase refrigerant and the evaporator wall is significantly greater than that in the superheat region. Therefore, in order to maximize the cooling capacity of the evaporator superheat must be minimized.

During operation, the expansion device is controlled to maximize efficiency while protecting the compressor from liquid drawback. With variable capacity systems this becomes more difficult due to the strong coupling inherent to the vapor compression cycle. In practice, a superheat set point is set based on the superheat deviation during anticipated disturbances. A superheat controller that is able to regulate superheat more precisely will ultimately allow for a lower superheat set point which provides increased evaporator cooling capacity. Therefore, superheat control loops are designed through this research to precisely regulate superheat to low levels while maintaining high performance during disturbances. In order to accomplish this, control algorithms are developed to be responsive to system transients while also maintaining robustness to plant uncertainty.

1.3   Testing Methods

Control devices for the vapor compression system have been developed over the past century through rigorous experimental testing to ensure the performance and the reliability of

these devices. The experimental testing phase is extremely important for research and design groups since failure modes and limitations must be identified and addressed before full scale production is entered. During this phase, testing is performed while the AC&R system is subjected to conditions which replicate what the system will experience while operating in the field. Extreme conditions, such as large ambient temperatures with sudden transients, are placed on the system during testing to ensure performance specifications are met during the harshest conditions.

A common method used for testing AC&R systems is through the use of an environmental test chamber, also known as a psychometric chamber. With this method the AC&R unit is attached to its container and placed within a test chamber which replicates the ambient conditions and disturbances that the system may be subjected to by the consumer. Figure 1.3 illustrates the testing of a transport air conditioning system within an environmental test chamber. The test chamber has a conditioning system which heats and cools the environment to subject the city bus to a variety of conditions, such as a very hot 100°F day or a cool, rainy 60°F day.
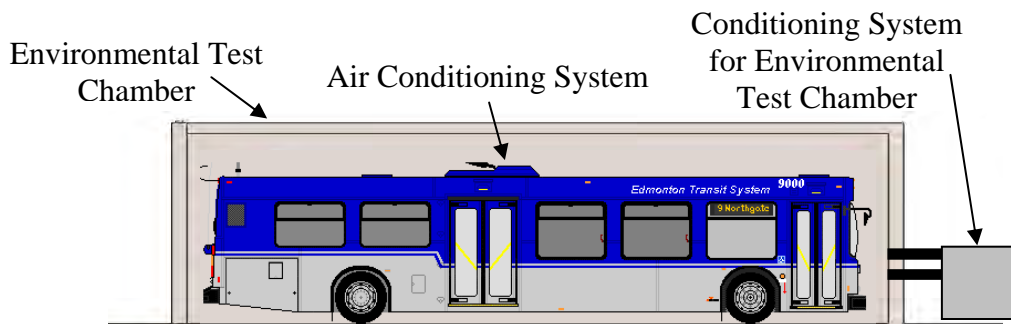
Figure 1.3   Environmental test chamber testing

In this case, the environmental test chamber is the size of a large bus and consumes large amounts of lab space. Independent of size, all environmental test chambers require resources for installation, operation, and maintenance. An alternative testing method has been investigated through this work where the container and ambient conditions are virtually replicated through an on-line simulation environment as shown in Figure 1.4. This method is referred to as hardware-in-the-loop load emulation where a simulation environment takes the place of the environmental test chamber. An emulation unit places the virtual load on the experimental system to replicate

what the system would experience while cooling the container in the actual environment. Automobile engines are tested in a similar method where a dynamometer places torque on the engine which is coupled to a computer to evaluate performance. Hardware-in-the-loop load emulation ultimately allows for a flexible testing environment for AC&R systems with a reduced need for full scale test chambers and containers.
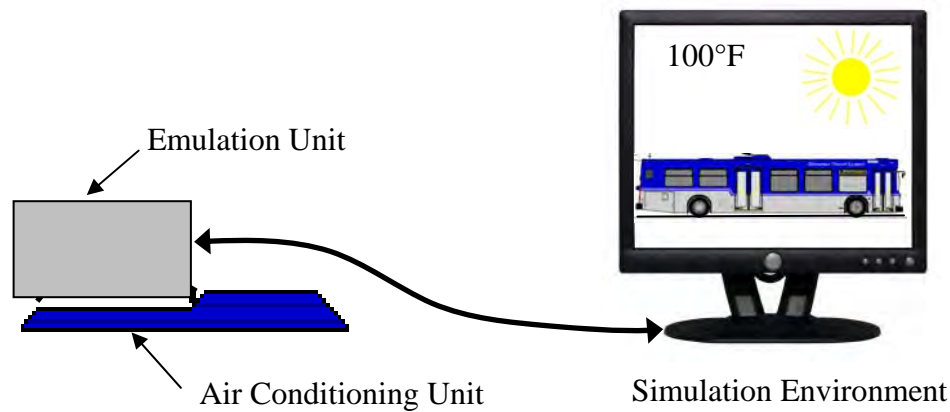
Figure 1.4   Hardware-in-the-loop load emulation

1.4   Organization of Thesis

The remainder of this thesis is organized as follows. Chapter 2 describes the experimental system used during model development and controller validation. Chapter 3 presents the alternate testing method of hardware-in-the-loop load emulation and results from such testing. Modeling and simulation techniques are discussed in Chapter 4. Chapter 5 provides an in-depth discussion of superheat control design and implementation. In this chapter control features are developed to supplement and improve upon the state of the art methods. Chapter 6 presents controller validation through hardware-in-the-loop load emulation. Finally, Chapter 7 summarizes the main contributions of this thesis and presents avenues for potential future research.

Chapter 2

Experimental System

The experimental system used for empirical model development and controller validation is located in the Mechanical Science and Engineering department at the University of Illinois. The experimental system was developed through Air Conditioning and Refrigeration Center support via ACRC project # 123, 163, 170, and 175. This chapter presents an overview of the experimental system including actuators, sensors, and data acquisition systems. The reader is referred to [7] for a more detailed description of the system.

2.1   General System Configuration

Figure 2.1   Experimental test stand

The experimental system at the University of Illinois is a dual evaporator test stand that is able to mimic the behavior of a variety of AC&R system configurations as shown in Figure 2.1. This system has a semi-hermetic reciprocating compressor, a single condenser, an array of expansion devices, two evaporators, and an internal suction line heat exchanger. The system contains bypasses and valves to allow the system to be configured in many different modes: single or dual evaporator, thermostatic expansion valve, electronic expansion valve, or automatic expansion valve. The internal heat exchanger may also be included or isolated with a certain valve configuration. Figure 2.2 shows a schematic of the experimental test stand which shows the configuration of the components and the locations of the sensors and actuators.
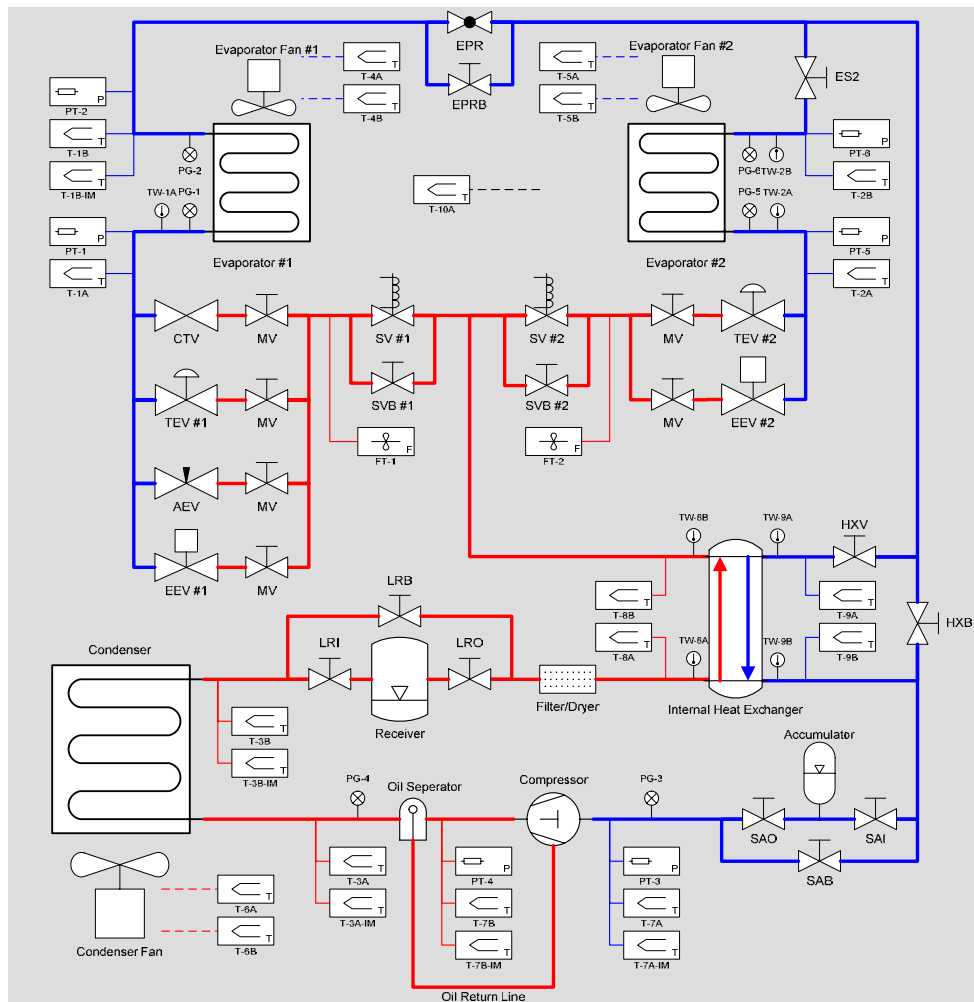
Figure 2.2   Schematic of experimental test stand

9

Table 2.1   Valve descriptions

Valve Designation	Description
CTV	Capillary Tube Valve
TEV	Thermostatic Expansion Valve
AEV	Automatic Expansion Valve
EEV	Electric Expansion Valve
SV	Solenoid Valve
SVB	Solenoid Valve Bypass
EPR	Evaporator Pressure Regulating Valve
EPRB	Electronic Pressure Regulating Valve Bypass
ES2	Evaporator Side #2 Valve
HXV	Internal Heat Exchanger Valve
HXB	Internal Heat Exchanger Bypass
LRI	Liquid Line Receiver Inlet
LRO	Liquid Line Receiver Outlet
LRB	Liquid Line Receiver Bypass
SAI	Suction Line Accumulator Inlet
SAO	Suction Line Accumulator Outlet
SAB	Suction Line Accumulator Bypass
MV	Manual Valve

Table 2.2   Component information

Component	Manufacturer	Model	URL
Evaporator Fan and Casing	Larkin (HeatCraft)	VAK-17A	www.heatcraftrpd.com
Evaporator #1	HeatCraft	52601301 (VAK-17A)	www.heatcraftrpd.com
Evaporator #2	Blissfield	BH517	www.blissfield.com
Condenser and Fan	Tecumseh (Blissfield)	50803-1 (66001-3)	www.blissfield.com
Internal Heat Exchanger	Superior (Sherwood)	HXSV-1/2	www.sherwoodvalve.com
Liquid Line Receiver	AC&R Components, Inc. (Henry Tech.)	S-8064	www.henrytech.com
Suction Line Accumulator	AC&R Components, Inc. (Henry Tech.)	S-7043	www.henrytech.com
Oil Separator	AC&R Components, Inc. (Henry Tech.)	S-5581	www.henrytech.com
Compressor	Copeland	KANA-006E-TAC-800	www.copeland-corp.com
Variable Frequency Drive	Baldor	ID15J101-ER	www.baldor.com
Capillary Tubing	Sealed Unit Parts Co., Inc.	BC-4	www.supco.com
TEV	Sporlan Valve Co.	FJ ¼ C	www.sporlan.com
AEV	Parker-Hannefin	A2	www.parker.com
EEV	Sporlan Valve Co.	SEI-0.5	www.sporlan.com
EPR	Sporlan Valve Co.	ORIT 6-0/50-1/2"	www.sporlan.com
Manual Valves	Mueller Brass Co.	14838, 14841	www.muellerindustries.com
Filter-Dryer	Sporlan Valve Co.	C-052	www.sporlan.com
Sight Glasses	Sporlan Valve Co.	SA-14S, SA-12FM	www.sporlan.com
Pressure Transducers	Cole-Palmer	07356-53, 07356-54	www.coleparmer.com
Pressure Gauges	Ritchie Engineering Co., Inc.	49051, 49052	www.yellowjacket.com
Mass Flow Transducers	McMillan Company	102-6P	www.mcmflow.com
Immersion Thermocouple	Omega	GTMQSS-062U-6	www.omega.com
Welded Thermocouple	Omega	FF-T-20-100	www.omega.com
Watt Meter	Ohio Semitronics, Inc.	GW5-019D	www.ohiosemitronics.com
Pressure Switches	Ranco	010-1402, 011-1711	www.ranco.invensys.com
Line Reactors	MTE (Galco Industrial Electronics)	MTE RL-00402	www.galco.com
Analog Input Board	Measurement Computing, Inc.	PCI-DAS1200/JR	www.measurementcomputing.com
Analog Output Board	Measurement Computing, Inc.	PCI-DDA-08/12	www.measurementcomputing.com
Thermocouple Board	Measurement Computing, Inc.	PCI-DAS-TC	www.measurementcomputing.com
Signal Conditioners	Omega	OM5 Series	www.omega.com
DC Motor for Blade Actuation	Pittman	Lo-cog 12VDC 218.4:1	www.ametektip.com

2.2 Sensors

The experimental test stand has an array of sensors that allow the system to be completely monitored during testing. Collectively, the sensors provide data which may be used to determine the performance of various components while also providing information on the overall system efficiency. The system is fully instrumented with six pressure gauges, two mass flow meters, and 24 thermocouples. The pressure sensors are strain-gage based measurement devices that are located at the input and output of the condenser and each evaporator. Type T welded tip thermocouples are used for air temperature measurements, whereas thermocouples with stainless steel sheaths are used for immersed refrigerant temperature measurements. Table 2.3 describes the type and location of the individual sensors.

Table 2.3   Sensor designation

Surface Thermocouple	Immersion Thermocouple	Thermowell	Location
T-1A		TW-1A	Evaporator #1 Inlet
T-1B	T-1B-IM	TW-1A (removed)	Evaporator #1 Outlet
T-2A		TW-2A	Evaporator #2 Inlet
T-2B	T-2B-IM	TW-2B (removed)	Evaporator #2 Outlet
T-3A	T-3A-IM	TW-3A (removed)	Condenser Inlet
T-3B	T-3B-IM	TW-3B (removed)	Condenser Outlet
T-4A			Evaporator #1 Air Inlet
T-4B			Evaporator #1 Air Outlet
T-5A			Evaporator #2 Air Inlet
T-5B			Evaporator #2 Air Outlet
T-6A			Condenser Air Inlet
T-6B			Condenser Air Outlet
T-7A	T-7A-IM	TW-7A (removed)	Compressor Inlet
T-7B	T-7B-IM	TW-7B (removed)	Compressor Outlet
T-8A		TW-8A	Internal Heat Exchanger – Liquid Inlet
T-8B		TW-8B	Internal Heat Exchanger – Liquid Outlet
T-9A		TW-9A	Internal Heat Exchanger – Vapor Inlet
T-9B		TW-9B	Internal Heat Exchanger – Vapor Outlet
T-10A			Ambient
Pressure Transducer	**Pressure Gage**	**Flow Transducer**	**Location**
PT-1	PG-1		Evaporator #1 Inlet
PT-2	PG-2		Evaporator #1 Outlet
PT-3	PG-3		Compressor Inlet
PT-4	PG-4		Compressor Outlet
PT-5	PG-5		Evaporator #2 Inlet
PT-6	PG-6		Evaporator #2 Outlet
		FT-1	Expansion Device #1 Inlet
		FT-2	Expansion Device #2 Inlet
Potentiometer			**Location**
5 K-ohm			Emulation blade – non-drive side

2.3 Actuators

The experimental test stand is outfitted with various actuators which allow for the control of important system parameters. The test stand has four main control inputs: compressor speed, expansion valve opening, evaporator fan speed and condenser fan speed. Presently, most AC&R systems in production have fixed compressor and fan speeds. Therefore, the experimental test stand does not necessarily replicate the configuration of a commercially available AC&R system. Instead, the experimental test stand at the University of Illinois is outfitted with these actuators to allow for advanced control research which may demonstrate the usefulness of such actuators.

2.3.1 Compressor

The experimental test stand has a semi-hermetic reciprocating compressor shown in Figure 1.4. The compressor has a variable frequency drive that controls the speed of the electric motor which is coupled to the compressor through a drive shaft. This component compresses low-temperature, low-pressure refrigerant vapor to a high-temperature, high-pressure state. The compressor speed can be controlled via the control software to speeds between 0 and 2200 RPM. A power meter monitors the average power consumption of the compressor during operation which may be used while investigating system efficiency.

Figure 2.3   System compressor

2.3.2 Electronic Expansion Device

The electronic expansion device on the experimental system controls the refrigerant mass flow rate of the system through the positioning of a needle valve, referred to as a pin in Figure 2.4. The position of the needle is precisely controlled by the actuation of a geared stepper motor coupled to the needle. The stepper motor is controlled by a motor control board which takes in

an absolute valve position signal from the digital to analog control board. This signal is then converted into an appropriate step command signal which is sent to the EEV to actuate the stepper motor. The degree to which the EEV may be used to regulate superheat depends strongly on the software control design as discussed in Chapter 5.
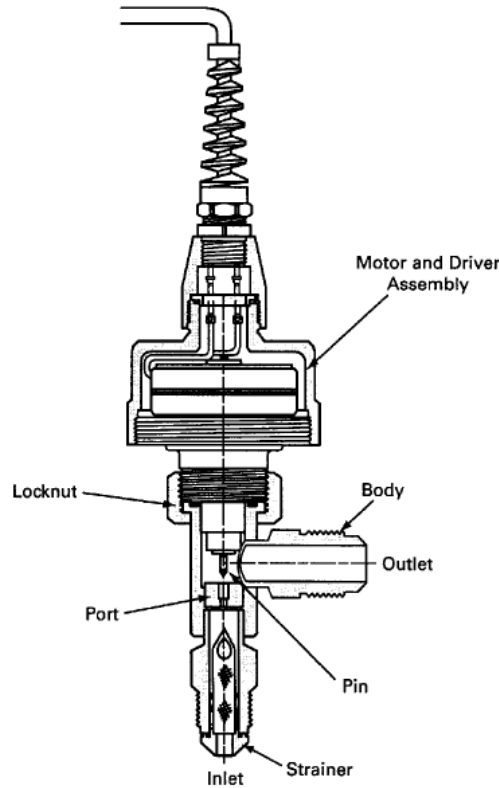
Figure 2.4   Electronic Expansion Valve

The electronic expansion device on the experimental test stand was installed in the early 2000s and has since been heavily utilized. The valve now exhibits a substantial amount of hysteresis after being in use for nearly a decade as shown in Figure 2.6. Without compensation the current amount of valve hysteresis causes oscillatory control; therefore compensation must be performed to improve performance. The hysteresis is identified through open loop testing to be about 1% of the overall opening range. This amount of hysteresis would normally be acceptable for valves that are properly sized for the system in which they are installed on. However, the EEV on the experimental test stand is greatly oversized (this valve may be used to regulate a system with 5 times the capacity) even though it was the smallest valve available at the time. On the experimental system the valve is normally operated between 10% and 20% opening,

13

therefore in this case a 1% hysteresis is more substantial since it is equivalent to hysteresis that is 5% to 10% of full stroke. With the hysteresis identified, a compensation block may easily be implemented to reduce the effects of this hysteresis as shown in Figure 2.5. This hysteresis compensator is used for the results shown in this thesis.
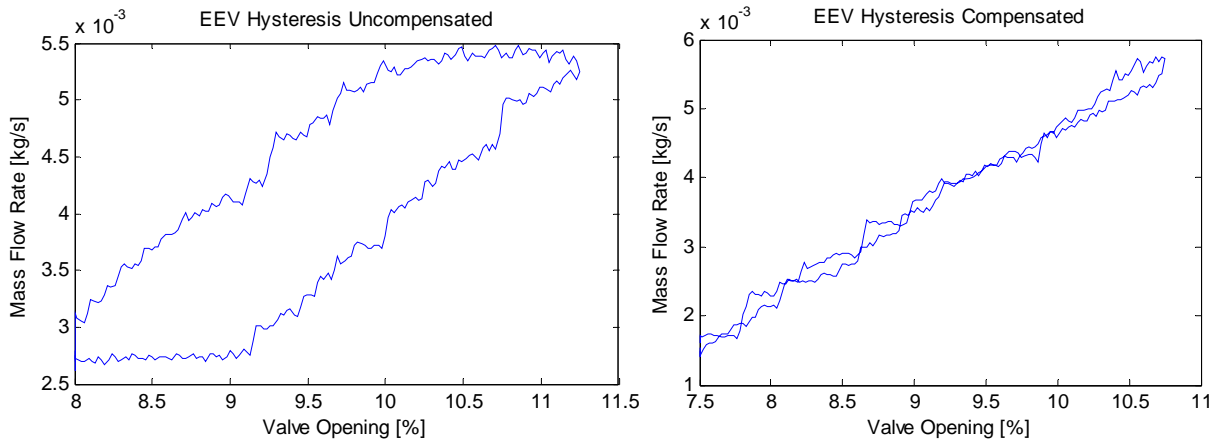
Figure 2.5   Valve hysteresis compensation

Figure 2.6   Photo of the EEV

2.4   Components

The experimental system is equipped with two liquid to air evaporators, a condenser, and an internal heat exchanger. The system also has an oil separator, filter/dryer, accumulator,

receiver, sight glasses, and manual valves. Many of these components may be isolated or included in the system with certain manual valve configurations.

The oil separator is in the refrigerant line between the compressor and the condenser. The function of this device is to return oil to the compressor by separating oil from the refrigerant. The filter/dryer reduces the amount of moisture, acids and other particulates from the refrigerant which may potentially cause reduced component efficiency and flow obstruction. The sight glasses mounted throughout the system allow the operator to visually determine the state of the refrigerant (i.e. vaporized or liquid state).

The suction line accumulator is designed to ensure the refrigerant entering the compressor is completely vaporized. The accumulator is in the refrigerant line between the evaporator and the compressor and is designed to trap any liquid which enters to ensure only vapor is allowed to reach the compressor. Another component that some AC&R systems are equipped with is a liquid-line receiver. This component is installed in the refrigerant line between the condenser and the expansion device to ensure the refrigerant is completely condensed before entering the expansion device. This device improves the refrigerant flow since vaporized refrigerant flowing across the expansion valve may cause flow rate variations. The receiver and accumulator are isolated from the system for the results shown in this thesis.

2.4.1 Heat Exchangers

The heat exchangers on the experimental system are tube-and-fin type liquid to air heat exchangers. The fins of the condenser unit are made of steel where the two evaporators are constructed of copper tubes and aluminum fins. The two evaporators are constructed of the same material, but have different tubing configurations which influence the heat transfer. Evaporator number 1 is a 'two-slab' tube configuration where the refrigerant enters the top of the evaporator, goes back and forth down the front side, and flows back and forth up the back side before exiting. This configuration may be considered a series of two heat exchangers sitting on top of one another. Evaporator number 2 is a 'single-slab' configuration where the refrigerant enters the top of the evaporator, goes back and forth and exits the bottom of the evaporator. Evaporator number 2 is used for model development and controller validation in this thesis. Likewise, evaporator number 1 could have been chosen for model development and controller validation,

however, a majority of the Thermosys models have been validated using evaporator number 2 [8].

The fan speeds of each evaporator and condenser are controllable. This is achieved through independent control boards which modulate the speed of the AC fan. Figure 2.7 and Figure 2.8 show photos of the condenser and evaporator fans.

Figure 2.7   The condenser fan unit

Figure 2.8   The evaporator unit fan

A suction line internal heat exchanger may be configured to transfer heat from the refrigerant entering the expansion device to the refrigerant entering the compressor. The suction line internal heat exchanger increases the system capacity through pre-heating the vaporized refrigerant entering the compressor and also sub-cooling the liquid refrigerant entering the expansion device. This component is isolated from the system during model development and controller validation.

2.5 Data Acquisition and Control

The data acquisition system collects and stores sensor data for analysis on a desktop PC. A thermocouple board and analog input board are used to convert analog sensor data measurements to digital signals for reading and storage. The 16-channel thermocouple board is used to read 16 temperature measurements at a sampling rate of 10 Hz. The software used to interface the desktop PC with the data acquisition system is MATLAB Real Time Workshop and WinCon. A digital to analog board is coupled with WinCon to output voltage levels for the control of system actuators. During model development and controller validation the data acquisition system is set to operate at a rate of 10 Hz. This sampling rate is adequate for control and monitoring due to the slower temperature dynamics of the vapor compression cycle.

Chapter 3

# Hardware-in-the-Loop Load Emulation

This chapter presents a novel approach for experimentally simulating various environmental conditions and container parameters on air conditioning and refrigeration systems. Typically, AC&R systems are placed within an environmental test chamber where testing is done to determine the performance of the system. The environmental test chamber is conditioned, with heaters and air conditioners, to represent environments that AC&R systems may be subjected to by the consumer. This type of testing allows for the experimental evaluation of component and control loop performance during various disturbances and ambient conditions while the system is cooling a given container. The environmental test chambers consume large amounts of lab space while also requiring resources for installation, operation, and maintenance.

To mitigate these issues, hardware-in-the-loop load emulation has been developed to test AC&R systems with a reduced need for environmental test chambers. Alternatively, an on-line real time environmental simulation accounts for the interactions between the environment and container while sensor measurements are used to determine the virtual cooling performance. The on-line simulation outputs a virtual load which is placed on the experimental system through an emulation unit attached to the experimental AC&R system; this is analogous to a dynamometer attached to an engine for automotive testing. The virtual load is representative of what the system would experience while cooling the specified container in the actual environment. Hardware-in-the-loop load emulation ultimately provides a flexible testing environment with a reduced need for environmental test chambers. This chapter details the hardware-in-the-loop load emulation testing method and presents results from an experimental test stand virtually cooling a truck environment.

3.1 Introduction

Almost all AC&R systems cool some type of container or space such as a building, truck environment, or a household refrigerator. Therefore, it is important to determine the performance of AC&R systems while cooling a container in certain ambient conditions (i.e. transport refrigeration performance during changing ambient conditions). Part of this performance evaluation would include the assessment of control loop performance such as the superheat or capacity control loops. Control loop evaluation is particularly important since the dynamics of the vapor compression cycle are influenced by the inlet air temperature which is equivalent to container temperature. Current modeling and simulation techniques may be used to predict the cooling and control loop performance of AC&R systems while cooling a given container in certain ambient conditions [9]. These modeling techniques accurately predict the performance of AC&R systems. However, experimental validation is almost always required to determine the actual performance of the system.

One method that is used to test AC&R systems is to place the system in the actual end-use environment for testing as illustrated in Figure 3.1. For example, testing the air-conditioning system on a city bus may be done by driving the bus around a city while monitoring control loops and collecting data. This method is not frequently used since the ambient conditions and disturbances on the system are not controllable but rather dictated by local weather. With this method it is also difficult to test the system to extreme conditions since there is little to no control over the environment.
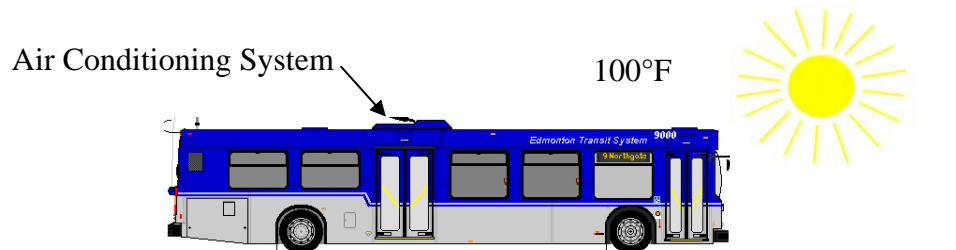
Figure 3.1 AC&R system placed in the actual environment for testing

A more common method used to validate system performance is through testing AC&R systems in environmental test chambers, also known as psychometric test chambers. In this testing scenario the AC&R unit is attached to the container and placed within the test chamber

which is conditioned to replicate ambient conditions. Environmental test chambers may be large enough to hold household refrigerators or may be much larger for applications such as in transport refrigeration. Figure 3.2 illustrates the testing of a truck environment in an environmental test chamber. With this testing configuration, control loops of the AC&R system may be evaluated during ambient temperature fluctuations and other system disturbances. Environmental test chambers require resources for installation, operation, and maintenance. Test chambers also consume large amounts of lab space which is usually limited.
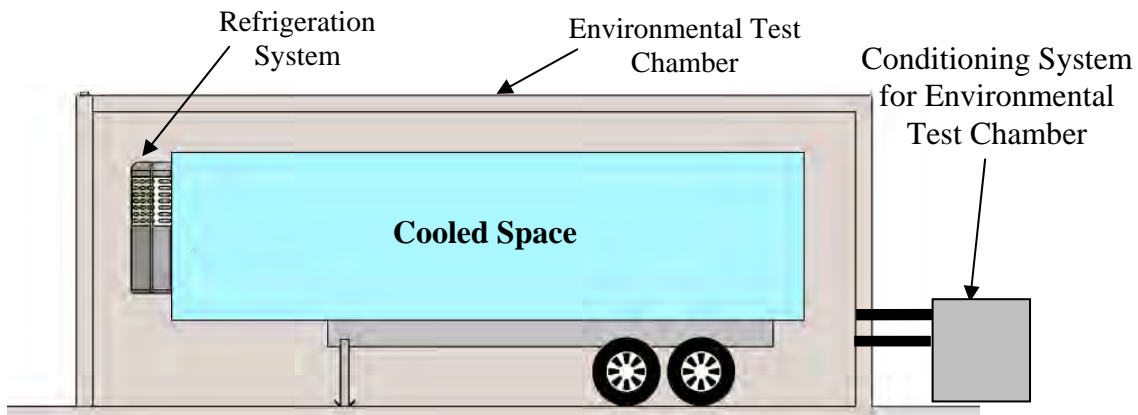
Figure 3.2   Conventional testing method using environmental test chamber

To mitigate these issues, hardware-in-the-loop load emulation has been investigated to perform a task similar to the environmental test chamber. Hardware-in-the-loop (HIL) simulation is a common technique that has been used for many applications to reduce testing cost while providing a more flexible and controlled testing environment [10], [11]. A HIL testing configuration is typically used as an intermediate or alternative step for testing a system in its actual environment.

Hardware-in-the-loop load emulation uses a model to account for the interactions between the environment, the container, and the system instead of relying on a test chamber to replicate these interactions. Figure 3.3 illustrates the testing of a transport refrigeration unit through load emulation. An emulation unit places an equivalent load on the experimental AC&R system which is intended to replicate the load the experimental system would experience if subjected to such ambient conditions while cooling the specified container.
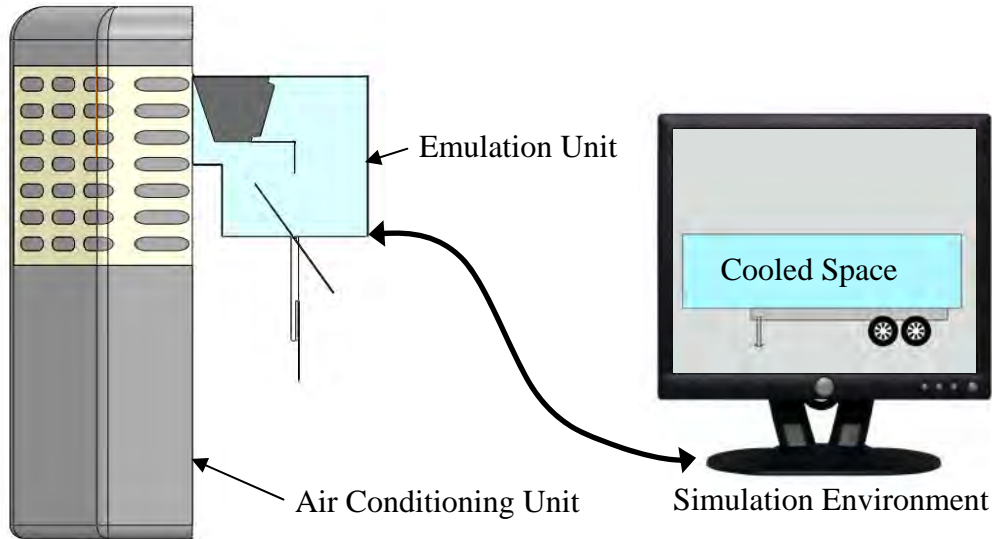
Figure 3.3   Hardware-in-the-loop load emulation

A refrigeration transport application is used in this chapter to illustrate load emulation. Nevertheless, this technique may be applied to a variety of AC&R applications. The remainder of this chapter is organized as follows. Section 3.2 outlines the load emulation framework. The concept and the construction of the emulation unit are discussed in Section 3.3. Section 3.4 provides a summary of the environmental load model. Section 3.5 describes the load emulation control configuration. This section identifies the dynamics of the emulation unit and details the inner workings of the emulation control loop. In Section 3.6 load emulation results are presented for a refrigeration system virtually cooling a truck environment. Finally, Section 3.7 summarizes the contributions of hardware-in-the-loop load emulation.

3.2   Load Emulation Framework

Vapor compression cycle hardware-in-the-loop load emulation is a novel technique that may experimentally simulate different environmental conditions and container sizes on a given system without the need to experimentally replicate such conditions in a test chamber. An environmental load model is used to characterize the container parameters, the environmental conditions, and system disturbances such as door openings. This model is implemented on-line during load emulation testing which allows for flexible testing of arbitrary environments and container parameters.
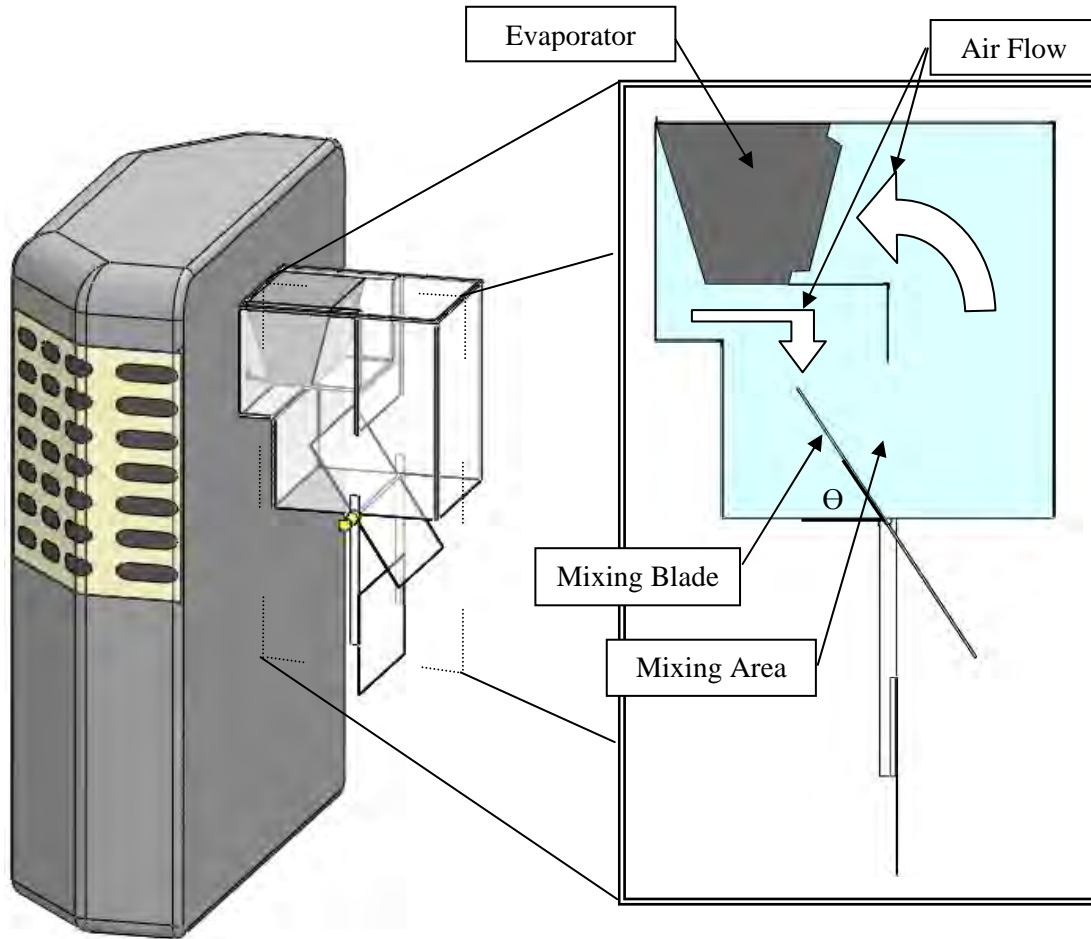
Hardware-in-the-loop load emulation is composed of two main components: an emulation unit and an environmental load model. The emulation unit is designed to allow for on-line control of the load on the AC&R unit. The load on the AC&R system is equivalent to the inlet air temperature and mass flow rate across the evaporator since these two parameters influence the heat transfer across the evaporator. The mass flow rate of the air is influenced by humidity which is not controlled in the results shown in this chapter. The consideration of humidity is one potential area for future research and is discussed in Chapter 7. The results shown in this thesis assume a constant mass air flow rate, therefore, making the load on the AC&R system solely equivalent to the evaporator inlet air temperature.

During system startup, container temperature may be very large; the large temperature places a large load on the vapor compression system due to the significant temperature difference between the refrigerant and the air. As the container temperature decreases, the AC&R system has a smaller load due to the decreased evaporator inlet air temperature. Inlet air temperature is exclusively used to describe the loading on the system for the load emulation shown here since the air mass flow rate is considered constant due to a constant evaporator fan speed and relatively constant humidity (controlled by the central air-conditioning unit of the Mechanical Engineering Laboratory at the University of Illinois). The current configuration may be extended to consider applications with variable speed fans by accounting for the correlation between mass air flow and fan speed in the on-line real-time environmental load model.

3.3   Emulation Unit

The emulation unit is attached to the evaporator and/or condenser during testing to control the inlet air temperature. In this research load emulation is considered on the evaporator side only, although a similar approach may be taken to emulate conditions on the condenser side. The main function of the emulation unit is to control the evaporator inlet air temperature through the mixing of evaporator outlet air (cold air) with ambient air (warm air) with a mixing blade. Figure 3.4 shows a computer aided design (CAD) model of the emulation unit which is attached to a transport refrigeration unit. In this illustration, the large arrows within the emulation unit represent the airflow throughout the emulation unit. The air enters the emulation unit on the right and is passed through the evaporator where the air is cooled. The air flows down the left

side of the emulation unit where a portion of the outlet air is redirected toward the inlet by the mixing blade while the other portion of air exits the emulation unit. The angle, Ө, of the mixing blade is modulated via a DC motor to control the evaporator inlet air temperature, or system load, by controlling the amount of mixing.

Figure 3.4   Hardware-in-the-Loop load emulation

To further explain the operation of the emulation unit, some possible blade angles and their air flow paths will be discussed. Figure 3.5 shows the emulation unit at three different states; a blade angle of 90°, 45°, and 0°. When the blade angle is positioned at 90° the evaporator fan pulls 100% ambient air into the emulation unit. The air is cooled through the evaporator and is completely discarded to the surrounding environment. No mixing occurs since a blade angle of 90° isolates the inlet and outlet chambers of the emulation unit. A blade angle of 90° provides the evaporator with the largest attainable inlet air temperature which is equal to

23

that of the ambient air. If an evaporator inlet air temperature larger than the ambient air temperature is desired a heater may be used to direct air into the emulation unit to increase the evaporator inlet air temperature. This method may be used to attain desired inlet air temperature for certain testing scenarios. However, this technique is not used for load emulation results shown in this thesis. The vertical dividing wall beneath the blade is designed to prevent unintended mixing of outlet air with inlet air while the blade is fully open at an angle of 90°. When the blade is at mid stroke, 45° pictured in Figure 3.5, the evaporator fan pulls in a mixture of ambient air (warm) and evaporator outlet air (cool). The outlet air exits the evaporator where a portion of the flow is redirected back towards the inlet by the mixing blade. Mixing a higher percentage of outlet air with ambient air decreases the inlet air temperature. When the blade is at an angle of 0° the evaporator fan pulls in air directly from the outlet of the evaporator. This can be thought of as a closed loop where the air within the emulation unit is continually cooled while being passed through the evaporator. When the blade angle is maintained at 0° the temperature will approach a lower bound which depends on the cooling capacity of the system and the heat transfer characteristics of the emulation unit.
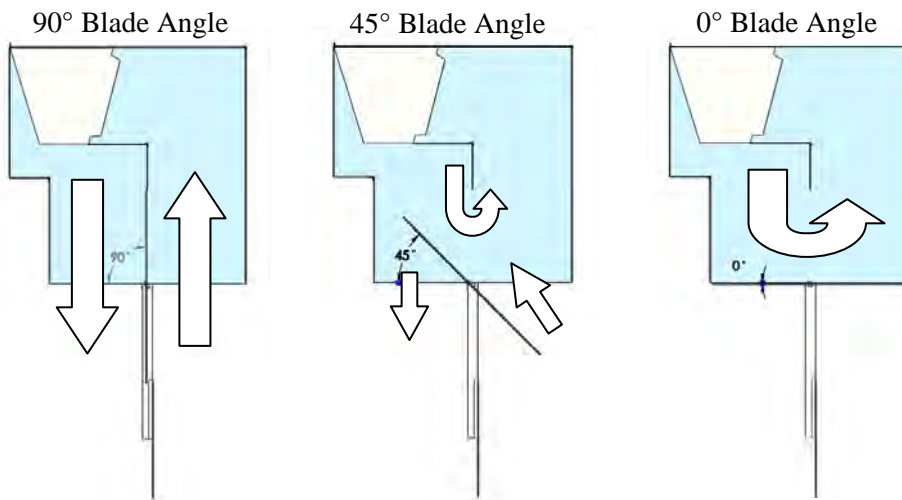
Figure 3.5   Interaction between blade angle and inlet air temperature

Using the principle of mixing, the emulation unit has been designed to electronically control the inlet air temperature of the evaporator. The emulation unit was also designed to be easily installed and removed from the experimental AC&R system to allow the system to be configured easily by different researchers. Figure 3.6 shows a computer aided design model of

the emulation unit. This unit is relatively compact, measuring approximately 2ft x 1.5ft x 4ft, making this unit ideal for a laboratory environment. The inverted 'L' shaped design of the emulation unit was pursued to provide needed clearance for piping on the experimental test stand. The volume of the main chamber of the emulation unit is approximately 6 cubic feet. The volume of the emulation unit places a lower limit on the container size that may be virtually simulated on the experimental system. For example, this emulation unit may not be used to virtually simulate a container which is smaller than 6 cubic feet. More importantly, this emulation unit is able to virtually simulate a container which is larger than 6 cubic feet.
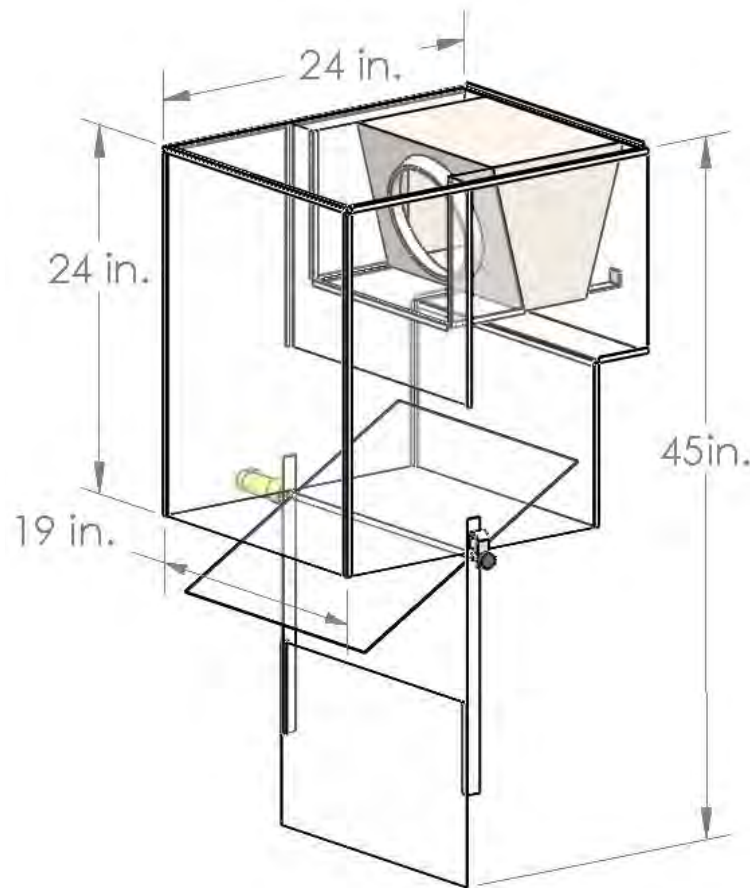
Figure 3.6   CAD model of emulation unit

The emulation unit is mainly constructed out of polycarbonate sheets and aluminum framing. The polycarbonate sheets were chosen for construction to provide a transparent design to allow the user to observe the blade and evaporator fan during testing. For certain low temperature emulation tests, the heat transfer through the polycarbonate sheets is too large.

Specifically, during the off cycle of an on-off AC&R system emulation test the temperature within the emulation unit may rise at a rate faster than the virtual rate; this scenario may be present if the virtual container has more insulation than the emulation unit. In this case, insulation may be added to the outside of the emulation unit to decrease the heat transfer rate; this method was used for the results in Figure 3.30 shown later in this chapter. Figure 3.7 shows a photo of the emulation unit while attached to the experimental AC&R test stand.

Figure 3.7   Photo of emulation unit

The blade of the emulation unit is mounted to a shaft which is directly fixed to a DC motor. The DC motor is driven by a motor control board; see Figure 3.8 and Figure 3.9. The motor control board takes an input signal between 0 and 5 volts from the data acquisition control board on the computer. The output of the motor control board is a pulse width modulated (PWM) signal which controls the speed and direction of the motor shaft.

Table 3.1 shows the relationship between the input voltage and the output PWM and direction of the motor controller.

Table 3.1   Motor controller input/output relation

Input Voltage [V]	Output PWM	Direction
0.0	100%	CCW
1.25	50%	CCW
2.5	0%	n/a
3.75	50%	CW
5.0	100%	CW

A geared DC motor is used to provide the torque necessary to rotate the emulation blade. The speed of the geared DC motor is adequate for this application since the slow temperature dynamics do not require fast blade rotation speeds. The emulation unit also has a micro switch, visible in Figure 3.9, which cuts power to the motor to prevent damage when the blade rotates past the closed position. Specifically, this micro switch is installed to prevent damage when the user stops data collection. When data collection is stopped all outputs are grounded, causing the input voltage to the motor control board to reach 0 volts. The motor control board takes an input of 0 volts and outputs a 100% PWM signal to the motor as presented in Table 3.1. This causes the motor to rotate the blade at full speed towards the closed position. Without the micro switch, the blade rotates past the closed position and hits the side of the emulation unit opening which stops the blade and causes damage to the mounting hardware between the motor shaft and the blade. Therefore, the micro switch is configured to cut power to the motor before damage occurs.
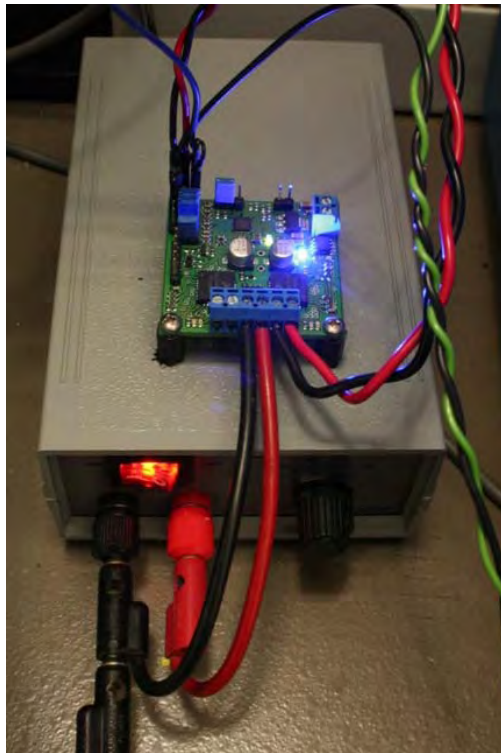
Figure 3.8   Blade angle motor controller and power supply

DC Motor
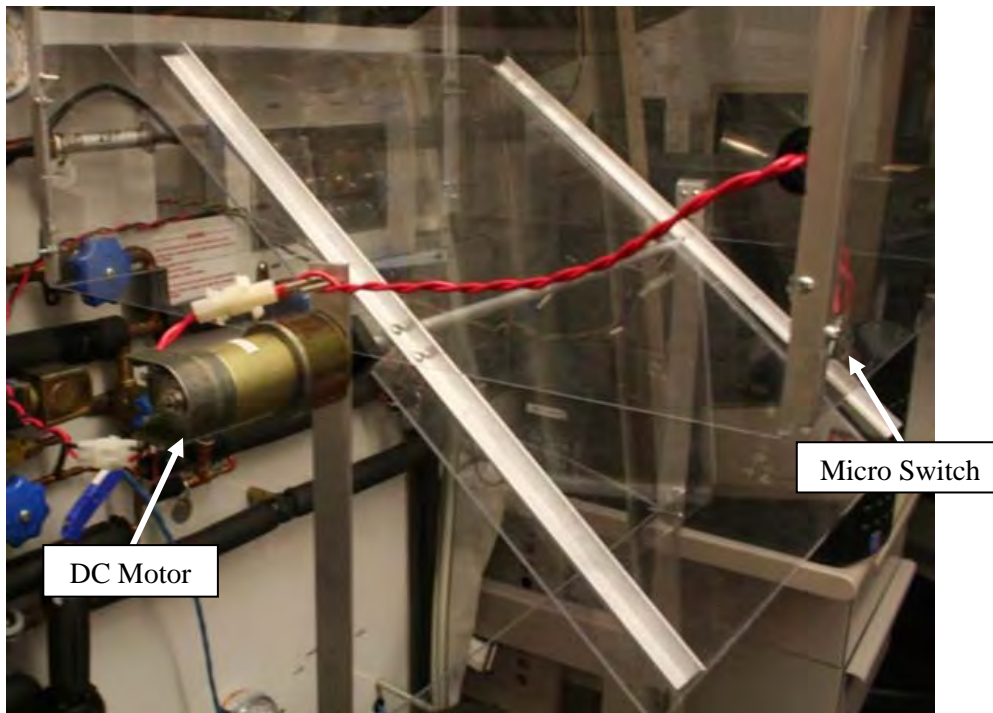
Micro Switch

**Figure 3.9   Blade angle motor and micro switch**

Opposite of the DC motor is a potentiometer which provides angular feedback to the control loop; see Figure 3.10. The output of the potentiometer is a voltage signal between 0 and 5 volts which is proportional to the angle of the blade. The output of the potentiometer is filtered in software to reduce noise before being used for control purposes.
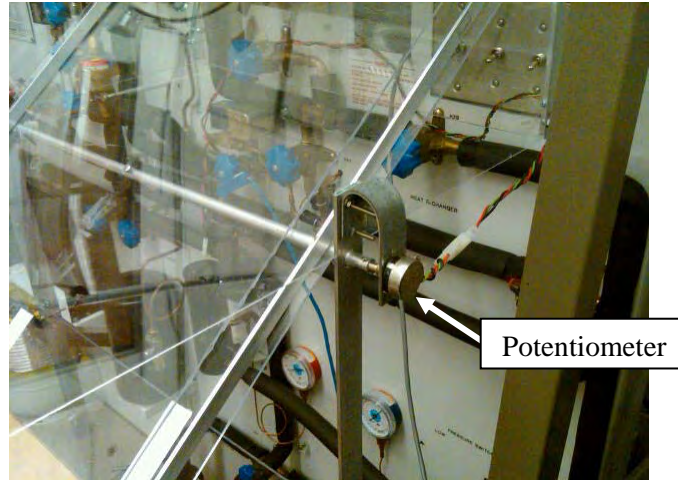
Potentiometer

Figure 3.10   Blade angle potentiometer

3.4   Environmental Load Model Development

The second key component for load emulation is the environmental load model. The environmental load model accounts for the container parameters, environmental conditions, and system disturbances. The interaction between the container and the VCC system is illustrated in Figure 3.11. The cooled space is coupled to the VCC system such that the cooled space input is the supply air temperature from the VCC unit. Simultaneously, the VCC system input is the return air, which is the output of the cooled space.
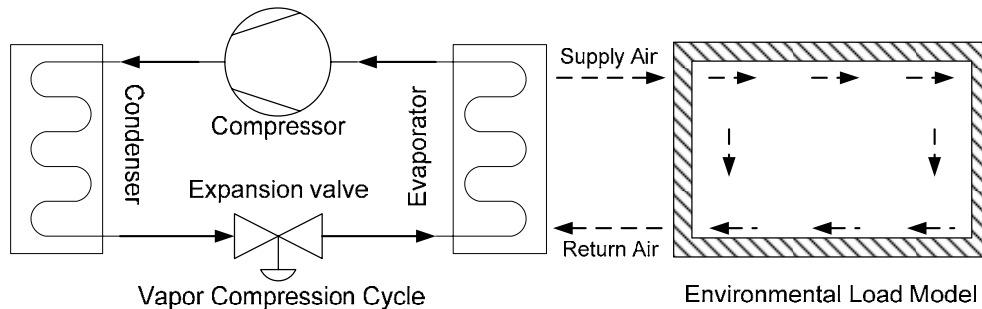
Figure 3.11   Schematic of the coupling between the VCC and the cooled space

3.4.1 Environmental Load Model Description

The environmental load model has been developed using the approach presented in Li et al. [9]. This model accounts for the following important effects in refrigeration transport applications: (i) varying ambient conditions, including ambient temperature, solar radiation intensity, and wind speed; (ii) air infiltration; and (iii) door openings for product removal/loading. The environmental load model is developed based on a heat balance approach [12]. More precisely, the load model is formulated by calculating the conductive and convective heat balances for the space surfaces and space air. The major modeling assumptions are given below.

-Uniform air temperature with well-mixed air in the space;

-Uniform surface temperature for the space including its interior and exterior wall surface;

-One dimensional heat conduction through the walls of the space.

This model has been developed with three dynamic states. The cooled space temperature T_{space}, interior surface temperature T_{is} and exterior surface temperature T_{es}, are defined to describe the load model dynamics, as shown in Equation 3.1. The dynamic state derivative equations are given in Equations 3.2-3.4

$$x = \begin{bmatrix} T_{space} & T_{is} & T_{es} \end{bmatrix}^T \tag{3.1}$$

$$\frac{dT_{space}}{dt} = \frac{\dot{Q}_{inconv} + \dot{Q}_{inf} + \dot{Q}_{door} - \dot{Q}_{vcc}}{(MC)_{air}} \tag{3.2}$$

$$\frac{dT_{is}}{dt} = \frac{\dot{Q}_{cond} - \dot{Q}_{inconv}}{(MC)_{wall}} \tag{3.3}$$

$$\frac{dT_{es}}{dt} = \frac{\dot{Q}_{solar} + \dot{Q}_{outconv} - \dot{Q}_{cond}}{(MC)_{wall}} \tag{3.4}$$

The solar load $\dot{Q}_{solar}$, the air infiltration load $\dot{Q}_{inf}$, and the VCC system capacity $\dot{Q}_{vcc}$ are computed from Equations 3.5-3.7. Where I_{sr} is the solar radiation constant, ρ_{air} is the density of the air, D is the door opening area, H is the door height, g is the gravitational constant, and F is the density factor. The sensible and latent refrigeration load, $\dot{Q}_{door}$, from door openings is

calculated by Equation 3.8 [12]. The convection and conduction load information, including $\dot{Q}_{outconv}$, $\dot{Q}_{inconv}$ and $\dot{Q}_{cond}$, can be found in [9]. The major environmental load model parameters used for this study are listed in Table 3.1.

$$\dot{Q}_{solar} = \alpha I_{sr} \tag{3.5}$$

$$\dot{Q}_{inf} = V_{space}\rho_{air}c_{air}(T_{amb} - T_{space})(ACH) \tag{3.6}$$

$$\dot{Q}_{vcc} = \dot{m}_{air}c_{air}(T_{space} - T_{supply}) \tag{3.7}$$

$$\dot{Q}_{door} = 0.221D(h_{amb} - h_{air})\rho_{air}(1 - \frac{\rho_{amb}}{\rho_{air}})^{0.5}(gH)^{0.5}F \tag{3.8}$$

Table 3.2 Environmental load model parameters

| Variable	Definition	Value	Unit
$(MC)_{wall}$	Wall thermal capacity	100	kJ-C^{-1}
$(MC)_{air}$	Air thermal capacity	20	kJ-C^{-1}
$(UA)_{wall}$	Lumped heat transfer coefficient	0.06	kW-C^{-1}
A_{space}	Space surface area	82.43	m^2
V_{space}	Space volume	38.62	m^3
α	Absorptivity to solar radiation intensity	0.12	
ACH	Air changes per hour	0	

3.4.2 Environmental Load Model Validation

The environmental load model is implemented in Thermosys (Rasmussen, 2005), and the model validation scenario involves a temperature pull-down and control test along with door-opening events for the enclosed space. The model is validated against data collected from the cooling of an actual commercial truck environment at Thermo King Corporation. The test procedure can be described as:

-Pull-down the enclosed container air temperature from ambient temperature to a given set point using the refrigeration system;

-Run the compressor in an on-off cycling pattern to maintain the space temperature during which the system disturbance of door openings is introduced.

The environmental load model inputs are given in Figure 3.12 and include ambient air temperature, supply air flow rate, supply air temperature, and door-opening signals. The model validation is presented in Figure 3.13 where the space air temperature from test data is compared to the environmental load model output. This figure shows that the environmental load model matches the experimental data very well. Therefore, this model accurately accounts for the interactions between the AC&R system, container, and environmental conditions.
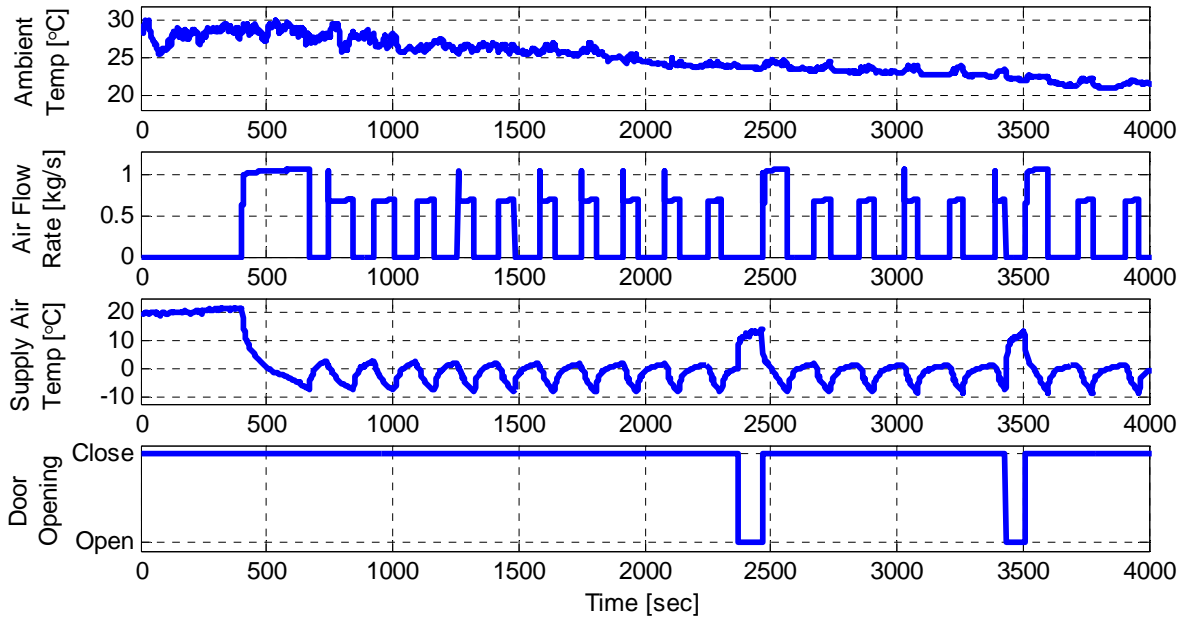
Figure 3.12   Environmental load model inputs
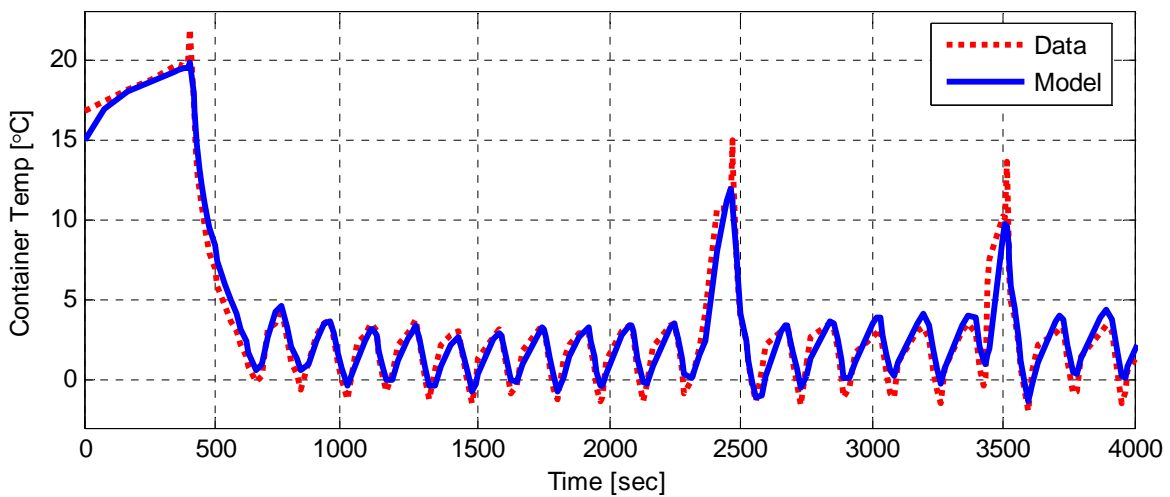
Figure 3.13   Environmental load model validation

32

3.4.3 On-Line Environmental Simulation

The environmental load model is implemented on-line during load emulation testing to determine how the experimental system is cooling the virtual container. The evaporator outlet air temperature, or supply air temperature to the virtual container, is measured and provided to the on-line environmental load model. The system disturbances and environmental conditions – such as ambient temperature, solar load, and wind speed - are inputs to the environmental load model and may be changed on-line during testing to represent dynamic conditions experienced in the field. The return air temperature output of the model captures the virtual load on the AC&R system. The return air temperature is the input to the emulation unit which places the virtual load on the experimental system through the mixing blade controller as presented in Figure 3.14.
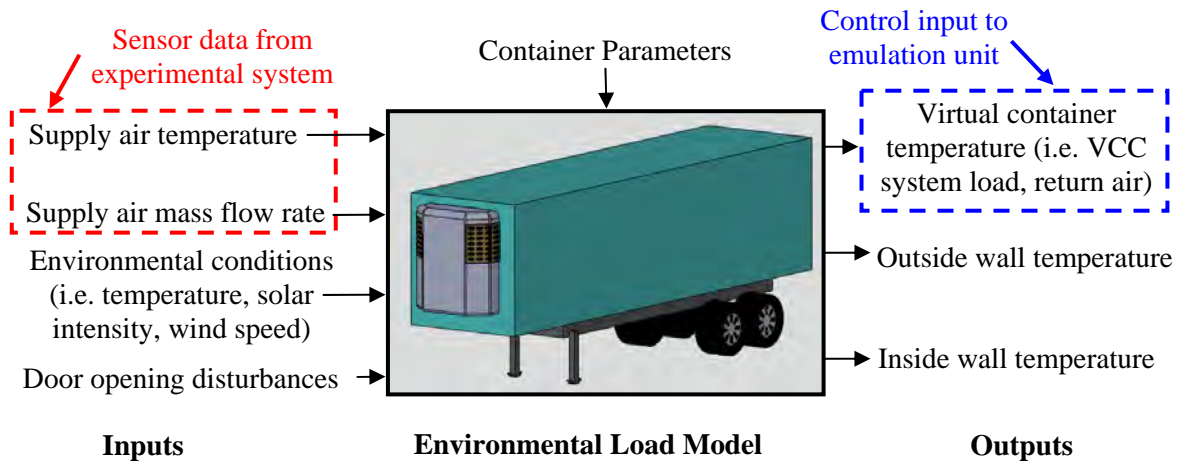

Figure 3.14   Environmental load simulation configuration

3.5   Load Emulation Control Loop

The load emulation control loop is shown in Figure 3.15 where sensor data is provided to the on-line simulation along with environmental conditions and container parameters. The output of the on-line simulation is the desired load on the AC&R system, which is equivalent to the evaporator inlet air temperature while making the assumption that the mass flow rate through the evaporator is constant. This assumption is reasonable since the humidity within the Mechanical Engineering Laboratory at the University of Illinois is maintained at a fairly constant level. The mixing blade control loop then tracks the desired load (i.e. inlet air temperature) on the experimental system through modulation of the mixing blade. The blade angle controller tracks

the desired blade angle through pulse width modulation of the DC motor coupled to the blade. The performance of the mixing blade controller and the blade angle controller play an essential part in accurately replicating the container and environmental conditions on the experimental AC&R system. The following subsections describe these control loops in detail.
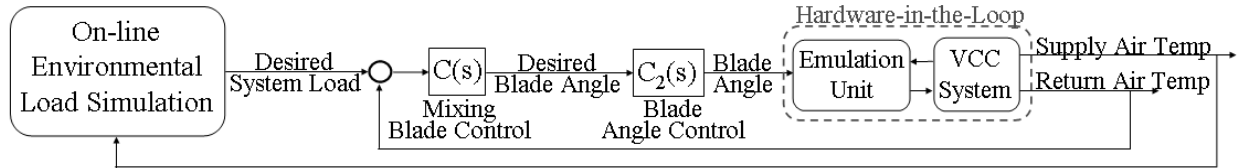
Figure 3.15   Hardware-in-the-loop load emulation control structure

## 3.5.1 Mixing Blade Control

This section details the identification of the emulation unit and the development of the mixing blade controller. To begin, the dynamics of the emulation unit are empirically identified in Section 3.5.1.1. The identified models provide a framework for the development of the mixing blade control loop shown in Section 3.5.1.2.

3.5.1.1 Emulation Unit Model Identification

The models in this section are empirically identified with data-based parameter identification techniques. An empirical modeling approach is used here since developing a first principles-based model would require substantial resources considering the complexities of the flow dynamics and heat transfer throughout the emulation unit. Therefore, empirical data is used to accurately identify the dynamics of the emulation unit for controller design purposes. The emulation unit shown in Section 3.3 is attached to the experimental test stand in the Mechanical Engineering Laboratory at the University of Illinois for identification.

The model between blade angle and inlet air temperature is first identified to understand the dynamics of the feedback path. Figure 3.16 shows open loop step response data from the experimental system where the compressor speed is fixed at 2000 RPM while the blade angle is stepped in angular increments of 10°. The blade angle is initially fully open at an angle of 90°. At this blade angle the evaporator air inlet temperature is equal to the ambient air temperature since the evaporator fan pulls in 100% ambient air since there is no mixing at this blade angle.

34

As the blade angle steps towards the closed position the evaporator inlet air temperature begins to decrease as an increased amount of cool outlet air is mixed with ambient air.
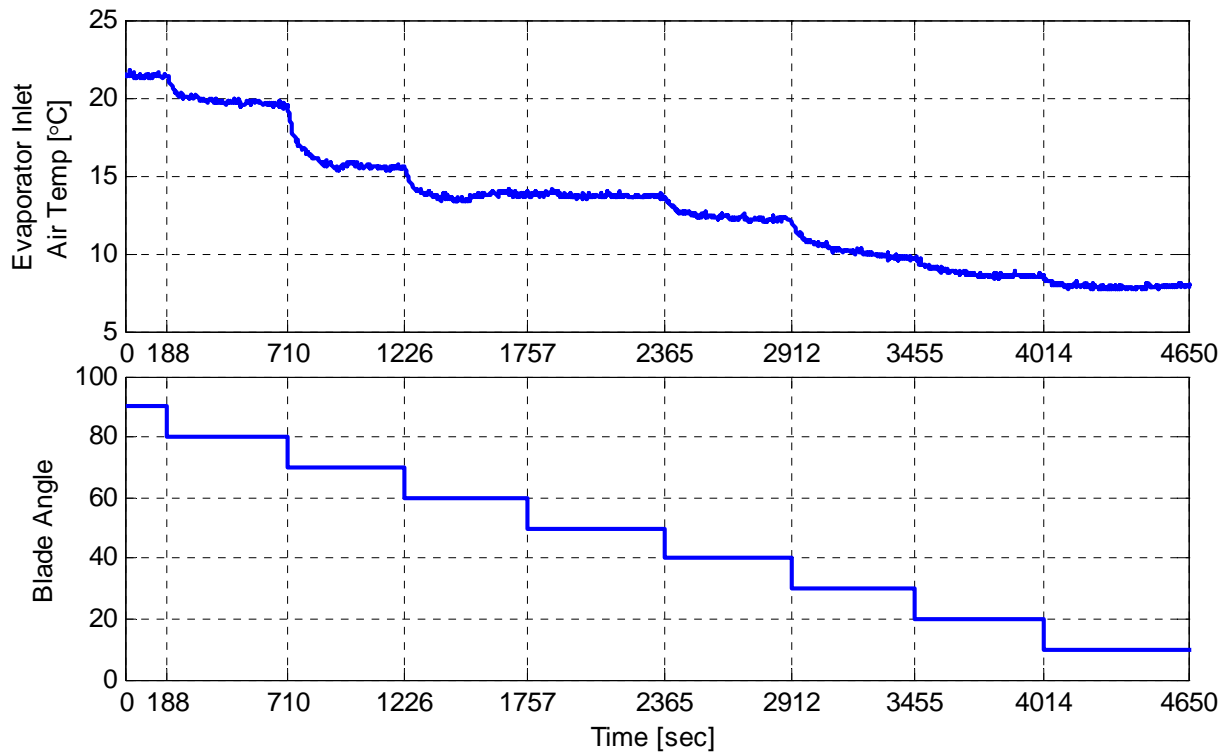
Figure 3.16   Open loop blade angle identification

To clearly show the input/output relation between blade angle and inlet air temperature Figure 3.17 plots a selected amount of data from the results shown in Figure 3.16. The nonlinear dynamics between blade angle and inlet air temperature can easily be seen in Figure 3.17 where the dynamics strongly depend on the absolute blade angle. For ease of comparison Figure 3.17 plots the change in inlet air temperature due to the blade angle variation on the y-axis, which should not be confused with the absolute inlet air temperature. The nonlinear correlation between blade angle and inlet air temperature becomes important during the development of the mixing blade controller and is quantitatively identified.

35
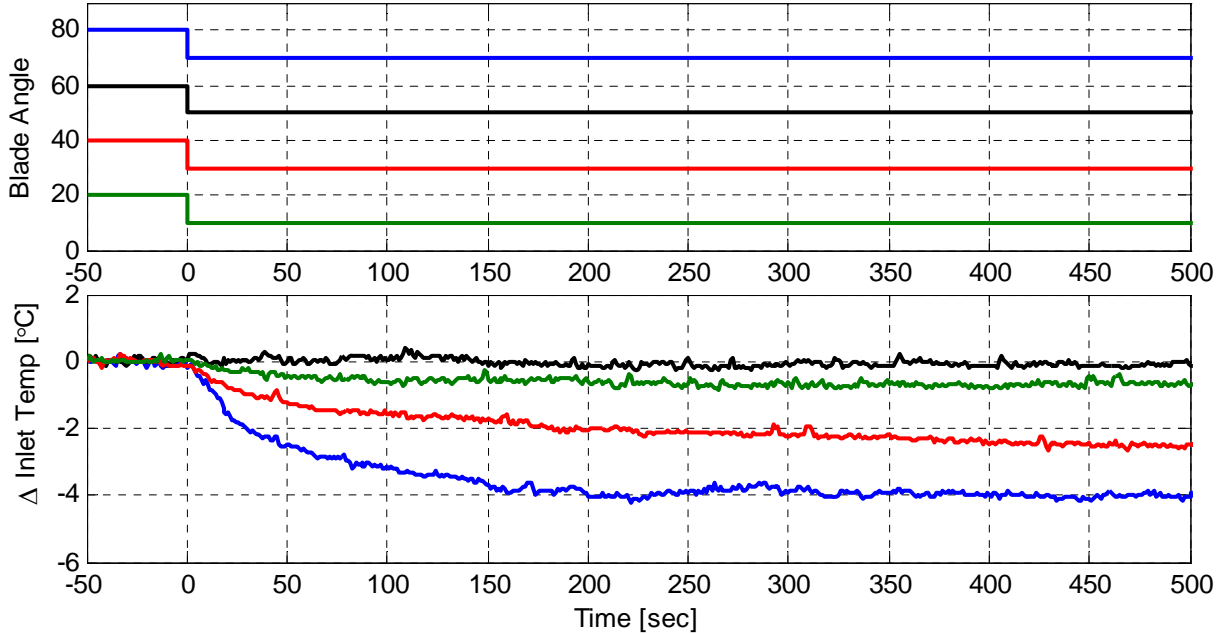
**Figure 3.17   Select blade angle identification data**

The response of the inlet air temperature to a change in blade angle is a first order response. Equation 3.9 shows a first order model where the input is blade angle θ_B, the output is evaporator inlet air temperature $T_{e,ai}$, M_θ is the amplitude of the model, and τ_θ is the time constant of the model. The model parameters are manually identified from the data shown in Figure 3.16 and are shown in Table 3.2. Due to the nonlinear response, this model is identified for different nominal blade angles. The amplitude of this model varies greatly, by a factor of 20, over the entire range of blade angles. Whereas the time constant of this model is relatively constant, varying by a factor of 3, over the entire range of blade angles.

$$\frac{T_{e,ai}}{\theta_B} = \frac{-M_\theta}{\tau_\theta s + 1}$$

(3.9)

Table 3.3   Blade angle to inlet air temperature model parameters

Nominal Blade Angle	Amplitude [°C]	Time Constant [sec]
85°	0.19	46
75°	0.40	53
65°	0.17	33
55°	0.02	n/a
45°	0.13	52
35°	0.26	106
25°	0.12	103
15°	0.07	81

For further clarity, Figure 3.18 plots the amplitude of the model shown in Equation 3.9 as a function of the nominal blade angle. This figure shows the strong nonlinear correlation between amplitude and nominal blade angle. The coupling between blade angle and inlet air temperature is strongest at nominal blade angles around 35° and 75°. The coupling is very weak around blade angles of 55°. These results are certainly repeatable for this design of the emulation unit while coupled to the experimental test stand. The dynamics are strongly nonlinear and more analysis is considered to understand the dynamics.
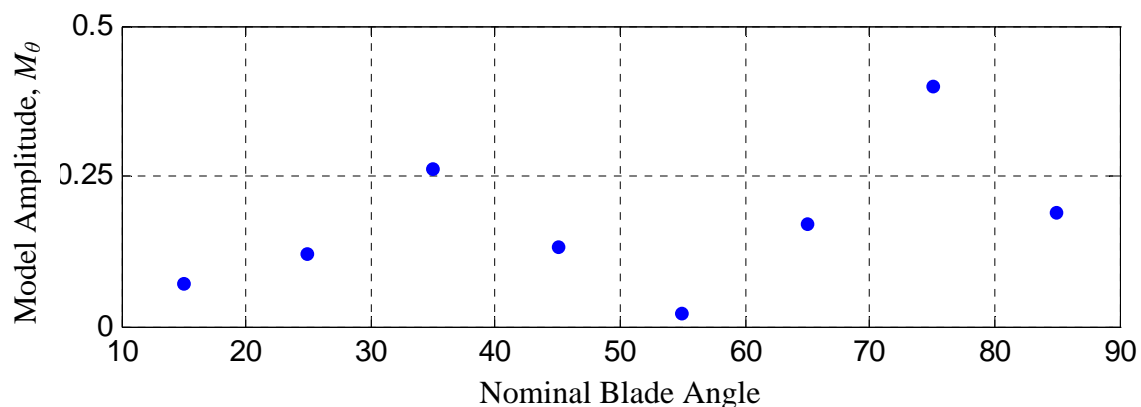

Figure 3.18   Blade angle to inlet air temperature model amplitude

To further understand the origins of the nonlinear relation between blade angle and inlet air temperature, the air flow within the emulation unit is investigated. A program called FloXpress is used to determine the flow profile throughout the emulation unit. FloXpress is a

computational fluid dynamics (CFD) application that determines how fluid flows through parts/assemblies. This application is part of the solid modeling program SolidWorks.

The emulation unit is configured within *FloXpress* to determine the flow profile given the fluid properties of air and the flow rate through the evaporator. The simulation output is shown in Figure 3.19 where the blade angle is fully open at an angle of 90°. The solid lines show the calculated air flow trajectories throughout the emulation unit where the color of the line represents the air flow velocity at that point corresponding to the legend.
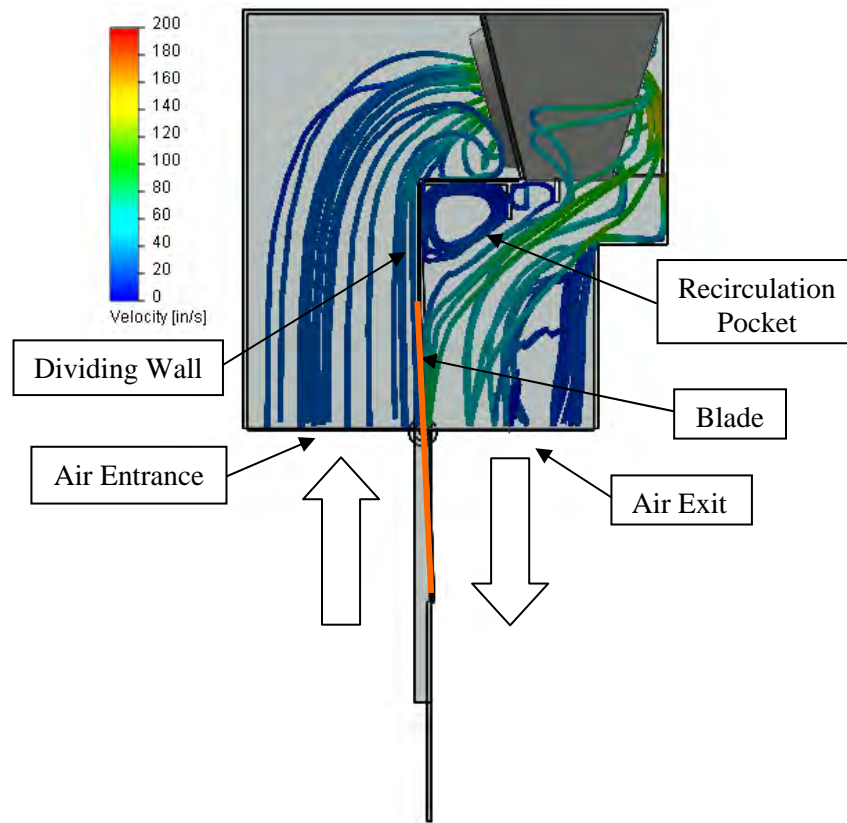
Figure 3.19   FloXpress simulation of air flow through the emulation unit

To describe the flow through the emulation unit in more detail, the air flows into the unit on the left hand side with a uniform velocity profile. The air increases in velocity as it flows through the evaporator and into the right portion of the emulation unit. The air hits the right side wall and then flows downward and to the left toward the exit at the bottom.   Two flow trajectories exist which flow around the side of the evaporator before heading toward the exit. These two flow trajectories result since there is a flow path on either side of the evaporator due

to the design. There also exists a recirculation pocket, or eddy current, in the upper left corner of the exit where the flow is nearly stagnant. At the exit of the emulation unit the air has a non-uniform flow profile. The air close to the interior dividing wall has a large velocity in the range of 60 to 100 in/sec., whereas the air on the right side of the exit has a small velocity in the range of 0 to 20 in/sec. This non-uniform flow profile is one cause for the strong nonlinear relationship between blade angle and inlet air temperature.

From the CFD results an illustration of the air flow rate profile at the exit of the evaporator is created and shown in Figure 3.20. When the blade is vertical the inlet temperature is more sensitive to blade angle changes due to the larger air flow rate close to the center dividing wall. On the other hand, the inlet air temperature is less sensitive to blade angle changes when the blade angle is further from the vertical position due to the decreased air flow rate. When the blade angle approaches horizontal, or closed, the sensitivity between blade angle and inlet air temperature begins to increase. One reason for this is from the closed loop which is formed between the inlet and outlet of the evaporator where the air is continually cooled by being passed through the evaporator.
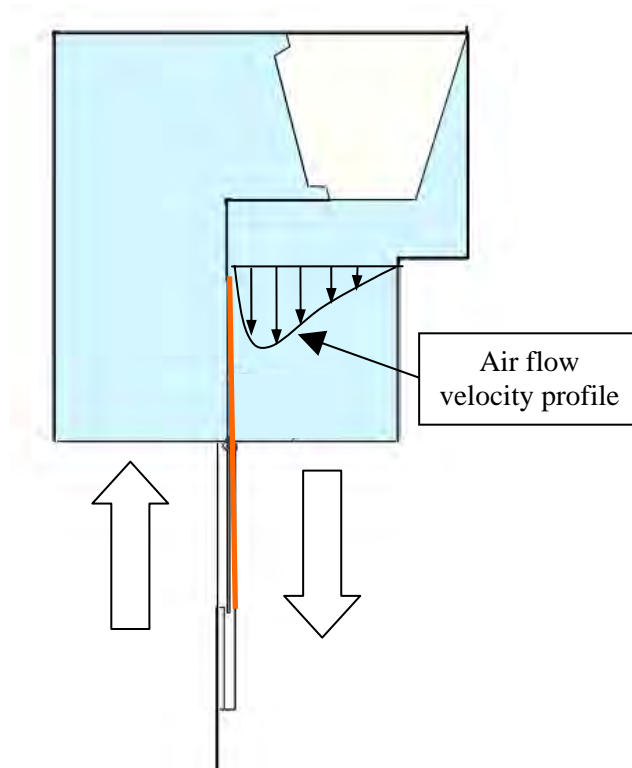

Figure 3.20   Air flow velocity profile at the emulation unit exit

Another cause for the nonlinear dynamics between the blade angle and inlet air temperature is from the relation between the blade angle and mixing width, W_M. The mixing width is the measurement between the center dividing wall and the tip of the blade as shown in Figure 3.21. The mixing width is important since this dimension influences the amount of outlet air which is redirected toward the inlet. Figure 3.22 shows the correlation between the blade angle and the mixing width which has been determined from simple geometry. The radius of the blade is 9 inches making the mixing width 9 inches at a blade angle of 0°. Ideally this correlation would be linear; however this is a nonlinear relation where changes in the blade angle at large absolute angles result in relative large changes in the mixing width. Therefore, this nonlinear relation is another cause for the nonlinear dynamics observed between the blade angle and the inlet air temperature.
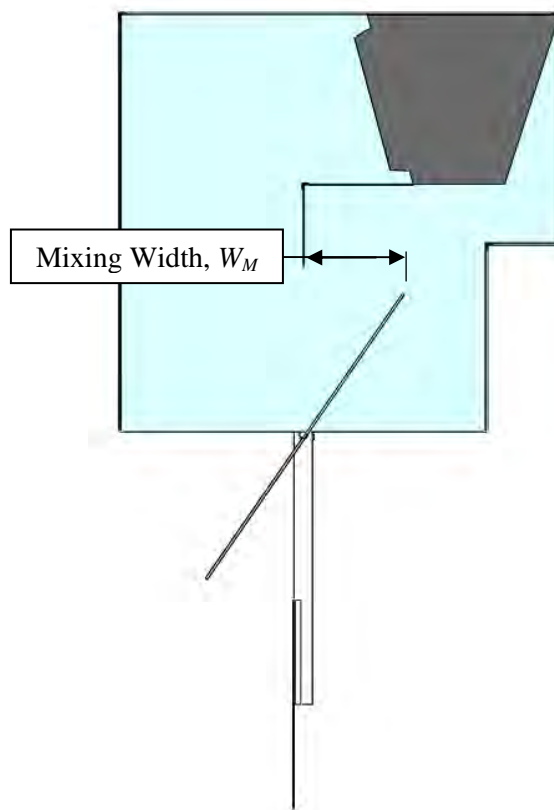
Mixing Width, W_M

**Figure 3.21   Mixing width dimension**
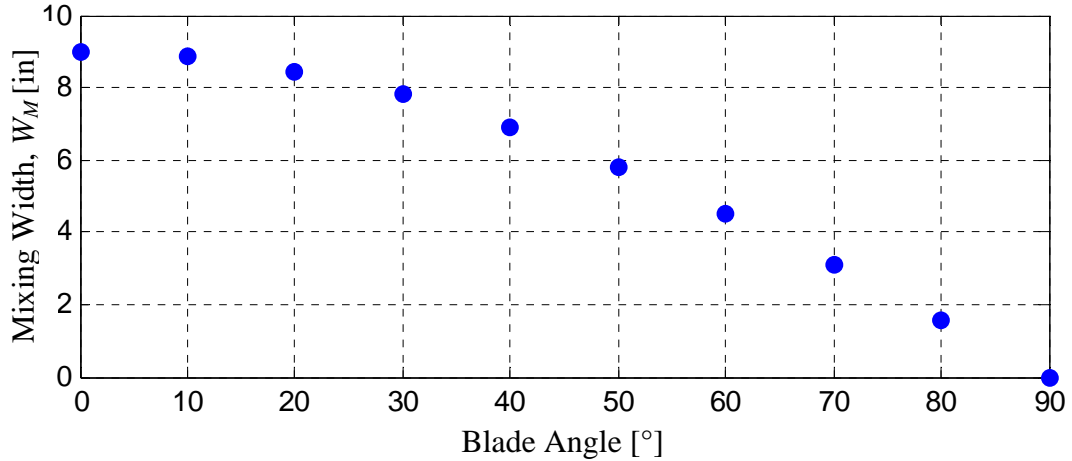
Figure 3.22   Nonlinear mixing width relation

From these results it is clear that the model between blade angle and evaporator inlet air temperature is strongly dependent on the design of the emulation unit itself. The identification shown in this section is therefore only accurate for the emulation unit under investigation. A different emulation unit design will still exhibit the same general coupling between blade angle and inlet air temperature, however the degree of nonlinearity may be different.

One significant disturbance to the mixing blade control loop is variations in compressor speed. A change in the compressor speed influences the capacity of the system which in turn changes the outlet air temperature, which finally affects the inlet air temperature due to the mixing dynamics. Therefore, large changes in compressor speed cause the inlet air temperature to deviate from set point which reduces the tracking performance of the mixing blade control loop. Therefore the model between compressor speed and inlet air temperature is investigated to better understand the coupling effects for the development of a feedforward element for the mixing blade control loop.

Figure 3.23 shows open loop step response data collected from the experimental system where the compressor speed is stepped from 2000 RPM to 1500 RPM while the blade angle is fixed at three different angles as shown in the legend. This figure shows that there is indeed coupling between the compressor speed and the evaporator inlet air temperature. This figure also shows that the dynamics are nonlinear and depend on the blade angle. For clarity, the y-axis in Figure 3.23 is the change in inlet air temperature due to a compressor speed change which should not be confused with the absolute inlet air temperature.
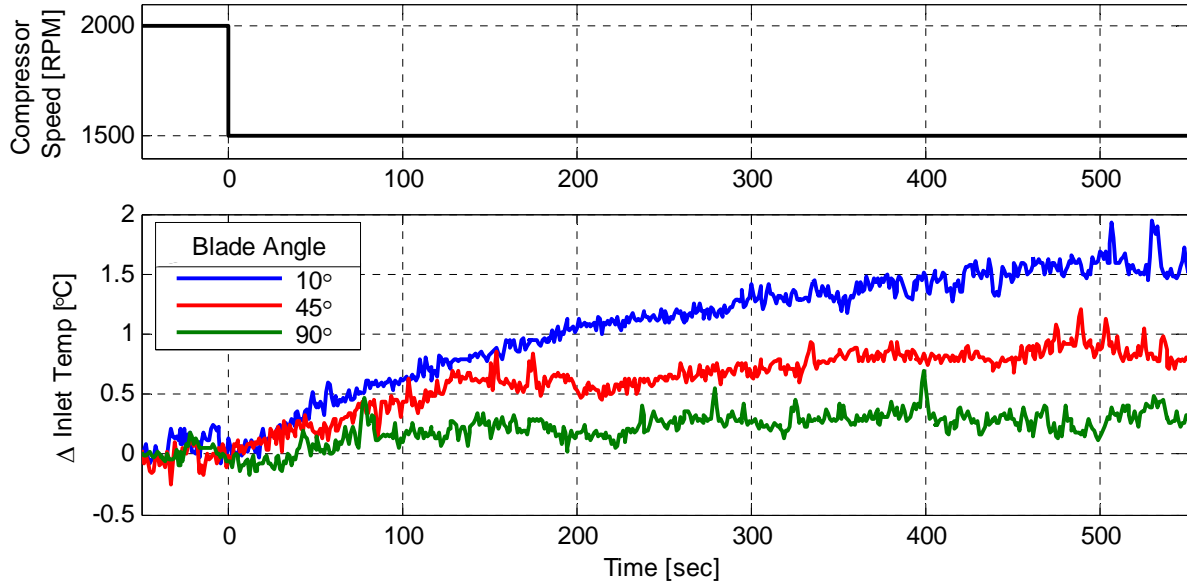
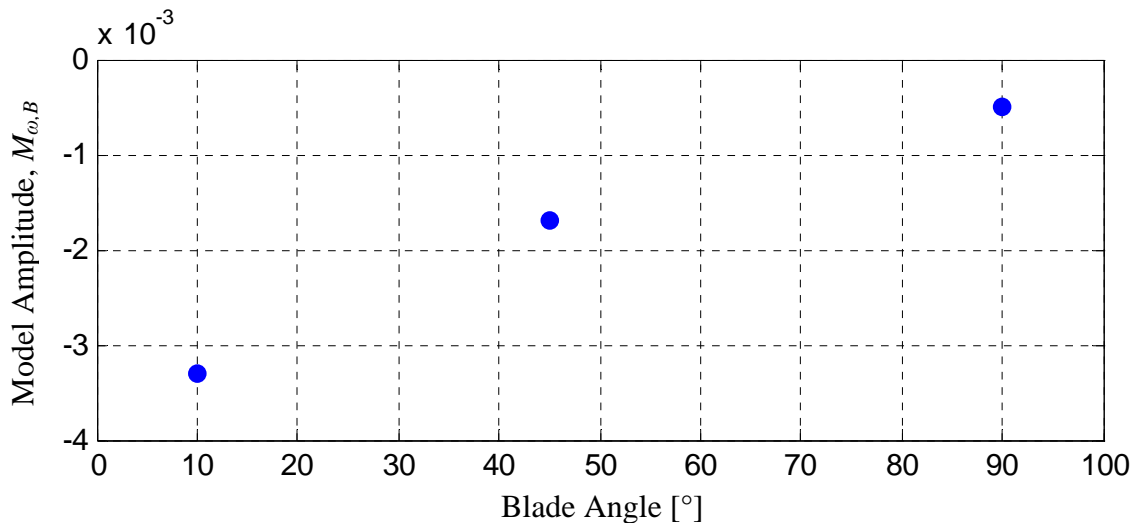**Figure 3.23 Compressor speed to inlet air temperature identification**

The response of inlet air temperature to a change in compressor speed exhibits that of a first order response. Equation 3.10 shows this model where the input is compressor speed ω, the output is inlet air temperature $T_{e,ai}$, $M_{\omega,B}$ is the amplitude of the model, and where $\tau_{\omega,B}$ is the time constant of the model. The model parameters are manually identified using the data shown in Figure 3.23 and reported in Table 3.3. Due to the nonlinear dynamics, this model is identified based on the blade angle. The model amplitude varies greatly, by a factor of 60, across the range of blade angles. The model time constant is relatively constant varying by a factor of 1.5 across the range of blade angles.

$$\frac{T_{e,ai}}{\omega} = \frac{-M_{\omega,B}}{\tau_{\omega,B}s+1} \qquad (3.10)$$

Table 3.4 Compressor speed to inlet air temperature model parameters

Blade Angle	Amplitude [°C]	Time Constant [sec]
90°	-0.0005	150
45°	-0.0017	152
10°	-0.0033	215

42

Figure 3.24 plots the amplitude of Equation 3.10 as a function of the nominal blade angle. The absolute value of the model amplitude is largest for small blade angles. This indicates strong coupling between compressor speed and inlet air temperature while the blade angle is small. This relation can be explained by considering the air flow profile throughout the emulation unit, refer to Figure 3.5 for flow illustrations. When the blade angle is at 90° the inlet and outlet of the evaporator are completely decoupled since there is no mixing of outlet air and ambient air. Since the evaporator fan pulls in 100% ambient air, any fluctuations in the outlet temperature do not influence the inlet air temperature. This is observed in the experimental data where changes in compressor speed have little effect on the inlet air temperature for large blade angles. For a blade angle of 0° the evaporator fan pulls in 100% evaporator outlet air. Since compressor speed fluctuations influence the outlet air temperature, any changes in compressor speed also influence the inlet air temperature while the blade angle is small. This is observed in the experimental data where there is strong coupling between compressor speed and inlet air temperature at small blade angles as shown in Figure 3.24.

Figure 3.24   Amplitude of compressor speed to inlet air temperature model

3.5.1.2   Mixing Blade Control Development

This section details the design of the mixing blade control loop based on the identification of the emulation unit shown in Section 3.5.1.1. The input to the mixing blade control loop is the error between the desired inlet air temperature and the measured inlet air

temperature. The output of the mixing blade controller is the desired blade angle which is the input to the blade angle controller; refer to Figure 3.15.

The nonlinear dynamics between the blade angle and the inlet air temperature is considered during the design of the feedback controller. One possible method to account for the nonlinear dynamics would be through the development of a gain scheduled feedback controller. The gain scheduled feedback controller is constructed by interpolating between a family of local controllers depending on the state of the scheduling variable. In this case the blade angle would be the ideal scheduling variable since the blade angle strongly influences the plant dynamics. Each local controller is tuned to maintain stability and set point performance. An interpolation method is also designed to allow the global controller to effectively interpolate the output of the local controllers depending on the state of the scheduling variable.

The development of a gain scheduled feedback controller for this application is time intensive due to the non monotonic plant trends which would require many local controllers. Moreover, using a feedback gain scheduling controller for the mixing blade control loop is excessive since such a high performance over the entire range of blade angles is not necessary for tracking the slow temperature dynamics of the reference. The dynamics of the reference are relatively slow since the time constant of virtual container is larger than the time constant of the emulation unit. This is nearly always the case since the volume of the virtual container is larger than the volume of the emulation unit itself.

Therefore a different control method is pursued where a conservatively tuned controller is implemented which maintains stability over the entire range of blade angles while also being able to accurately track references signals. The conservatively tuned feedback controller is a proportional-integral type which has been tuned heuristically to give satisfactory tracking performance while maintaining stability across the range of blade angles. A heuristic tuning method is used for tuning since this controller merely needs to track a temperature reference with a certain degree of performance while maintaining stability.

The coupling between compressor speed and inlet air temperature may be decoupled with a feedforward element to improve inlet temperature tracking during compressor speed fluctuations. In this scenario, a scheduled feedforward compensator is required to effectively compensate a compressor disturbance over the entire range of blade angles due to the nonlinear

dynamics between compressor speed and inlet air temperature. Figure 3.25 shows the structure of the feedforward compensator which uses both of the models identified in Section 3.5.1.1. Equation 3.11 shows the form of the blade angle feedforward compensator, $G_{FF,B}$.
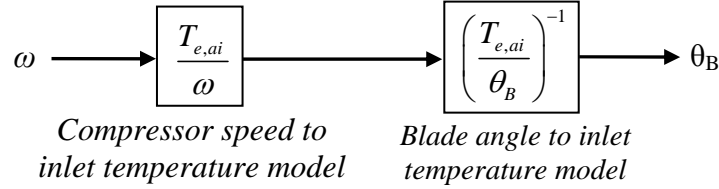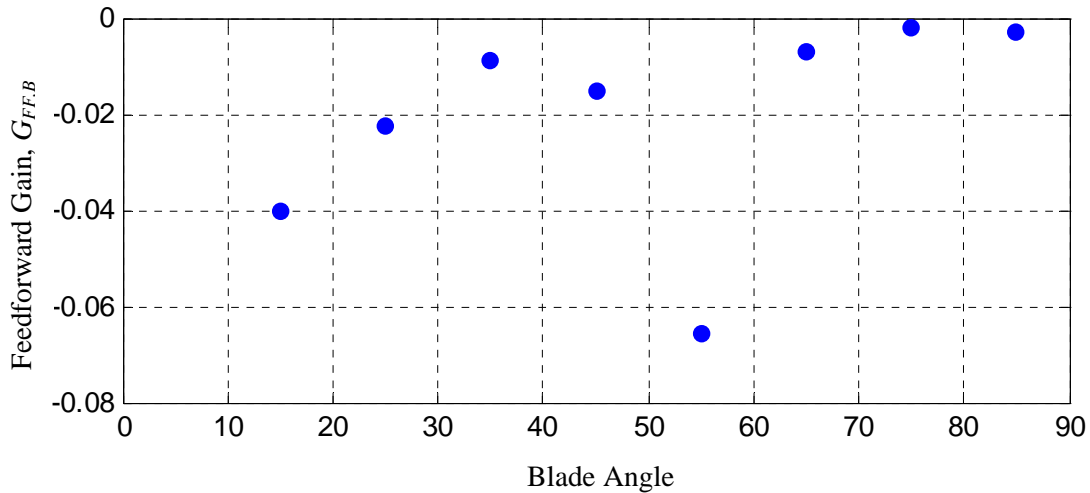

Figure 3.25   Mixing blade feedforward compensator

$$G_{FF,B} = \frac{T_{e,ai}}{\omega}\left(\frac{T_{e,ai}}{\theta_B}\right)^{-1} = \frac{M_{\omega,B}}{\tau_{\omega,B}s+1} \cdot \frac{\tau_\theta s+1}{M_\theta}$$

(3.11)

Since the time constants of the two models are on the same order of magnitude, on the order of 100 seconds, there is not a significant loss in dynamics by cancelling the time constants. This allows the feedforward compensator to be reduced to single gain as shown in Equation 3.12 where the amplitude of the model between compressor speed and inlet air temperature is divided by the amplitude of the model between blade angle and inlet air temperature. Equation 3.12 includes the nonlinear dynamics of these models since the amplitude of the models are shown to depend on the absolute blade angle.

$$G_{FF,B} = \frac{M_{\omega,B}(\theta_B)}{M_B(\theta_B)}$$

(3.12)

The feedforward compensator is increased in complexity since both of these models are nonlinear. The feedforward compensator is identified for a range of blade angles based on the model parameters shown in Table 3.2 and Table 3.3. Figure 3.26 shows the feedforward gain as a function of the absolute blade angle. This figure shows that the feedforward gain is not monotonic. This is due to the strong nonlinearity between blade angle and inlet air temperature as shown previously in Figure 3.18.

Figure 3.26   Mixing blade feedforward schedule

To maintain a level of simplicity a feedforward compensator is implemented using a static gain across all blade angles. One reason this is done is to ensure that the user may easily troubleshoot the control loop in the case of any temperature tracking issues. Also, reducing the feedforward compensator to a static gain does not impact performance significantly since the compressor typically changes speed slowly relative to the dynamics between blade angle and inlet air temperature. Later in this chapter Figure 3.37 shows a variable speed load emulation test where the compressor speed changes from 2000 RPM to 800 RPM in approximately 200 seconds. In this case, scheduling the feedforward gain as shown in Figure 3.26 is not necessary since the feedback control loop will compensate for any performance that has been sacrificed by the use of the static feedforward gain. The gain of the feedforward compensator is taken to be -0.01 and is shown later in this chapter to work well for temperature tracking as shown in the variable speed emulation results presented in Figure 3.37.

The final control structure for the mixing blade control loop is shown in Figure 3.27. This control configuration is referred to as the variable speed mixing blade control loop since this configuration accounts for the compressor speed during regulation. This figure shows the PI feedback controller along with the feedforward element influencing the desired blade angle based on the compressor speed. The output of the variable speed mixing blade control loop is the desired blade angle. The desired blade angle is the input to the blade angle controller as shown previously in Figure 3.15.
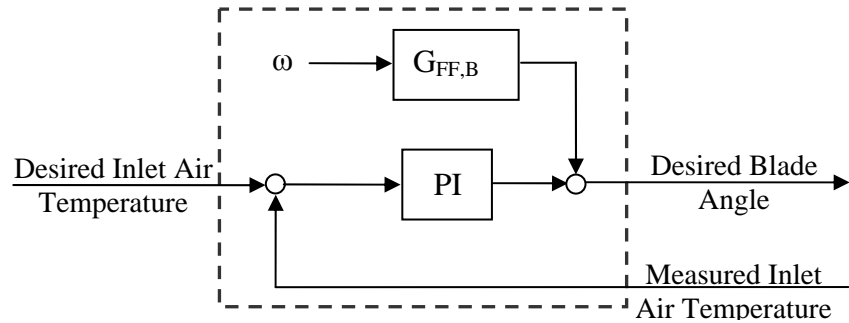
Figure 3.27   Variable speed mixing blade control loop

The control configuration shown in Figure 3.27 works well during the emulation of a variable speed AC&R system.   However, when the variable speed mixing blade control configuration is implemented during the emulation of an on-off AC&R system the temperature tracking is insufficient due to the sharp changes in temperature reference during the on-off transitions and the loss of the evaporator cooling. Figure 3.28 shows a load emulation result from an on-off AC&R system where the variable speed mixing blade control loop in Figure 3.27 is implemented for temperature tracking. The highlighted portion of this figure shows the off portion of the cycle where the variable speed mixing blade control loop allows the temperature to severely overshoot the reference temperature. The poor temperature tracking is partly due to the lack of cold air supply. When the system is off, any overshoot during temperature tracking is not recoverable since there is a lack of cool air from the outlet of the evaporator. Therefore, a unique control procedure is specifically developed for on-off load emulation to improve temperature tracking performance.
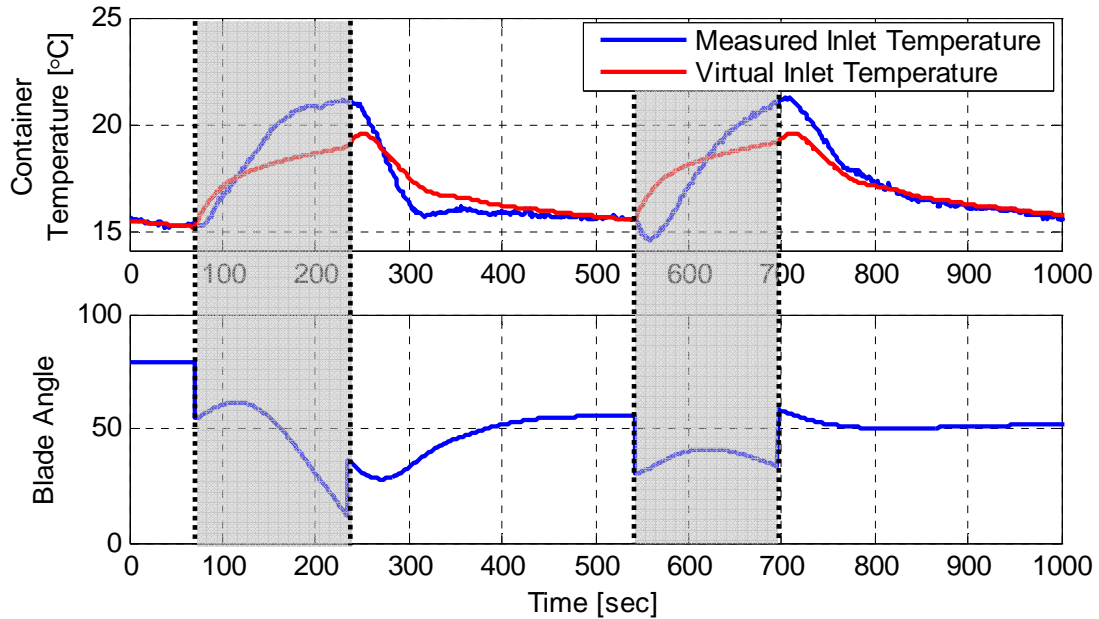
Figure 3.28   Poor regulation during on-off cycling using the variable speed mixing blade control loop for an on-off AC&R load emulation test

The on-off mixing blade controller has been designed with a feature to completely close the blade during certain conditions to retain the cold air within the emulation unit to prevent large overshoots in temperature. Figure 3.29 shows the configuration of the on-off mixing blade control loop where a PI controller is used for temperature regulation while the system is on. While the system is off two different feedback paths are switched between depending on the sign of the error. During a positive error a PI control procedure is in the feedback path and during a negative error the blade is closed to an angle of 0°. The PI controllers in the on-off mixing blade control configuration use the same gains as discussed previously for the variable speed mixing blade controller. The same gains are used for the PI controllers since the dynamics between blade angle and inlet air temperate remain the same.

The following paragraph describes the off cycle portion only of the on-off mixing blade control loop. When the measured inlet air temperature is greater than the desired inlet air temperature, referred to as state 1, the off configuration completely closes the blade to an angle of 0°. On the other hand, when the measured inlet air temperature is smaller than the desired temperature, referred to as state 2, the off configuration uses a PI controller for temperature tracking. When state 1 is switched to from state 2, this occurs during a temperature overshoot

48

when the system is off, the output of the mixing blade controller switches from the PI controller to the blade closed output. In this scenario, the output of the mixing blade controller simply changes from the PI output to 0°. Alternatively, when state 2 is switched to from state 1, this occurs when the measured inlet air temperature becomes smaller than the desired inlet air temperature while the system is off, the controller switches from the blade closed state to the PI controller initiated with an output angle of 30°. The PI controller is initiated at this angle to improve temperature tracking since without this feature the PI controller would take a significant amount of time to open the blade to an angle necessary to increase the inlet air temperature. The magnitude that the PI controller is initiated to may be tuned based on the virtual temperature of the emulation test. For example, during a low temperature emulation test the blade angle may be initiated to a small angle to retain the cool air within the emulation unit to prevent a potential temperature overshoot. Initiating the PI controller at an angle of 30° has been found to effectively track temperature references during on-off emulation for a range of temperatures.
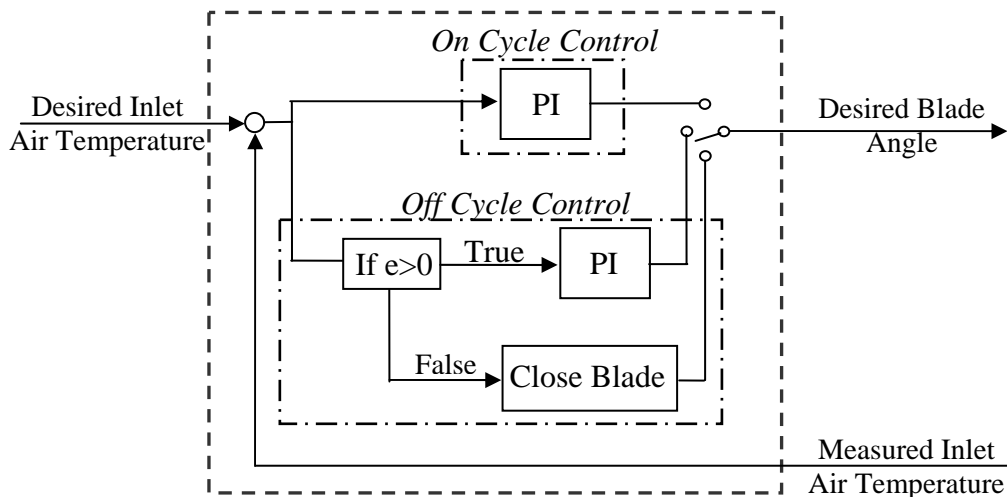
Figure 3.29   On-off mixing blade control loop

Figure 3.30 shows the improved tracking performance during on-off load emulation when the on-off mixing blade control loop is implemented. The shaded region in this figure shows the off cycle of the emulation where the on-off mixing blade control configuration switches between the blade closed state and the PI controller. When the PI controller is switched to from the blade closed state the blade angle is initiated at 30° which is then followed by the PI control procedure. During the off cycle the blade transitions between the closed state and the PI control procedure

49

frequently. It transitions about six times between the closed state and the PI control procedure during a 150 second period. A hysteresis or dead-band method may be implemented on the temperature error during tracking to reduce the blade actuation frequency during the off cycle. Certainly, a method such as this would minimize the number of transitions between the closed state and the PI control procedure while sacrificing temperature tracking performance.
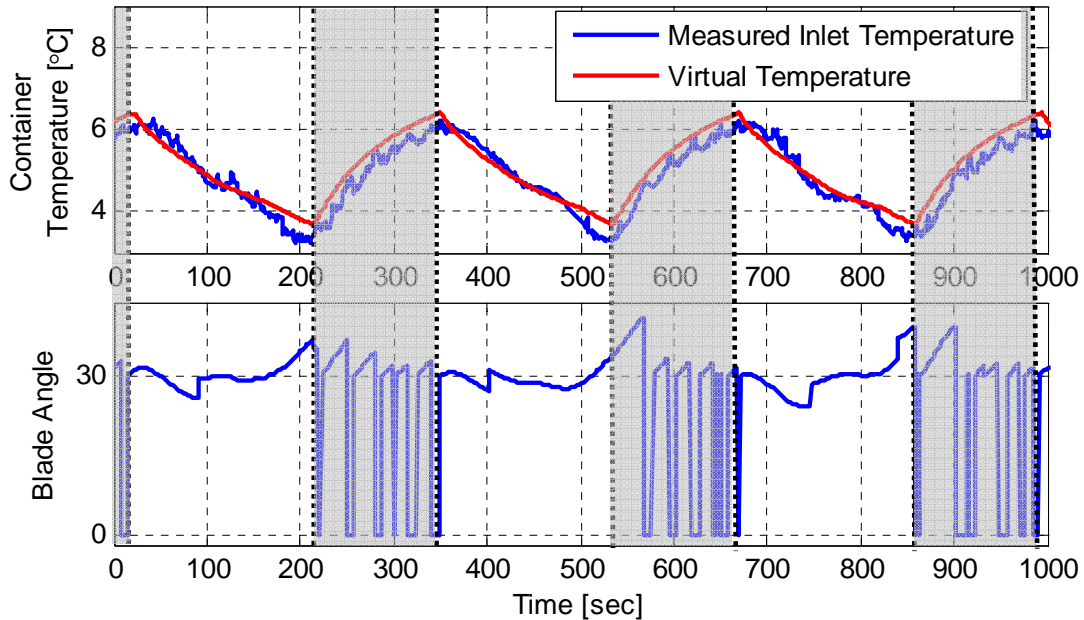

Figure 3.30   Improved on-off emulation with logic controller

3.5.2 Blade Angle Control

The blade angle control loop is the portion of the load emulation configuration which takes in the desired blade angle from the mixing blade control loop and outputs a duty cycle to the DC motor. The duty cycle controls the speed and direction of the motor which is used to track the desired blade angle. A heuristically tuned proportional-integral controller is used for this framework. A heuristic tuning approach is used since this controller needs only to track a desired blade angle while maintaining stability. To improve blade angle tracking, a friction compensation element is implemented to reduce the friction effects associated with the geared DC motor. Figure 3.32 presents experimental results showing the blade angle closely tracking the desired blade angle during a load emulation experiment.
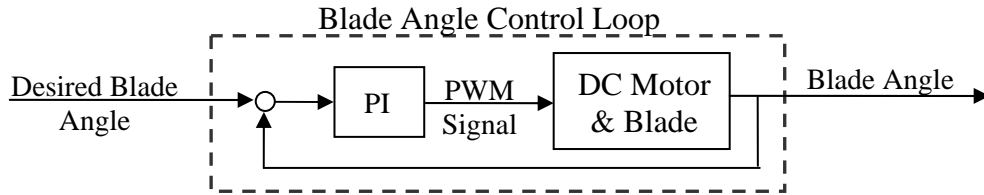
Figure 3.31   Blade angle control loop
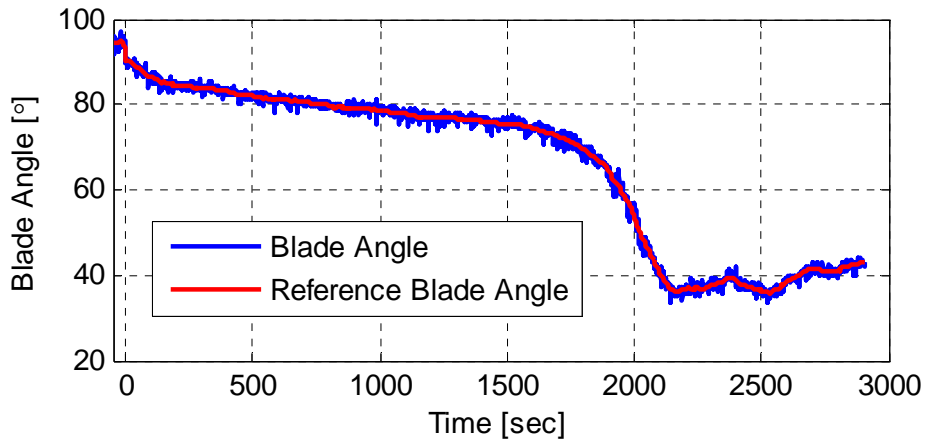
Figure 3.32   Blade angle during emulation

3.6   Load Emulation Results

This section provides load emulation results from the experimental test stand at the University of Illinois virtually cooling a large truck environment. An emulation unit is attached to the evaporator of the experimental test stand and the system is configured to virtually cool the truck environment with on-off control as shown in Figure 3.33. The on-off control framework turns the AC&R system on and off based on temperature measurements from the container. If the temperature is below the lower hysteresis set point the system is turned off. When the temperature rises above the higher hysteresis set point the system is turned on until the temperature drops below the lower set point again.
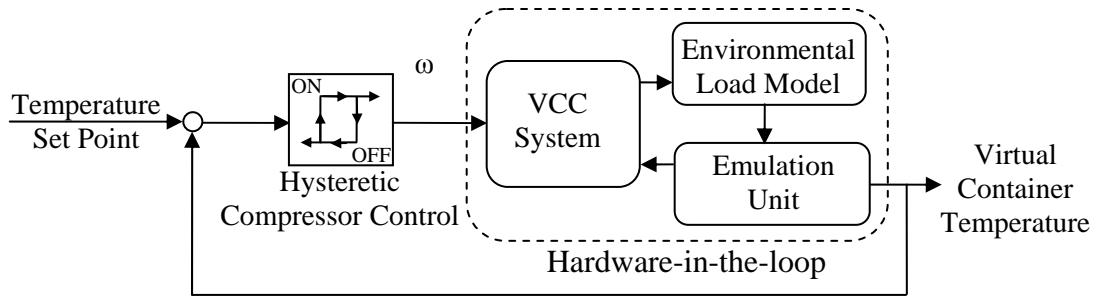
Figure 3.33   On-off container temperature control configuration

Figure 3.34 presents load emulation results from the air conditioning test stand virtually cooling a truck environment during a cloudy day with an ambient temperature of 25°C.   The virtual container temperature begins at 25°C and is pulled down to the temperature set point of 16.5±1.5°C where this temperature is maintained by on-off compressor cycling.   As shown, the emulation unit is able to effectively place this virtual load on the AC&R system. However, there does exist extreme conditions (i.e. extremely hot day) that load emulation is not capable of accurately simulating due to temperature limitations. For example, the largest attainable inlet air temperature is equal to that of the surrounding air as discussed in Section 3.3. In this results, the evaporator inlet air temperature tracks the virtual container temperature through the mixing blade controller which modulates the blade angle.   As the container temperature is pulled down, the blade angle slowly decreases to meet the inlet air temperature set point. In order to track the virtual container temperature, the blade angle has large variations during the on-off cycling due to the structure of the on-off mixing blade controller discussed in Section 3.5.1.2. This data is extremely useful in determining the performance of the AC&R system in terms of cool down time, compressor cycling frequency, and energy consumption. Load emulation may also be used in determining the performance of control loops such as the capacity control loop or the superheat control loop which is discussed in Chapter 6.

To illustrate the flexibility of testing systems with load emulation, Figure 3.35 presents emulation results with door opening disturbances. The door opening event represents the disturbance to the system when the truck environment is exposed to ambient air during the transfer of goods in/out of the cooled space. This disturbance may be used to investigate how a controller will respond to large temperature deviations or how much additional energy is consumed during each door opening event.
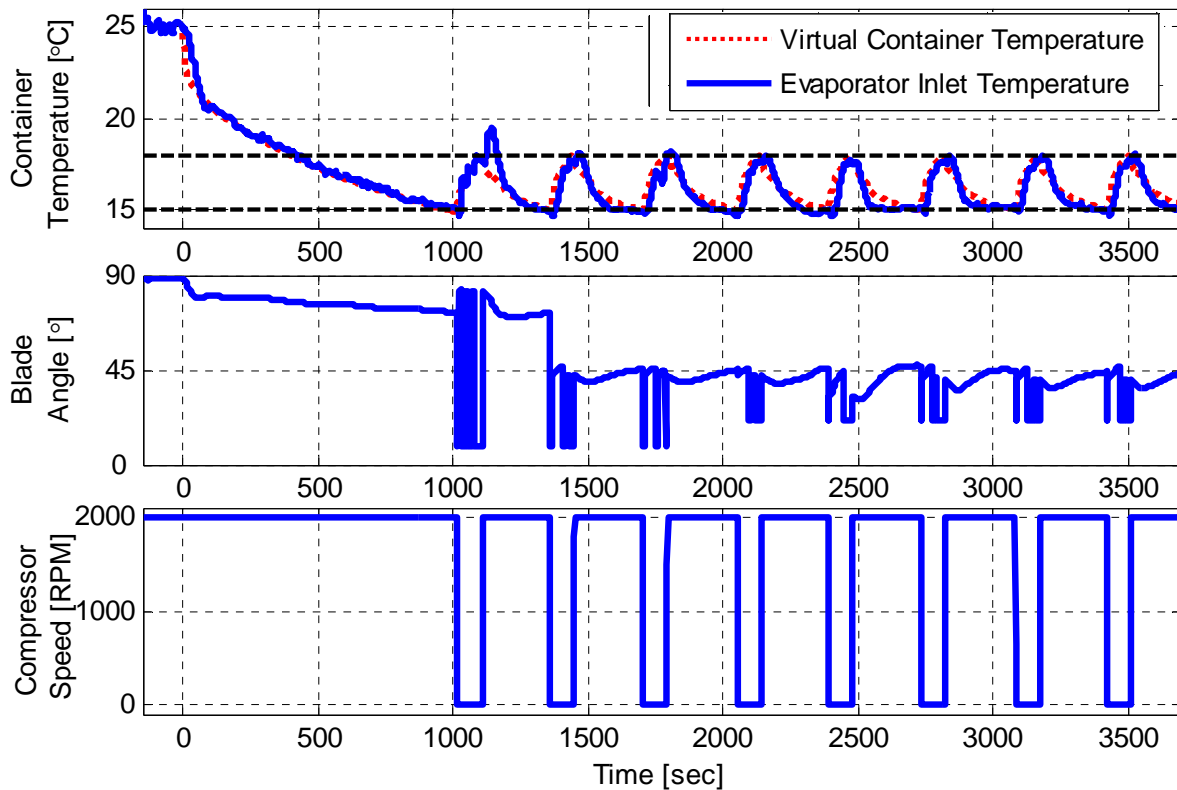
Figure 3.34   AC&R test bed virtually cooling a truck environment with on-off control using hardware-in-the-loop load emulation

53
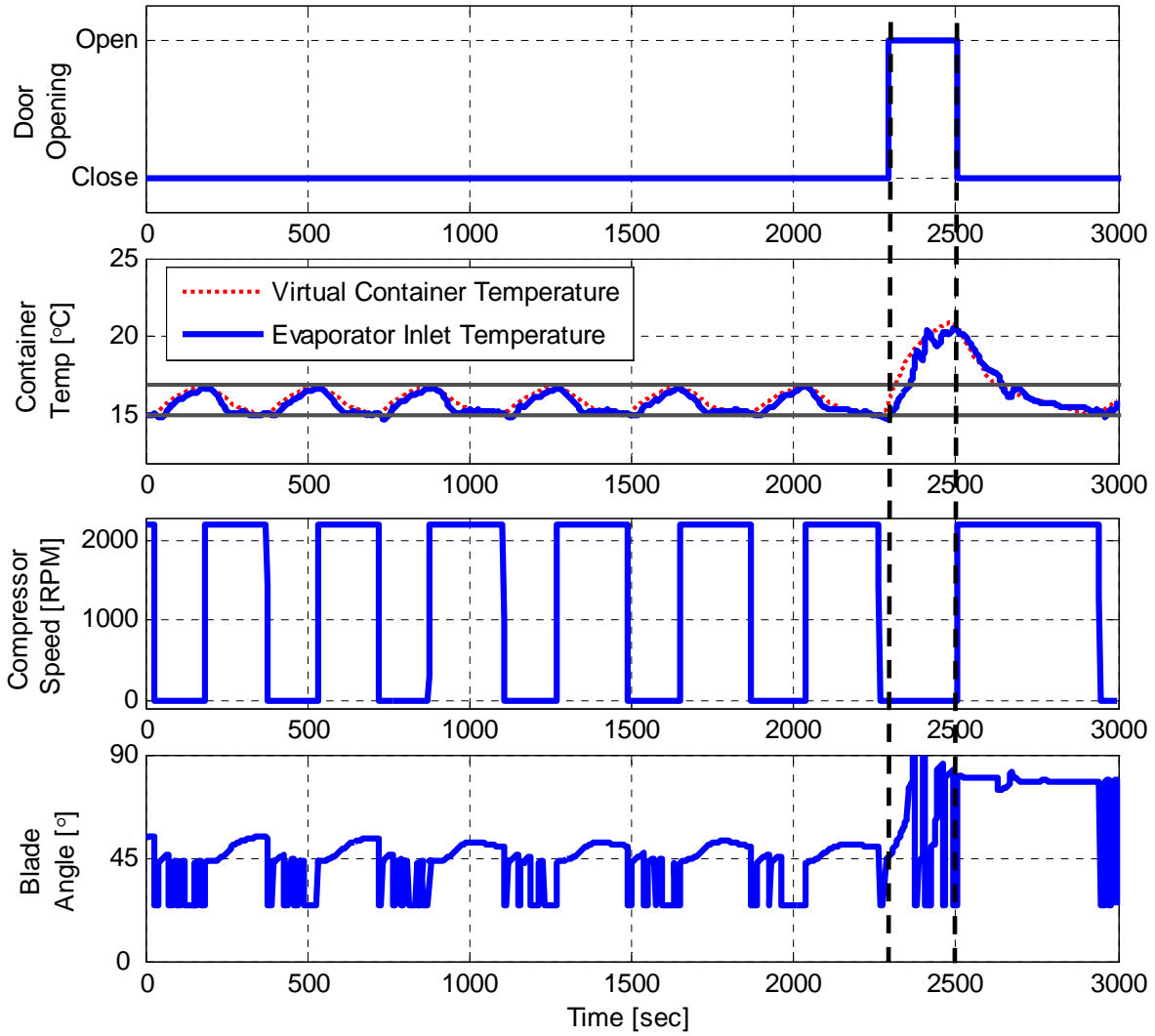
Figure 3.35   Door opening disturbance using hardware-in-the-loop load emulation
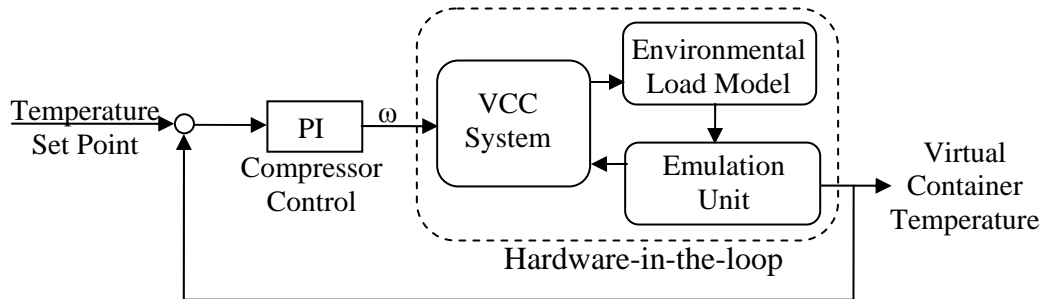
Figure 3.36   Variable speed container temperature control configuration

Hardware-in-the-loop load emulation may also be used to analyze the performance of variable speed systems. With variable speed systems the compressor speed is modulated to meet

54

capacity demands set by the user. Typically the user inputs a set point temperature to the control loop which minimizes the error between the temperature set point and the measured container temperature. A heuristically tuned proportional-integral controller is used to regulate the compressor speed to meet the temperature set point as shown Figure 3.36.

Figure 3.37 presents results of the air conditioning test stand in a variable speed configuration virtually cooling a truck environment on a cloudy day with an ambient temperature of 25°C. The virtual container temperature begins at 25°C and is pulled down to the set point of 16.5°C. During this time the temperature control loop varies the compressor speed to meet the temperature set point. Hardware-in-the-loop load emulation allows performance characteristics to be identified without having to place the air conditioning unit and real container within a test chamber.
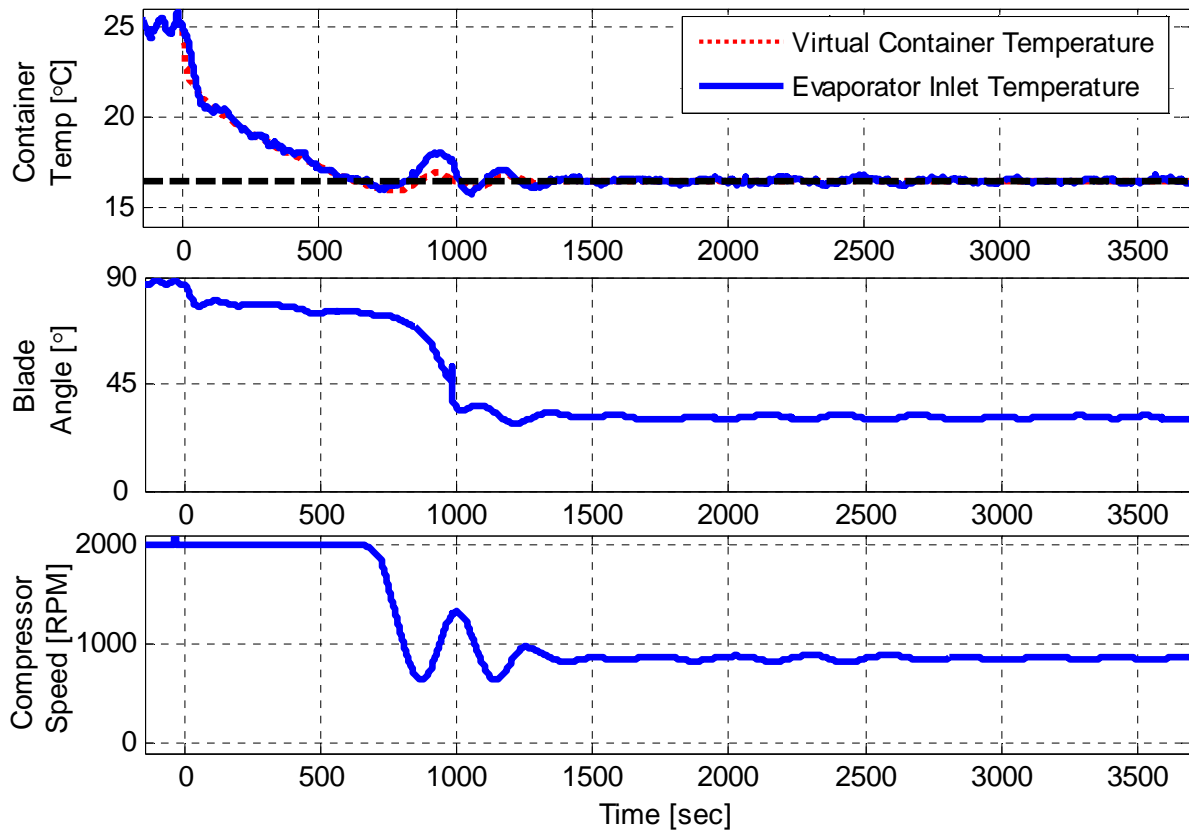
Figure 3.37   AC&R test bed virtually cooling a truck environment with variable speed control using hardware-in-the-loop load emulation

Figure 3.38 further highlights the flexibility of the load emulation testing environment by testing the experimental test stand while virtually cooling the truck environment to varying ambient conditions. A decrease in the ambient temperature causes a deviation of the virtual container temperature from the set point temperature which drives the temperature control loop to decrease the compressor speed. These emulation results allow for performance evaluation of the AC&R system, components, and control loops that would normally require large test chambers.
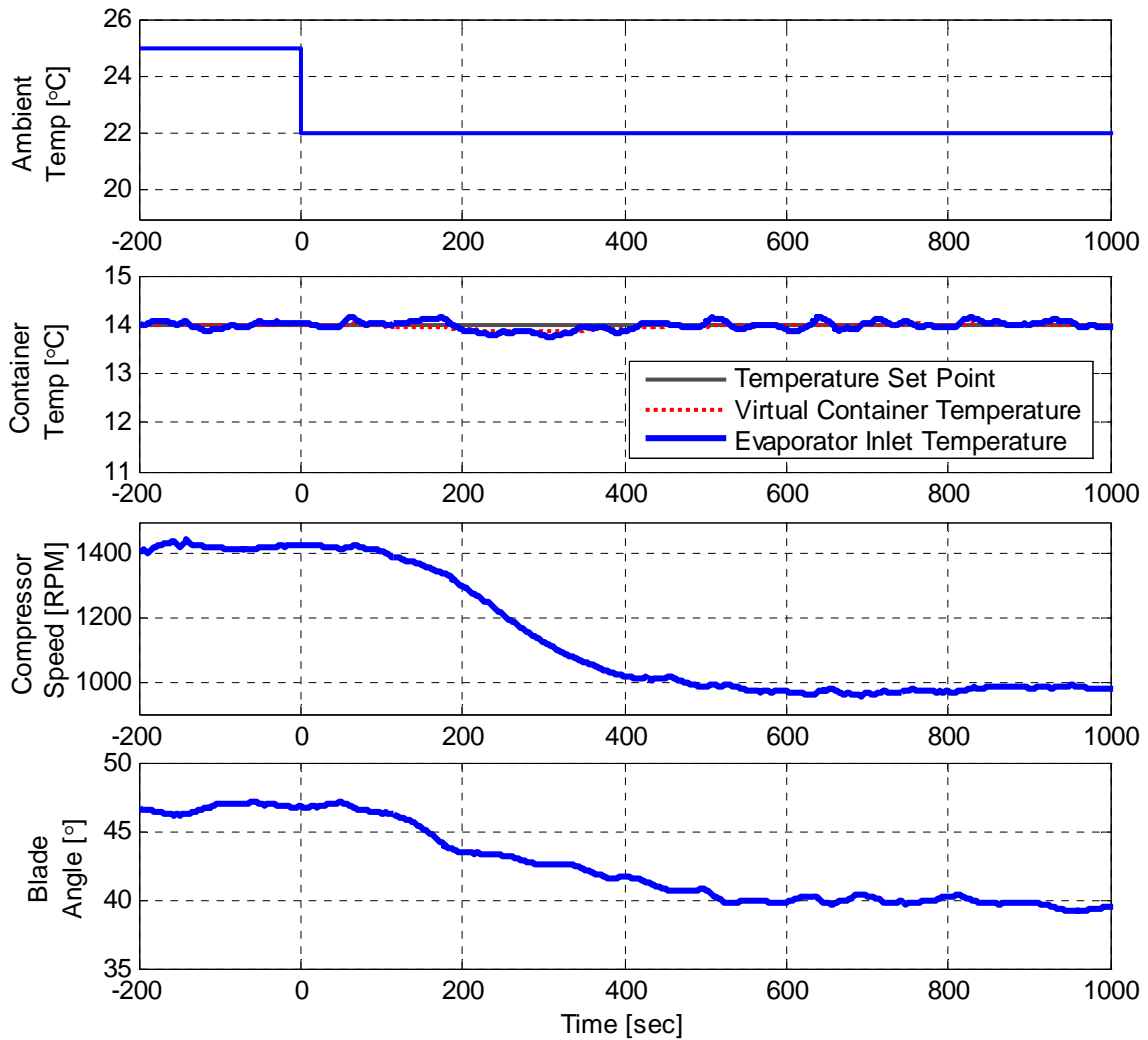
Figure 3.38   Change in ambient temperature during operation using hardware-in-the-loop load emulation

3.7   Summary

Hardware-in-the-loop load emulation has been shown to provide a flexible testing environment for air conditioning and refrigeration systems. This method provides an alternate solution to full scale testing in environmental test chambers which is both a costly and space consuming method of testing. Instead, an environmental load model accounts for the interactions between the AC&R unit, the container, and the surrounding environment. The accuracy of this model is paramount in subjecting the AC&R system to loading conditions representative of conditions it would experience while cooling the specific container in the actual environment. Hardware-in-the-loop load emulation provides a framework which may be used in the experimental evaluation of system and controller performance. This method of testing is used in this thesis to validate the developed controllers to realistic disturbances and cooling scenarios.
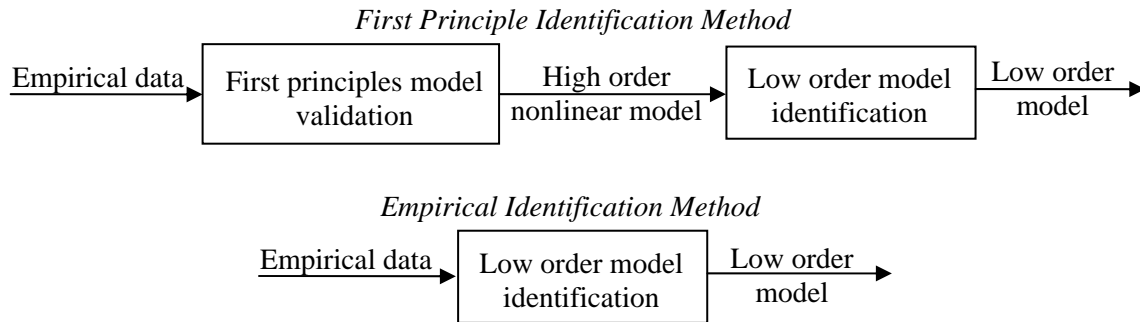
Chapter 4

Modeling

This chapter presents the development of a modeling environment to accurately simulate evaporator superheat dynamics for controller development and evaluation. The models in this chapter are empirically identified with various data-based parameter identification techniques. Evaporator superheat is explained in detail for better understanding of the empirical data used for model development. The identified models are used in subsequent chapters for controller design and simulation.

4.1 Past Modeling Efforts

Vapor compression cycle modeling has been the focus of much research due to the information these models provide to engineers in terms of system and component level understanding. There have been many modeling efforts in the literature that have been successful in accurately capturing the dynamics of the vapor compression cycle. One significant modeling effort has been the development of the modeling environment called Thermosys. This modeling framework is based on first principles and has been developed through modeling work that began within the Alleyne Research Group in 2000. This modeling environment is capable of simulating the complete vapor compression cycle and relies on a combination of smaller component level nonlinear models that are implemented in a MATLAB/SIMULINK environment [13].

Modeling packages such as Thermosys may be used to identify low order models for controller design. These modeling packages are also extremely useful in determining model trends and coupling effects for component and controller design. However, identifying models

from this type of framework is less frequently used for controller design when the intention is to experimentally implement the control framework. This is due to the indirect identification of the control-oriented model. The first principle modeling framework is first validated using empirical data. Then a low order model is fit to the high order nonlinear first principles model. This is a two step method used to identify a control-oriented model.

First Principle Identification Method

Empirical data → | First principles model validation | — High order nonlinear model → | Low order model identification | — Low order model →

Empirical Identification Method

Empirical data → | Low order model identification | — Low order model →

Figure 4.1   Model identification methods

On the other hand, the empirical identification method involves a single step of directly identifying the parameters of the low order model from empirical input/output data. Figure 4.1 shows the steps involved in identifying a low order model while using the first principles identification method and the empirical identification method. Identifying a low order model is most direct while using the empirical identification method. Yet, the first principle method provides a more complete dynamic modeling framework. Each method has a similar drawback where a functioning experimental system is needed to obtain data for model validation.

In this chapter the empirical identification method is used for model development since a low order model is desired for controller design, simulation, and experimental implementation. The empirical identification method used in this chapter is a gray box technique where the model order and form is assumed based on knowledge of the system. The empirical identification method is also referred to as the data-based identification method and is more commonly used for model development for controller design since a control-oriented model is identified directly from empirical data. Empirically identified models are commonly used for superheat control design in literature [14],[15].

4.2 Evaporator Superheat Sensing

Evaporator superheat is discussed in this section to allow the reader to better understand the origins of the empirical data used for model development. Evaporator superheat is defined as the temperature at which the vaporized refrigerant at the exit of the evaporator is elevated above its saturation temperature. Figure 4.2 illustrates the refrigerant as it flows through the evaporator. The refrigerant enters the evaporator from the expansion device in a two phase form. As the refrigerant flows across the evaporator the refrigerant absorbs heat from the cooled space and boils. Given adequate evaporator tube length and expansion device opening, the liquid refrigerant completely boils and the flow becomes 100% vaporized before exiting the evaporator.
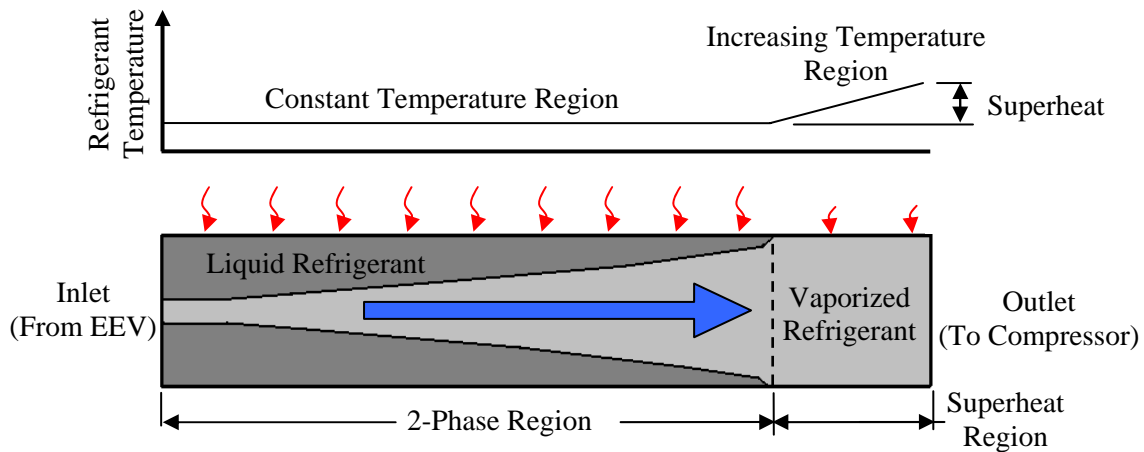
Figure 4.2   Evaporator superheat illustration

The two-phase region within the evaporator is at a constant temperature throughout since the heat absorbed boils the liquid refrigerant instead of heating it as illustrated in Figure 4.2. The refrigerant temperature begins to increase in the superheat region since the refrigerant is 100% vaporized and any heat absorbed increases the temperature of the vapor.

One method to measure evaporator superheat is to place one temperature sensor at the outlet of the evaporator and another temperature sensor at the inlet of the evaporator. The temperature sensor at the inlet of the evaporator is a measure of the saturation temperature. This measurement is subtracted from the outlet temperature measurement to determine the evaporator superheat. Another method to measure evaporator superheat is to place a pressure sensor and temperature sensor at the outlet of the evaporator. The saturation temperature of the refrigerant

is calculated from a look up table using the pressure measurement. The evaporator superheat is then calculated by subtracting the saturation temperature from the measured outlet temperature.
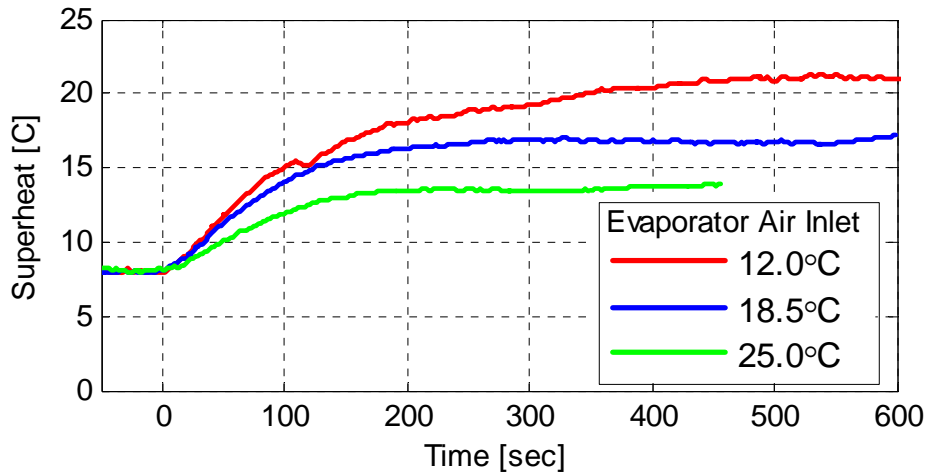
The temperature-temperature evaporator superheat sensing method is less accurate since there is a small pressure drop across the evaporator. This causes the inlet and outlet saturation temperatures to be slightly different. The pressure-temperature sensing method is more accurate since the saturation temperature is inferred with sensor data mounted on the outlet of the evaporator. However, the pressure-temperature method incurs a greater cost due to the relative large cost of pressure sensors. The pressure-temperature measurement is used for the results shown in this thesis.

4.3   Expansion Valve - Superheat Modeling

The main model required for tuning the EEV superheat control loop is the model between valve opening and superheat. Due to the inherent nonlinear dynamics of the refrigeration cycle, the model between valve opening and superheat is identified at different operating conditions. Specifically, the dynamics between valve opening and superheat may be influenced by many factors such as level of superheat, system charge, compressor speed, evaporator air inlet temperature, and other system variables. Some of these factors influence the dynamics more significantly than others depending on the application. For example, a model that accounts for varying ambient conditions may be useful for transport refrigeration applications. However, this type of model may be of less use for applications such as household refrigerators where the ambient conditions are usually constant.

The evaporator air inlet air temperature is a common parameter which influences the superheat dynamics and changes significantly during the operation of most AC&R systems. For cooling applications, the evaporator air inlet temperature is equivalent to the container temperature since the evaporator pulls air from the container. For heating applications, the opposite holds where the condenser inlet air temperature is equal to the container temperature. Here, the cooling application is considered. During system startup the container temperature is typically high; the AC&R system then cools the container to the desired temperature. If significant changes in the inlet air temperatures occur more advanced control methods may be implemented to account for the nonlinear dynamics.

Therefore, in this section a nonlinear model between valve opening and superheat is empirically identified at various evaporator inlet air temperatures. This model is said to be nonlinear since the parameters of the model depend on the inlet air temperature. Open loop data is collected from the experimental test stand at the University of Illinois by fixing the fan speeds, inlet air temperatures, and compressor speed while stepping the valve closed by 1%. A change in 1% of the overall valve stroke is equivalent to 5% to 10% of the full stroke used. The valve is stepped at three different evaporator air inlet conditions: 12°C, 18.5°C, and 25°C. Figure 4.3 shows experimental results from three different evaporator air inlet temperatures when the valve is stepped at 0 seconds. The upper red curve is the superheat response to a 1% change in valve opening at an evaporator air inlet temperature of 12°C. The blue curve and green curve are superheat responses to 1% change in valve opening at 18.5°C and 25°C air inlet temperature respectively. From this figure it is clear that the parameters of the model between valve opening and superheat are dependent upon the inlet air temperature.

Figure 4.3   **Superheat response to a step change in valve opening at different evaporator inlet air temperatures**

The model between valve opening and superheat has been identified as a first order plus time delay model numerous times in literature [14],[15],[16]. This model accurately captures the dynamics and is used in this work where the three model parameters are manually identification from the open loop step response data. The model transfer function is shown in Equation 4.1, with superheat T_S, valve opening U_V, gain M_V, time delay t_{dV}, and time constant τ_V. The negative sign in this transfer function is to account for the step decrease in valve opening during

the open loop data collection. The identified parameters are shown in Table 4.1. These models are used in following chapters in the development of superheat controllers.

$$\frac{T_S}{U_V} = \frac{-M_V \cdot e^{-t_{dV} s}}{\tau_V s + 1}$$

(4.1)

Table 4.1   Valve to superheat model parameters at various inlet air temperatures

	Evaporator Inlet Air Temperature		
	25.0°C	18.5°C	12.0°C
Time constant (sec)	93	94	125
Amplitude (°C)	5	7.8	10.9
Delay Time (sec)	13	10	3

Similarly, the model between valve opening and superheat is identified at different levels of superheat for controller design purposes. Figure 4.4 shows the superheat response to a 1% valve decrease during two different initial superheat levels. The red dashed curve has an initial superheat of 9°C whereas the green curve has an initial superheat of 18°C. Table 4.2 shows the model parameters at high and low superheat levels.
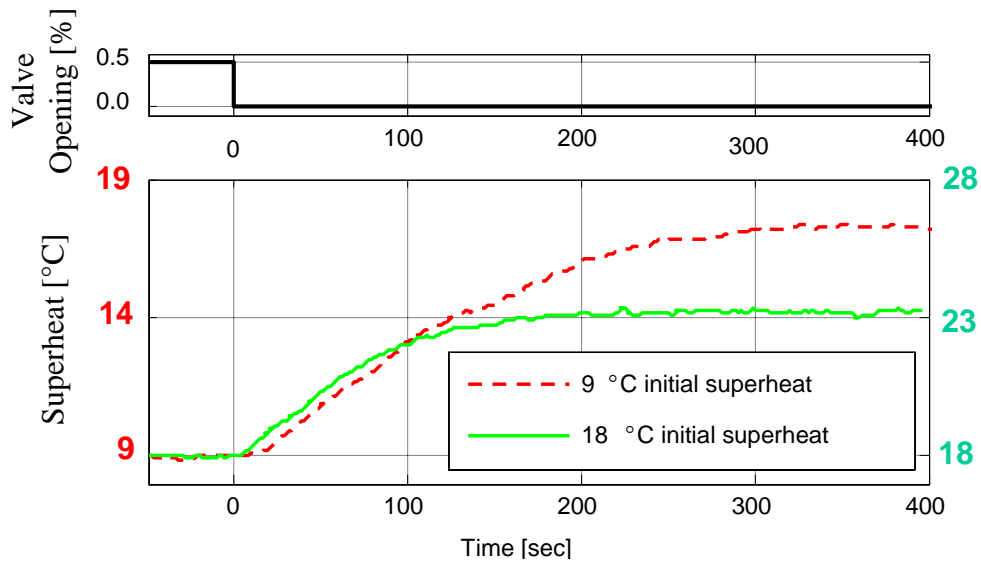
Figure 4.4   Superheat response to a step in valve opening at different initial superheat levels

At high superheat levels the model between valve opening and superheat has a relative small time delay, a small gain, and a small time constant. At a low superheat levels the model has a relative large time delay, a large gain, and a large time constant. The large change in the time delay between low and high superheat levels is from a larger mass transfer delay with the lower superheat case. The low superheat case has a smaller superheat length, and therefore a larger mass of refrigerant occupies the evaporator which causes increased time delay. This time delay plays a significant role in the stability of the closed loop superheat control loop and the implications are discussed in Chapter 5.

Table 4.2   Model parameters at low and high superheat

	Initial superheat level	
	9°	18°C
Time constant (sec)	120	85
Amplitude (°C)	16	10
Delay Time (sec)	14	3

There is a discrepancy in the identified amplitudes between the models shown in Table 4.1 and Table 4.2. This is most notably due to a difference in system charge during data collection. The experimental air conditioning and refrigeration test stand in the Mechanical Engineering Lab at the University of Illinois has been observed to have varying dynamics depending on the system charge. Since this system is a research test stand it has an array of different possible operating configurations. While the system is reconfigured to isolate/include components, refrigerant may unknowingly be isolated in certain components, piping, or within other segments of the system. For example, when a researcher wishes to test the system with the receiver and accumulator isolated, the valves to these components are closed. The amount of refrigerant in these components at the time the valves are closed dictates how much refrigerant will be available for the main VCC loop. The amount of refrigerant located within components during reconfiguration depends on the state of the system (i.e. temperature, pressure, system shutdown procedure, humidity, etc.) and is not completely controllable. Therefore, the charge within the main VCC is not completely controllable when the system is reconfigured. The

charge of experimental system at the University of Illinois fluctuates frequently since many different researches configure the system on a regular basis.

Efforts have been put forth to consistently configure the system in hopes of ensuring that the charge in the main VCC loop will be repeatable in case another researcher uses the system. A typical method that has been adopted for the results shown in this thesis has been the 'wait and configure' method. With this method, the system is first turned off with each valve open, 12 hours is allowed to pass, and the system is configured in the desired arrangement. This method is preferred since the pressures and temperature of the refrigerant within each component is given adequate time to equilibrated; 12 hours is specified here since the system is usually allowed to rest overnight. There are still slight dependencies such as shut down procedure which may isolate liquid refrigerant in certain areas of the system. Using a method such as this does not guarantee that the charge will be identical to the last time the system was configured in this arrangement, but does improve repeatability.

Another method that may be used to maintain a consistent system charge is to configure the system in the desired arrangement. Proceed to drain the charge from the circuit and the fill the circuit with precisely the amount of charge that is needed. This method is not used here since this process requires special hardware to allow the system to be drained and recharged safely.

Since the system charge plays an important role in the dynamic behavior of the cycle, the method the system is reconfiguration becomes important issue at times. Most importantly, when models are identified at early stages and controller are tested after the system has undergone reconfiguration. It has been observed on the experimental system that a change in the system charge does not affect the form of the model but rather the model parameters. The refrigerant charge of commercial AC&R system remains relatively constant during operation and therefore this is typically not an issue during the development of models and controllers.

4.4   Compressor Speed - Superheat Modeling

The model between compressor speed and superheat is identified to allow compressor speed disturbances to be incorporated in the simulation environment. A nonlinear model is identified for the development of a nonlinear system-wide controller for superheat regulation. Strong coupling exists between compressor speed and superheat which reduces the superheat

tracking performance during compressor speed fluctuations. Due to the nonlinear dynamics, a model between compressor speed and superheat is identified at different initial compressor speeds.

As with the valve opening to superheat model, the compressor speed to superheat model is identified with empirical step response data. The open loop data used for model identification is obtained by running the system with fixed fan speeds, inlet air temperatures, and valve opening while increasing the compressor speed by 100 RPM. The superheat is first regulated to 8°C by adjusting the valve opening. The valve opening is fixed and the compressor speed is stepped. This is done at different initial compressor speeds to develop a nonlinear model where the model parameters depend on the initial compressor speed; the open loop superheat response is shown in Figure 4.5.
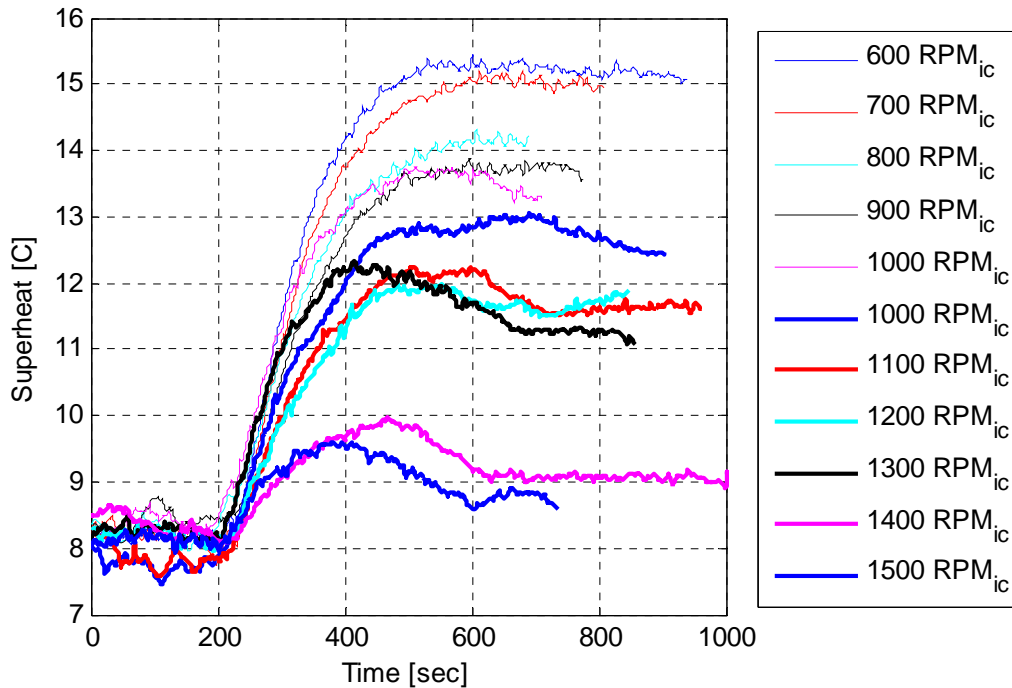
Figure 4.5   **Superheat response to a 100 RPM increase in compressor speed at a range of initial compressor speeds**

Figure 4.5 clearly illustrates the nonlinear behavior of the vapor compression cycle. The superheat response to a change in compressor speed is considered to be a first order response. A majority of the response trajectories shown in Figure 4.5 exhibit that of a first order response. There does exist, at larger initial compressor speeds, some overshoot which indicates a second

order model. The amount of overshoot is not considerable and a first order model is fit to each response to maintain simplicity for control design efforts. This assumption does not significantly affect the model accuracy as will be shown during model validation. Therefore, the model form is taken to be first order independent of the compressor speed, ω. There is a large difference in the coupling between compressor speed and superheat at different initial compressor speeds. The compressor to superheat model form is the same as that of the model between valve opening and superheat and is shown in Equation 4.2. Where ω is compressor speed, T_S is superheat, M_ω is the model amplitude, τ_ω is the time constant, and where $t_{d\omega}$ is the time delay.

$$\frac{T_S}{\omega} = \frac{-M_\omega \cdot e^{-t_{d\omega}s}}{\tau_\omega s + 1}$$

(4.2)

Table 4.3 shows the model parameters for the range of compressor speeds tested in Figure 4.5. There are no significant trends observed in the time constant or time delay of the model. The time constant is on the order of 100 seconds and the time delay on the order of 25 seconds. Therefore, these parameters are identified nominally and used for the entire range of compressor speeds. The time constant of this model is taken to be 95 seconds, whereas the time delay is taken to be 25 seconds.

Table 4.3   Compressor speed – superheat model parameters

| Initial Compressor Speed [RPM]	Time Constant [sec]	Time Delay [sec]	Amplitude [°C/RPM]
600	94	20	0.072
700	105	25	0.070
800	107	24	0.062
900	104	31	0.058
1000	77	12	0.053
1100	92	18	0.037
1200	98	23	0.038
1300	62	8	0.033
1400	38	25	0.011
1500	32	8	0.008

On the other hand, the magnitude, M_ω, of the model is strongly dependent on initial compressor speed. The magnitude of the model is determined from the data presented in Figure 4.5 by dividing the magnitude change in superheat by the magnitude change in compressor speed for each response. Figure 4.6 shows the correlation between the magnitude M_ω and compressor speed. Aprea et al. also investigated the correlation between evaporator gain and compressor speed and found a similar relation [16]. This correlation is due to a smaller nominal mass flow rate at low compressor speeds, an equivalent change in compressor speed results in a large relative change in mass flow rate, and thus a larger change in superheat during smaller initial compressor speeds [13].

The plotted line is labeled $y = -.00007x + 0.1211$
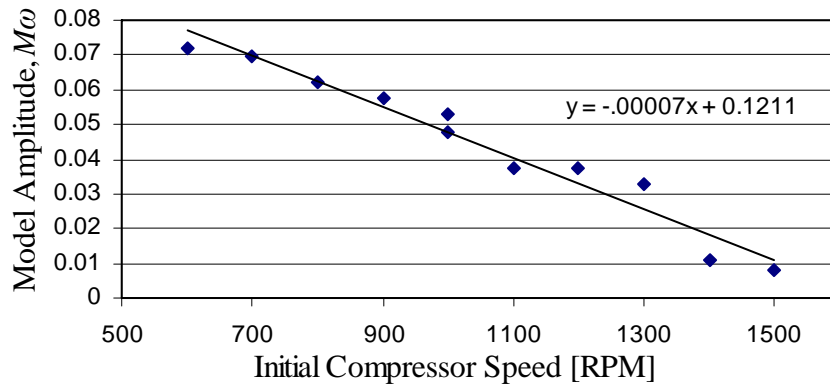
Figure 4.6   Correlation between initial compressor speed and magnitude M_ω

Thus far, the compressor speed to superheat model has been identified using empirical data from compressor speed step increases. Different dynamics are expected during a compressor speed decrease due a difference in the required torque to change shaft speed. Figure 4.7 shows experimental superheat response data during a compressor speed increase and decrease. In this result the compressor speed is changed by 100 RPM at 0 seconds. One trajectory is the superheat response to a compressor speed increase and the other response is to a compressor speed decrease. The time constant and gain of the models are similar while the time delay is strongly dependent on the direction of compressor speed change. During a compressor speed increase there is a large time delay between the compressor speed increase command and the superheat response. One contributing factor may be from a lag between desired compressor speed and the actual compressor speed. For example: when the compressor speed increases the

power supplied to the motor increases (the input power is limited) and the compressor shaft increases in kinetic energy and speeds up. This occurs with some lag due to the limit of how much power is available to the electric motor. On the other hand, during a compressor speed decrease the power to the motor is decreased and the compressor shaft looses kinetic energy and slows down, which occurs quickly. Therefore one potential reason for the difference in delay time may be from the compressor taking slightly more time to increase shaft speed than it takes to decrease the shaft speed.
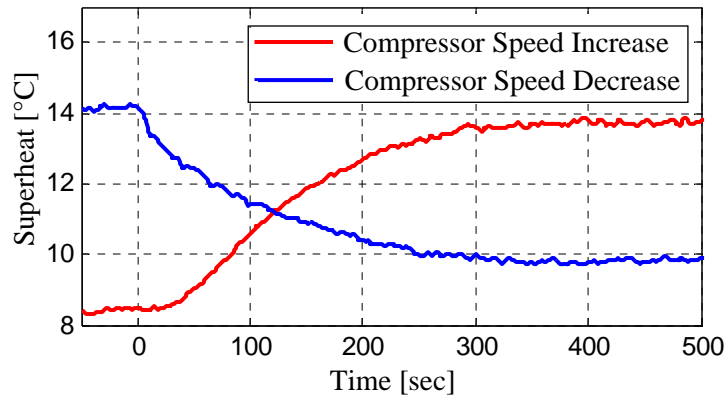
Figure 4.7   Superheat response to compressor speed increase and decrease

The magnitude M_ω for increasing and decreasing compressor speeds are equal and can be easily understood with this example: if the system is initially at steady state and the compressor is increased by 100 RPM, the superheat will converge to a larger value. If the compressor is then decreased by 100 RPM, back to its original speed, the superheat will then converge back to its original value. Therefore, the magnitude M_ω of the model for compressor speed increase must equal that of the model amplitude for compressor speed decrease.

A first order model is used to model a compressor speed decrease while a first order plus time delay model is used to model compressor speed increases. The difference between the compressor speed increase and decrease becomes important in the development of the feedforward control framework shown in Chapter 5. Equation 4.3 shows the model for superheat response to a decreasing compressor speed and Equation 4.4 shows the model for superheat response to an increase in compressor speed.

69

$$\frac{T_S}{\omega_\downarrow} = \frac{M_\omega}{95s+1} \qquad\qquad (4.3)$$

$$\frac{T_S}{\omega_\uparrow} = \frac{M_\omega \cdot e^{-25s}}{95s+1} \qquad\qquad (4.4)$$

4.5　Model Validation

  This section validates the models identified in Section 4.3 and Section 4.4. A simulation environment is developed using the model parameters that have been empirically identified. Open loop data is collected from the experimental system by supplying the actuators of the system with a pseudorandom binary sequence. The models are individually identified by actuating the electronic expansion valve and compressor speed independent from one another. First, the valve opening to superheat model is validated for two different operating conditions: 25°C evaporator inlet air temperature and 15°C evaporator inlet air temperature. This model is validated at two conditions to ensure the accuracy of the empirical nonlinear model identified in Section 4.3. Figure 4.8 shows open loop experimental data where the valve is supplied a pseudorandom binary signal and the superheat is observed while the evaporator inlet air temperature is maintained at 25°C. During this experiment the compressor speed is fixed at 1600 RPM. The model output closely matches the experimental data. Figure 4.9 shows a similar scenario where the model is validated at an evaporator inlet air temperature of 15°C. The compressor speed is maintained at 1600 RPM while the inlet air temperature is controlled to 15°C using the emulation unit. In this case the emulation unit is used only to maintain the evaporator inlet air temperature and there is no virtual container. The model in Figure 4.9 closely matches the experimental data. These results indicate that the model form and the identified parameters of the model between valve opening and superheat is capable of accurately predicting evaporator superheat.
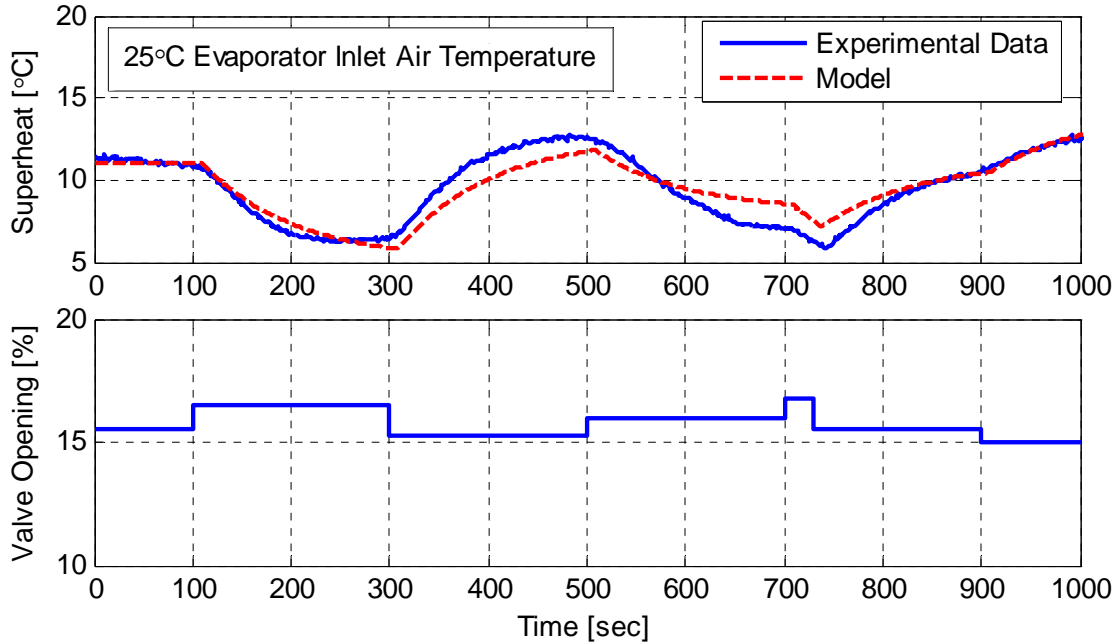
Figure 4.8   **Valve opening – superheat model validation at 25°C evaporator inlet air temperature**
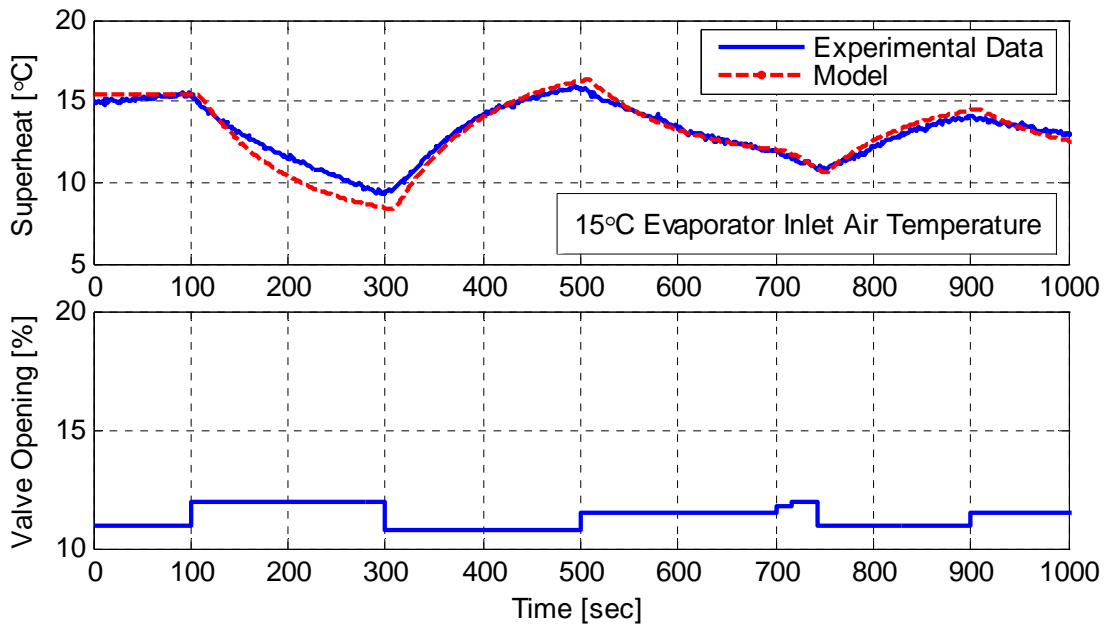

Figure 4.9   **Valve opening – superheat model validation at 15°C evaporator inlet air temperature**

Second, the compressor speed to superheat model is validated. This model is validated for two different nominal compressor speeds: 1450 RPM and 750 RPM. This is done to ensure the accuracy of the empirical nonlinear model developed in Section 4.4. Figure 4.10 shows open loop experimental data where the compressor speed is supplied a pseudorandom binary signal with a nominal compressor speed of 1450 RPM and the superheat response is observed. During the open loop test the valve opening is fixed to allow the superheat to begin at 8°C while the evaporator inlet air temperature is maintained at 25°C. As shown in the lower figure in Figure 4.10 the model output closely matches the experimental data. Figure 4.11 shows a similar scenario where the compressor speed fluctuates around a nominal level of 750 RPM. Likewise, the model matches closely with the experimental data. There exists some discrepancy in the gain of this model which may have originated from a change in system charge that occurred between the time of identification and the time of validation. Overall, each model matches well with the experimental data which is important for controller design as shown in Chapter 5.
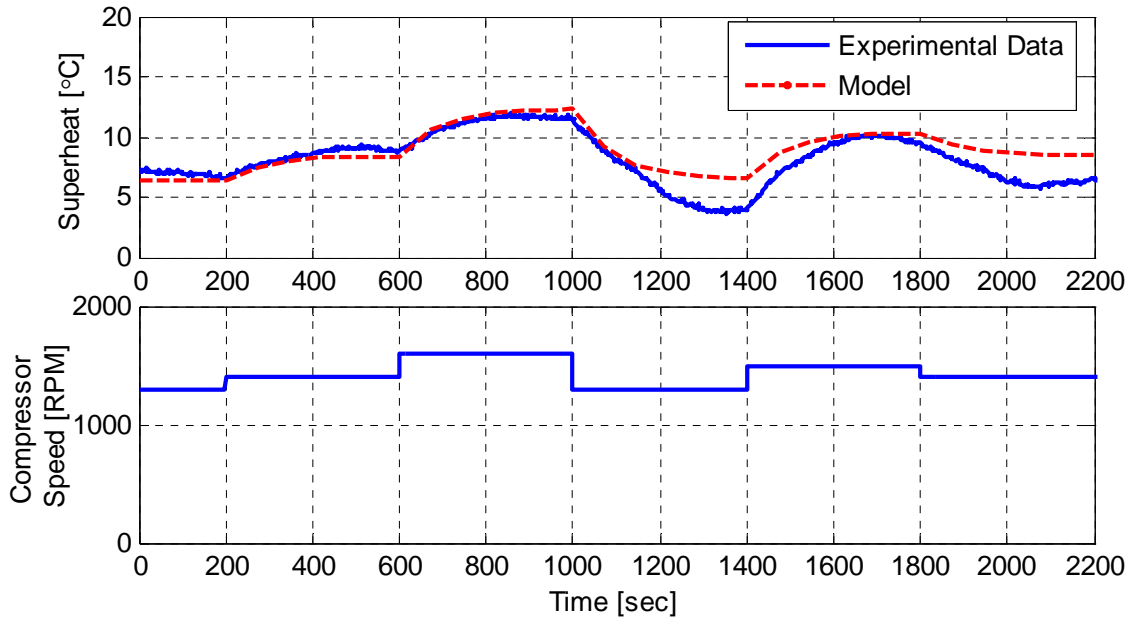
Figure 4.10   Compressor speed – superheat model validation at high compressor speed
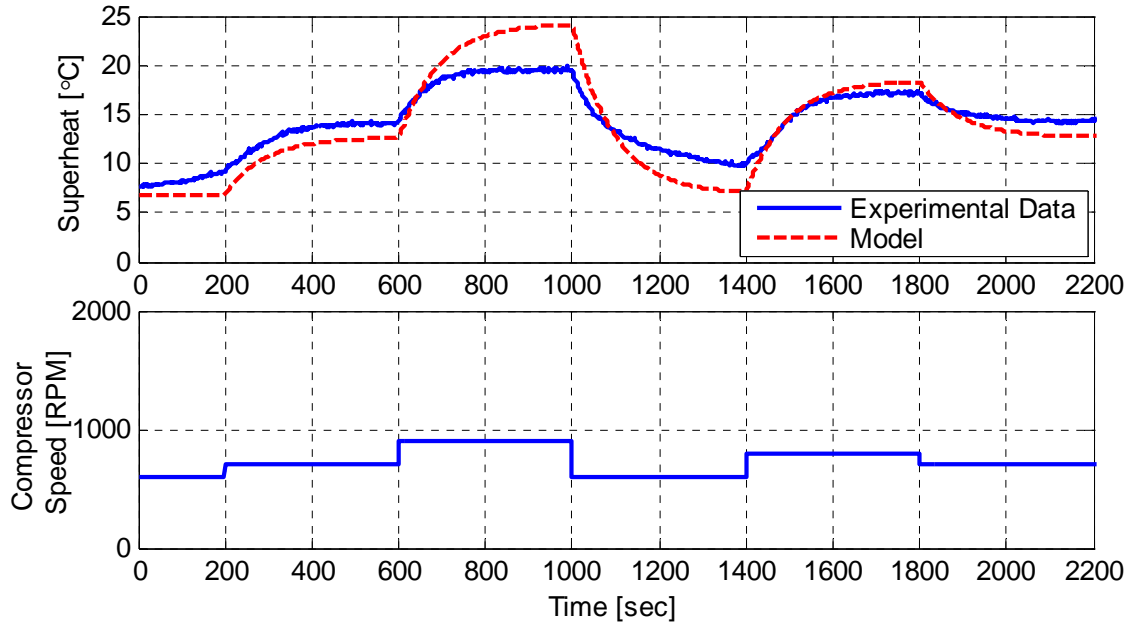
Figure 4.11   Compressor speed – superheat model validation at low compressor speed

4.6   Discussion

This chapter demonstrates the development of dynamic models for the vapor compression cycle which are suitable for controller design. Low order control-oriented models have been developed through system identification techniques. This chapter also investigates the nonlinear dynamics of the vapor compression cycle. These models are validated with experimental data and have been shown to accurately predict evaporator superheat. Overall, this chapter provides a method to identify nonlinear control-oriented models. Moreover, the information presented in this chapter allows a control engineer to better understand the nonlinear dynamics of the vapor compression cycle. A nonlinear understanding of the vapor compression cycle is extremely important since these models are extensively used for controller design. Chapter 5 uses these models and nonlinear relations as a means to understand design considerations which will allow for precise superheat regulation.

Chapter 5

Superheat Control Design

This chapter presents an overview of the various control frameworks that have been developed through this research to enhance evaporator superheat regulation. First this chapter begins with a discussion of commercially available expansion devices for superheat regulation in Section 5.1. Section 5.2 discusses guidelines for superheat regulation. Section 5.3 presents a literature review which summarizes the state of the art control efforts for superheat controller development for electronic expansion valves. The standard proportional-integral-derivative control configuration is investigated in Section 5.4. This section presents the limitation of the PID controller and presents a controller development flow chart to guide the reader throughout the chapter. Section 5.5 presents a scheduled feedforward control framework which may supplement the PID controller to improve disturbance rejection. Section 5.6 details the design of a gain scheduled feedback controller where the system-wide performance is maintained. A multiple feedback control configuration is presented in Section 5.7 which is designed to circumvent the typical performance vs. robustness tradeoff. The control features discussed in this chapter have been developed to provide a modular framework to improve disturbance rejection, system wide stability, and steady state tracking for an array of AC&R applications.

## 5.1 Superheat Control Devices

This section discusses the benefits and limitations of the common expansion devices used to regulate superheat in AC&R systems. One common expansion device for superheat regulation is the capillary tube. The capillary tube is a long tube with a small diameter where the length and diameter of the tube is designed to meet the systems mass flow rate requirement and therefore

regulate superheat to the desired level. The capillary tube has no feedback mechanism which is the reason this device is not used in certain applications. Superheat is usually regulated to a relative large level during normal operation so that any disturbances do not risk component damage. This device is widely used in many of the systems being produced today due to the low cost and simple design.


Figure 5.1   Capillary tube expansion device

Another common expansion device is the thermostatic expansion valve which modulates the valve opening through a mechanical feedback path. This device uses pressure feedback from a sealed bulb that is attached to the outlet of the evaporator. The bulb is filled with a gas which expands and contracts when the evaporator outlet refrigerant temperature changes. This change is assumed to be proportional to the evaporator superheat. As the bulb pressure fluctuates, the position and opening of a throttling valve is affected through the compression/decompression of a coil spring. This type of expansion device has improved superheat regulation relative to the capillary tube due to the feedback mechanism. The compression of the coil spring is physically tuned via a screw on the outside of the thermostatic expansion valve. If the operating conditions change the superheat is not guaranteed to remain at the same steady state level. This valve is also known to exhibit superheat hunting during certain operating conditions which reduces the ability of the valve to effectively regulate superheat [17].
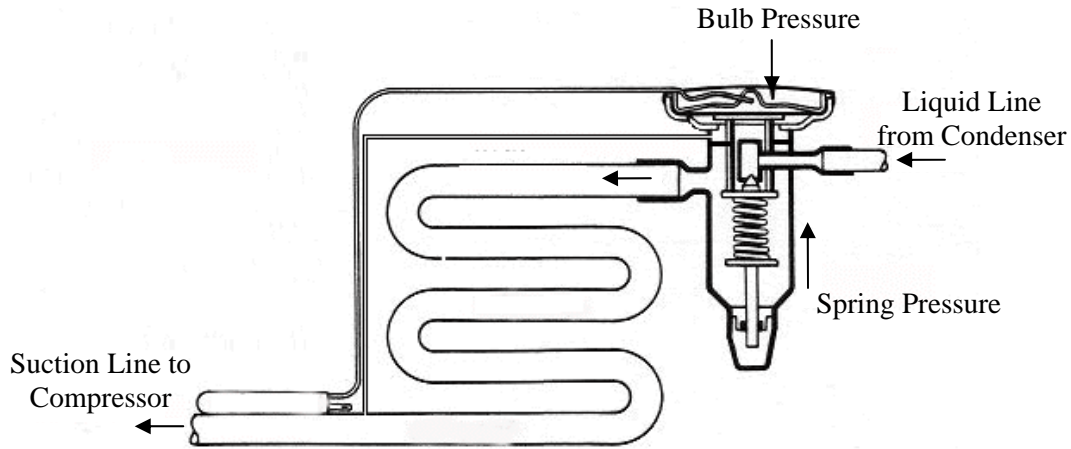
**Figure 5.2   Thermostatic expansion device**

An emerging expansion device is the electronic expansion valve (EEV) which modulates the valve opening electronically. This type of valve is gradually becoming implemented in many AC&R applications as more is understood about the type of control framework which is necessary to regulate superheat effectively. The opening of this valve is modulated electronically by a stepper motor which provides precise control of the needle position and therefore accurate control of the refrigerant mass flow rate. The EEV is coupled to a stepper motor control board which takes in a signal from the superheat control algorithm. The superheat control algorithm is one critical component in the system which allows for high performance regulation. This research investigates control configurations which improve superheat regulation with the EEV to ultimately allow the designer to specify a low superheat set point for high efficient operation.
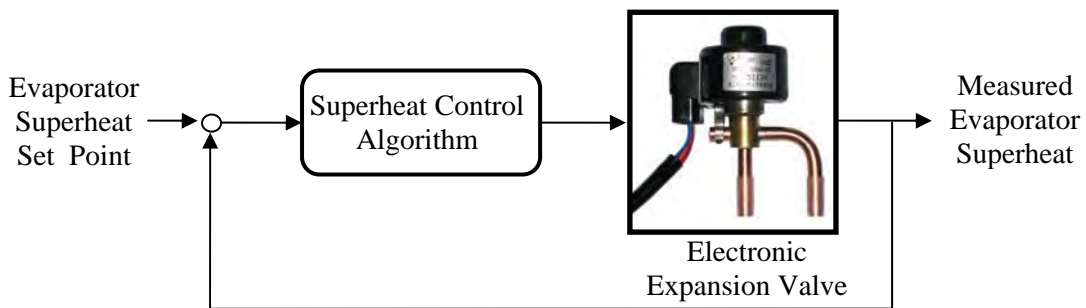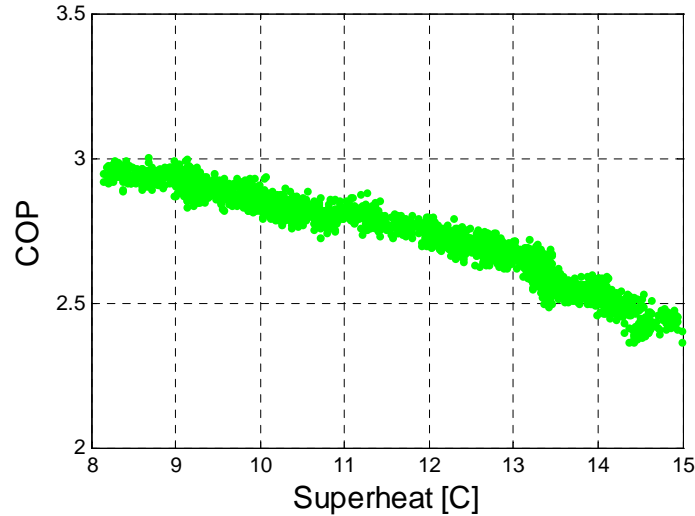

Figure 5.3   Electronic expansion valve

5.2   Superheat Regulation

Evaporator superheat regulation addresses the tradeoff between efficiency and component safety which is inherent to all vapor compression systems. In practice, the superheat set point is set as low as possible while accounting for the anticipated superheat deviation during a system disturbance. Figure 5.4 illustrates the tradeoff between efficiency and component damage where a low superheat setting allows for high efficiency operation at the cost of a greater risk to component damage, specifically the compressor as discussed in Chapter 4. A high superheat setting reduces the risk to component damage while reducing the efficiency of the system. The tradeoff curve shown in Figure 5.4 is not necessary linear, this figure simply illustrates the general tradeoff that must be considered while specifying a superheat set point. A superheat control loop that is designed to have high performance to disturbances will reduce the risk to component damage and allow for a low superheat set point.
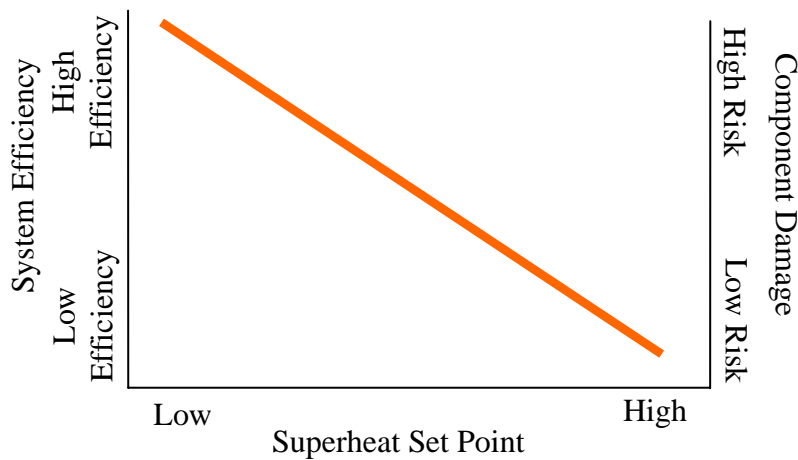
Figure 5.4   Superheat setting tradeoff

Figure 5.5 shows experimental data obtained from the experimental test system at the University of Illinois where the inverse relation between the coefficient of performance and the level of superheat is observed. The coefficient of performance (COP) is a measure of the efficiency of the system where a larger COP indicates more efficient operation; see Equation 5.1 [18]. This figure experimentally shows that as superheat is decreased the system efficiency increases similar to Figure 5.4. Therefore a high performance superheat control loop is desired to allow for the lowest feasible superheat set point.

Figure 5.5   Superheat influence on coefficient of performance

$$COP = \frac{Cooling\ effect}{Work\ input} = \frac{\dot{m}(h_1 - h_4)}{\dot{W}_{Net,in}}$$ (5.1)

5.3   Electronic Expansion Valve Literature Review

Evaporator superheat was first controlled with an electronic expansion valve in the early 1970s using a proportional control structure [19]. A PI and PID control procedure was later patented in the mid 1980's [20],[21]. These first studies did not account for the nonlinear dynamics of the vapor compression cycle.

In the mid to late 1990s research efforts further developed the PID controller to more effectively regulate superheat over a wider range of operating conditions and disturbances. In 1994 Parkum and Wagner [22] developed a gain scheduled feedback PI controller in which the feedback gains were scheduled depending on the level of superheat. This control structure also considered a feedforward control element which accounted for room temperature disturbances. This investigation showed the need for nonlinear feedback control while also showing an application for feedforward control. In 1997 Chia et al. [14] developed a fuzzy logic control for superheat regulation and compared its performance to a PID controller. The fuzzy logic controller was observed to be slightly more robust than the PID controller while cooling a shipping container. However, tuning the fuzzy logic controller requires in depth knowledge of the system dynamics and rigorous tuning. In 2000 Jolly et al. [23] built upon the fuzzy logic

controller by designing the control loop to adjust the desired superheat set point on-line with a second fuzzy logic control loop. This outer loop control was developed to find the minimum stable superheat during operation to ensure the most efficient superheat set point.

In 2000, Finn and Doyle [15] conducted a general investigation of evaporator superheat control via a PID controller. This study investigated PID tuning methods and the effect which these methods have on superheat regulation. It was concluded that large control gains decrease stability but increased response time. This study also investigated the nonlinear dynamics related to the container temperature which was used as the scheduling variable in a gain scheduled feedback controller. This investigation concluded that controller stability may be accomplished through either conservative tuning or periodic retuning such as a gain scheduled method.

In 2004, Li et al. [24] developed a fuzzy PID controller where the controller gains are determined through fuzzy reasoning. This study focused on the development of a control algorithm to reduce superheat deviations during a compressor speed fluctuation. The fuzzy logic controller improved superheat regulation relative to a PID controller at the cost of time intensive tuning of the fuzzy logic framework. Lin and Yeh [25] investigated a MIMO control framework where the container temperature and superheat were inputs to a MIMO controller with compressor speed and valve opening as outputs. This study showed improved performance over a SISO configuration since the system coupling was accounted for through the MIMO controller. This approach requires an accurate system model for the tuning of the MIMO controller. Moreover, a simple SISO configuration is desirable in industry for ease of tuning and implementation. The controllers developed in this chapter perform a task similar to the MIMO control however using a simple SISO structure with an additional control element to account for the coupling.

In 2008 Changenet et al. [5] developed a predictive functional control configuration for superheat regulation and compared the results to that of a PID controller during compressor speed fluctuations. This study found that the predictive functional control loop was able to regulate superheat more precisely than the PID controller. The predictive functional controller again requires complete understanding of the system dynamics and is not desirable for applications in industry due to the complexity of tuning and implementation.

79

Hua et al. [3] presented results which demonstrate the need for feedforward control of superheat while regulating the capacity of the system with compressor speed. During a change in temperature set point or a change in system load, the compressor rapidly changes speeds to meet the cooling demand. Due to the strong coupling between compressor speed and superheat the authors proposed a feedforward compensator to mitigate the coupling. This study showed that the feedforward controller improved the regulation of superheat. However, this study does not account for the nonlinear dynamics of the refrigeration system.

In 2010 Elliott et al. [26] developed a control configuration which accounts for the nonlinear dynamics of the refrigeration system. This study linearizes the valve opening to superheat response using a nonlinear gain which is identified based on the expansion valve in use. A cascade control loop is used to control evaporator superheat via a slow temperature feedback loop and a fast pressure feedback loop. This investigation implements this control framework on a hybrid expansion valve which is unique to the work of Elliott et al. [26].

Table 5.1   **Literature survey**

| Journal Articles	Papers	Patents
Fuzzy Control	4, [14],[27],[24],[23]	1, [41]
Nonlinear Control	5, [15],[23],[26],[25],[28]	4, [33],[34],[35],[36]
Feedforward Control	2, [3],[22]	3, [37],[38],[40]
PID	2, [29],[30]	3, [32],[39],[42]
MIMO	3, [31],[3],[25]	0
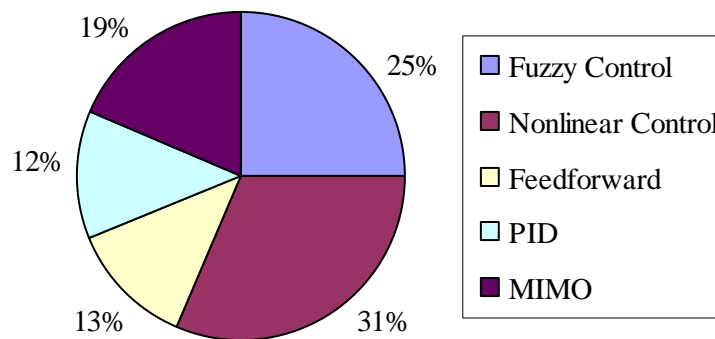
Figure 5.6   **Superheat control articles**
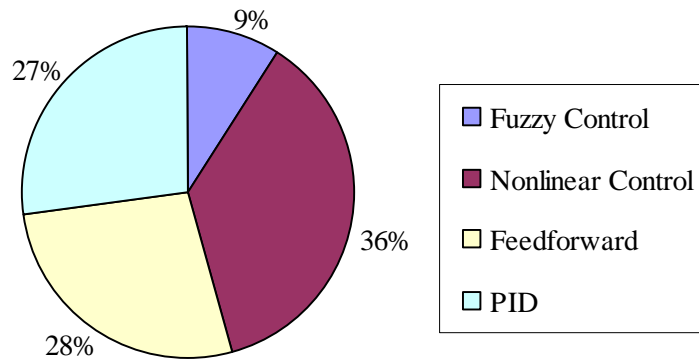
Figure 5.7   Superheat control patents

The superheat control loop has been studied for decades and many different approaches have been taken in the design of the feedback path. Table 5.1 summarizes the literature findings on electronic expansion valve control of superheat. Figure 5.6 and Figure 5.7 visually show the notable EEV control investigations found in academic papers and patents respectively. These figures report only selected papers and patents which are relevant to the research presented in this thesis. Some of the most successful superheat control investigations have used methods which account for the nonlinear dynamics while also improving regulation through disturbance rejection through the use of a feedforward control framework. The vapor compression cycle is known to be highly nonlinear which requires some type of nonlinear, such as a gain scheduled feedback method. Another method that has been investigated extensively has been the fuzzy logic controller. This is a nonlinear control technique which provides similar performance as the gain scheduled feedback control method. However, the fuzzy logic controller requires the design engineer to perform rigorous tuning based on the dynamics of the system. Therefore fuzzy logic is not pursued here. The scheduled feedback and feedforward control methods have been identified as the state of the art control methodologies for superheat regulation. These two proven control configurations are used as a benchmark for further controller development shown in the following sections.

## 5.4   PID Control of Superheat

This section discusses the regulation of evaporator superheat with a proportional-integral-derivative (PID) controller. This controller is commonly used in industry for superheat

regulation due to the ease of implementation and satisfactory performance. This type of control configuration has three gains in the feedback path: a proportional gain, an integral gain, and a derivative gain. The gains of the PID controller are tuned to provide the desired performance and robustness. Figure 5.8 shows the PID control configuration for superheat regulation.
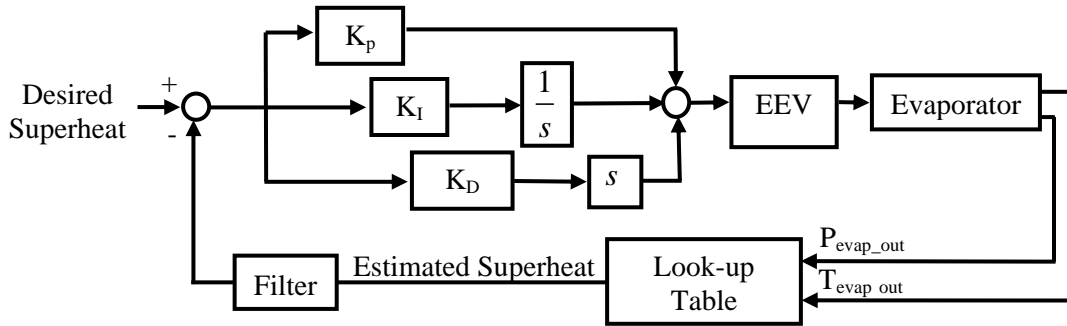
Figure 5.8   PID structure for superheat regulation

There exists an inherent tradeoff between performance and robustness that a control engineer must consider while tuning a PID controller. Tuning may be performed to provide high performance in terms of disturbance rejection and reference tracking, or the PID controller may be tuned to be robust to plant uncertainty and system noise. Figure 5.9 illustrates the tradeoff between performance and robustness which is present when tuning a PID controller. Typically a controller with large gains provides a high performance at the cost of large sensitivity to system noise and plant uncertainty [43]. A controller with smaller gains provides improved robustness to plant uncertainty and system noise at the cost of a reduction in performance in terms of disturbance rejection and reference tracking. Therefore, the design engineer must understand the plant dynamics and the control objectives.
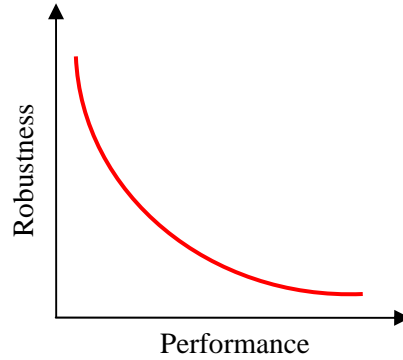
Figure 5.9   Robustness vs. performance tradeoff in feedback Systems

Depending on the sizing of the valve, an anti-windup strategy may be required to avoid actuator saturation during control. If the valve surpasses its saturation limit and there is no anti-wind up strategy in place, undesirable performance is observed as the controller may outputs a control effort which is not achievable by the actuator. The anti-windup scheme monitors the control effort to determine if the saturation limits have been reached. If the limits have been reached the control output is constrained within the saturation limits by influencing the integral action of the PID controller. The experimental test stand at the University of Illinois does not require an anti-wind up strategy since the electronic expansion valve does not approach its saturation limits during operation due to the small size of the valve as discussed in Chapter 2. However, many systems require an anti-windup strategy since the actuator may operate close to its saturation limit during operation.

The controllers developed in this research are primarily examined while regulating superheat to 8°C. This set point has been used as a standard for testing controllers while considering the potential AC&R applications. In transport refrigeration evaporator superheat is typically maintained between 3°C and 5°C. For residential applications superheat is commonly regulated to a level between 8°C and 10°C. In this research a superheat level of 8°C is used to allow the developed controllers to be implemented on an array of applications. The controllers developed in this chapter may be implemented to improve superheat regulation regardless of the superheat set point.

The next portion of this section discusses methods that may be used to tune a PID controller. Tuning methods such as pole-placement, tuning rules, frequency design, or heuristic tuning may be used to tune the PID controller. In this section tuning rules are used to design the

PID controller gains since they provide a simple and effective way to tune a PID controller given a model of the process. The two tuning methods that are investigated here are the Ziegler-Nichols and SIMC methods [43],[44]. The Ziegler-Nichols tuning method was developed in the 1950s, whereas the SIMC method was developed in 2001. The Ziegler-Nichols method typically provides large controller gains which enhance performance while increasing sensitivity to noise and plant uncertainty. On the other hand, the SIMC tuning method provides smaller controller gains which are less sensitive to system noise and plant uncertainly while providing a lesser degree of performance.

Using the models that have been identified in Chapter 4 the Ziegler-Nichols method is first used to tune a PID controller for superheat regulation at 16°C superheat with an evaporator inlet air temperature of 25°C. A high superheat set point of 16°C is used here to present the differences between high superheat regulation and low superheat regulation. The plant model identified in Chapter 4 is shown in Equation 5.2 and Equation 5.3.

$$\frac{T_S}{U_V} = \frac{-M_V \cdot e^{-t_{dV}s}}{\tau_V s + 1}$$ (5.2)

$$t_{dV} = 3, M_V = -10, \tau_V = 85$$ (5.3)

$$R = \frac{M_V}{\tau_V} = -0.117, \quad L = t_{dV} = 3$$ (5.4)

$$k_p = \frac{1.2}{RL} = -3.40, \quad k_I = \frac{k_P}{2L} = -0.56, \quad k_D = .5k_PL = -5.1$$ (5.5)

The SIMC tuning method is used to tune the PID controller as shown in Equation 5.6 and Equation 5.7. Since the plant model identified in Chapter 4 is a first order plus time delay model, the SIMC tuning rules provide a derivative gain of zero [44].

$$K_c = \frac{.5 * \tau_V}{M_V * t_{dV}} = -2.28$$ (5.6)

$$K_p = K_c = -1.42, \quad K_I = K_c / \tau_V = -0.016, \quad K_D = 0.0$$ (5.7)

The Ziegler-Nichols tuning method provides gains which are much larger than the gains provided from the SIMC tuning method as seen in Equation 5.5 and Equation 5.7. Therefore, it

is expected that the Ziegler-Nichols tuned controller will exhibit fast reference tracking and improved disturbance rejection whereas the SIMC tuned controller will be more robust to system noise and plant uncertainty.

The following results show the Ziegler-Nichols and SIMC tuned PID controllers regulating superheat during a set point change from 17°C to 16°C at 0 seconds. Even though this is only a 1°C change in superheat, this is more than sufficient for controller comparison purposes. This is mainly due to the relative small level of noise that is observed – approximately ±0.1°C. Also, a 1°C change may seem small while changing superheat from 17°C to 16°C, however a change from 5°C to 4°C superheat may be considered more substantial even though the overall change in superheat is still 1°C. Therefore, a 1°C step change in the reference superheat is used for controller comparison throughout this chapter.

Figure 5.10 shows the experimental and simulation superheat response to a step change in reference with a Ziegler-Nichols tuned PID controller. This simulation environment is derived from the models identified in Chapter 4. The simulation response matches closely with the experimental data which indicates the accuracy of the identified model. The Ziegler-Nichols tuned controller exhibits a fast response showing some overshoot and oscillation. Figure 5.11 shows the control effort during the step change in reference. The valve abruptly changes by nearly 10% at 0 seconds to track the step change in superheat reference. During steady state regulation the valve opening oscillates by $\pm$ 1.5%.
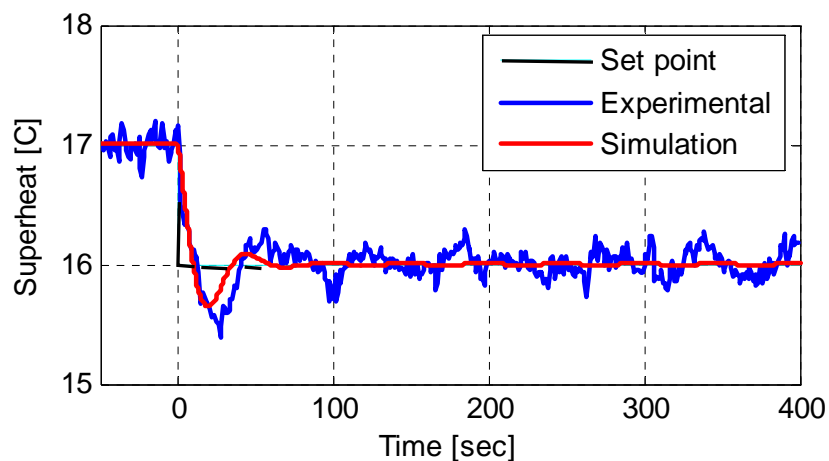

**Figure 5.10   Ziegler-Nichols tuned PID control response**
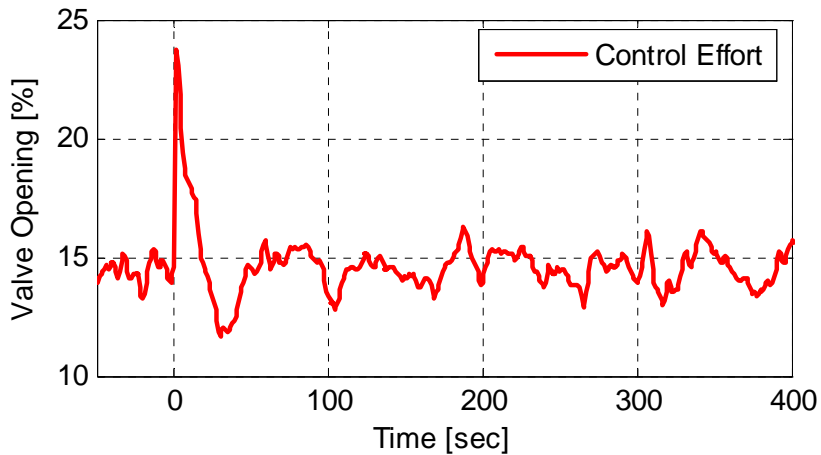
Figure 5.11   Ziegler-Nichols tuned PID control effort response

Figure 5.12 show the SIMC tuned controller while regulating superheat during a set point change from 17°C to 16°C. The SIMC tuned controller has a relative slower response with less overshoot. There is also good correlation between simulation output and experimental data. Figure 5.13 shows the control effort during the step change in reference superheat. During the step change the valve opening changes by approximately 4% and has a steady state oscillation of ± 0.5°C. From these results it is clear that the SIMC tuning method provides more robust feedback in terms of sensitivity to system noise whereas the Ziegler-Nichols method provides a higher level of performance in terms of reference tracking. The amount of steady state actuation is an important consideration in the development of the EEV controller since valve life is affected by the amount of actuation. A controller which modestly actuates the valve at steady state will prolong the life of the valve which is extremely desirable.
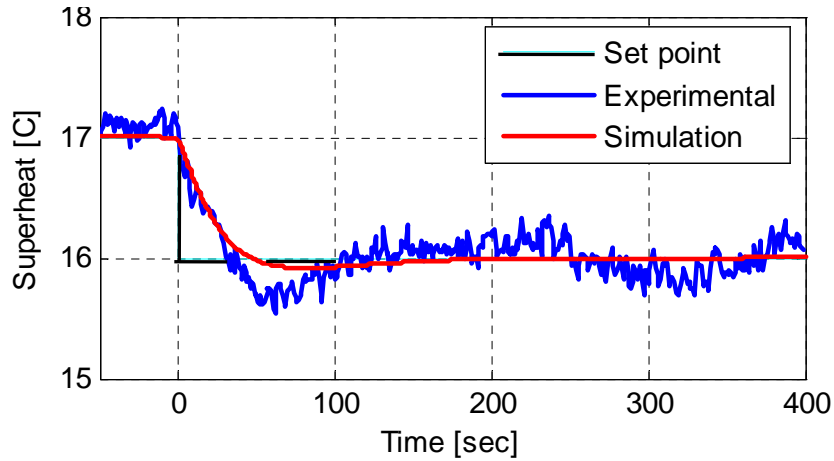
Figure 5.12   SIMC tuned PID control response
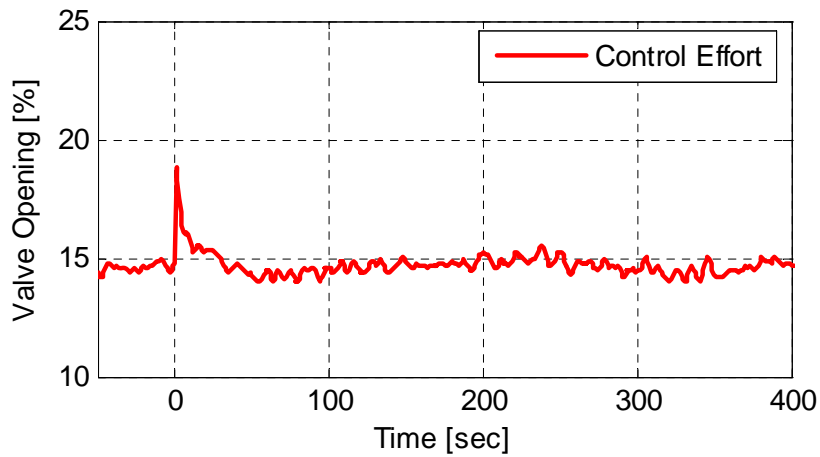
**Figure 5.13   SIMC tuned PID control effort response**

As the PID controller is used to regulate superheat at lower levels the PID controller gains become smaller to maintain stability. At lower superheat levels the time delay of the model between valve opening and the superheat increases which reduces the stability of the system. The PID controller is tuned for regulation at 8°C superheat using the model identified in Chapter 4. The SIMC tuning method is used since this method gives a controller which is relatively robust to system noise.

$$t_{dV} = 13, M_V = -5, \tau_V = 93 \quad\quad\quad\quad (5.8)$$

$$K_c = \frac{.5 * \tau_V}{M_V * t_{dV}} = -0.71 \qu\quad\quad\quad (5.9)$$

$$K_p = K_c = -0.71\,, \quad K_I = K_c / \tau_V = -0.0077\,, \quad K_D = 0.0 \tag{5.10}$$

The controller gains for the SIMC tuned controller for 8°C superheat regulation are shown in Equation 5.10. The PID gains are considerably smaller compared to the controller gains tuned for regulation at 16°C as shown in Equation 5.7. The PID controller is experimentally implemented on the experimental test stand during a 400 RPM change in compressor seed from 1400 RPM to 1000 RPM. This change in compressor speed represents a common compressor speed fluctuation in a variable speed system when the user changes the temperature set point. Figure 5.14 shows the superheat response during this disturbance. The superheat deviates by nearly 4°C during the disturbance risking compressor flooding and oil losses. A deviation this large in superheat limits the ability for the design engineer to specify a low superheat set point for improved system efficiency.
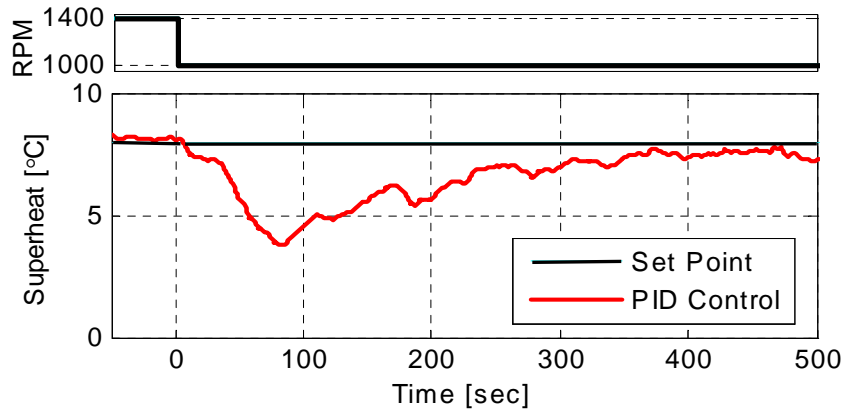

Figure 5.14   Compressor speed disturbance during low superheat regulation

Proportional-integral-derivative control is the preferred method of superheat regulation in industry due the relative ease of implementation and satisfactory performance. However, this controller prevents a low superheat set point due to poor disturbance rejection. It has been shown in this section that the PID controller lacks transient and steady state performance while regulating superheat. The remainder of this chapter investigates control features that may supplement the PID controller to improve transient and steady state performance to ultimately allow for a lower superheat set point.

Figure 5.15 presents a flow chart which may act as a guide during the development of a superheat control algorithm for superheat control with an EEV. The three control structures

developed in the remainder of this chapter serve to improve either transient or steady state performance. A scheduled feedforward controller is developed to improve transient performance during system disturbances while considering the nonlinear dynamics. Also, a gain scheduled feedback controller is developed to account for the nonlinear dynamics in the feedback path to maintain system-wide transient performance. The steady state performance of the PID controller is improved with the development of the multiple feedback control configuration. Section 5.5 develops the scheduled feedforward controller, followed by the development of the gain scheduled feedback control configuration in Section 5.6. Section 5.7 presents the multiple feedback control framework.
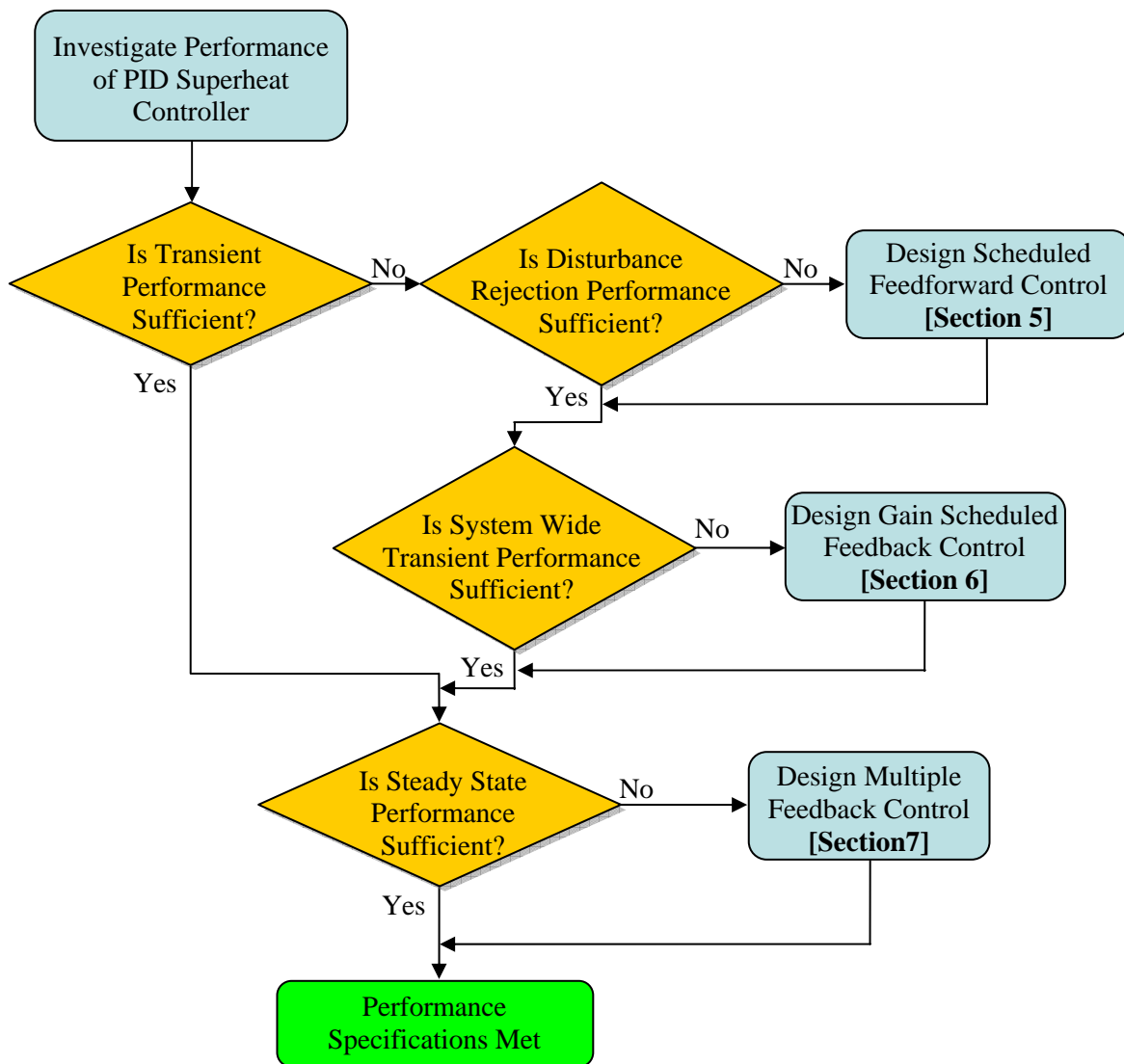
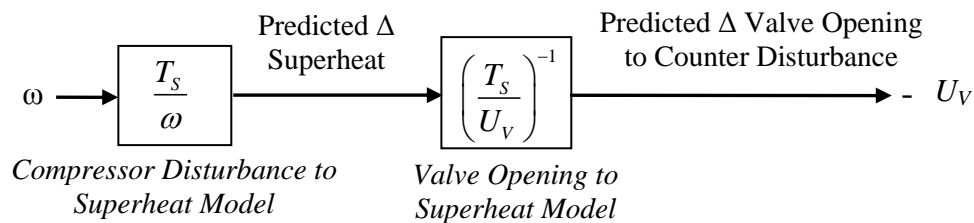**Figure 5.15   Control development flow chart**

5.5   Feedforward Control

Variable capacity vapor compression systems have recently been the focus of much research due to the potential energy savings these systems may provide. Strong coupling between control parameters require advanced control techniques to meet performance requirements. To realize the potential energy savings, evaporator superheat must be regulated to a low level to ensure system efficiency. With variable speed systems this task becomes more difficult due to fluctuating capacity demands. Keir et al. showed that significant efficiency improvements may be realized with a variable capacity system compared to a fixed capacity system [4].

To mitigate the coupling between compressor speed and superheat, a feedforward control structure is implemented to reduce the effects of such disturbances. This section proposes a method where the nonlinear dynamics of the vapor compression cycle are taken into account to allow for precise disturbance rejection over system-wide operating conditions.

5.5.1 Feedforward Method

To decouple the compressor speed from superheat a standard feedforward technique is implemented where a model inversion is used to cancel the disturbance effects. This method compensates a disturbance by first predicting how the disturbance will influence the output. This controller then determines how to adjust the input to cancel the anticipated change in output. In this case, the change in valve opening is calculated to suppress the change in superheat due to the disturbance.

$$\omega \rightarrow \boxed{\frac{T_S}{\omega}} \xrightarrow[\text{Superheat}]{\text{Predicted } \Delta} \boxed{\left(\frac{T_S}{U_V}\right)^{-1}} \xrightarrow[\text{to Counter Disturbance}]{\text{Predicted } \Delta \text{ Valve Opening}} - \ U_V$$

Compressor Disturbance to   *Valve Opening to*
*Superheat Model*   *Superheat Model*

Figure 5.16   Feedforward Control Structure

This method requires two models to determine the feedforward control effort as shown in Figure 5.16. The first model required is that between compressor speed and evaporator superheat. The second model that is required is between valve opening and evaporator

superheat. The compressor speed is the input to the first model where the output of the first model is the predicted change in superheat due to a change in compressor speed. The predicted change in superheat is the input to the inverted model between valve opening and superheat. The output of the second model is the change in valve opening which will counteract the effect of the compressor speed disturbance.

The feedforward compensator is evaluated off-line by multiplying the first model by the inverse of the second model. These models are multiplied by one another and implemented as a single element, G_{FF}, in the control structure as presented in Figure 5.17. The output of the feedforward compensator is subtracted from the control effort to counter the disturbance.
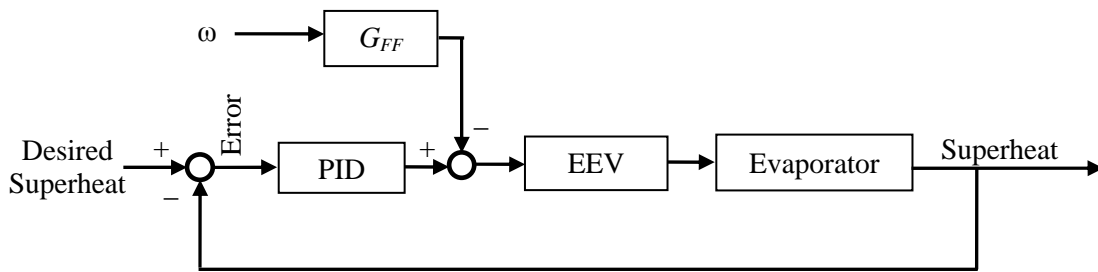
Figure 5.17   Overall feedforward control structure

5.5.2 Feedforward Development

This section develops the feedforward compensator using the models identified in Chapter 4. Using the method discussed in the previous section the feedforward compensator reduces to Equation 5.11. For simplicity, the delay time of each model is omitted here and considered at the end of this section. The magnitude M_ω depends on the compressor speed, ω, and the magnitude M_V depends on the evaporator inlet air temperature, T_I, as identified in Chapter 4. During the development of the feedforward compensator the evaporator air inlet temperature is considered constant. This assumption is relaxed when the controller is validated in Chapter 6.

$$G_{FF} = \frac{T_S}{\omega}\left(\frac{T_S}{U_V}\right)^{-1} = \frac{-M_\omega(\omega)\cdot(\tau_V s+1)}{M_V(T_I)\cdot(\tau_\omega s+1)}$$ (5.11)

The time constant of each model in Equation 5.11 is on the same order of magnitude, on the order of 100 seconds as shown in Chapter 4. Figure 5.18 shows the contribution of the

dynamic feedforward compensator, shown in Equation 5.11, during a step change in compressor speed. For the purpose of this investigation the response of the dynamic compensator can be reasonably approximated as a step function. Therefore, to reduce complexity the time constants are cancelled in Equation 5.11 since the performance is not significantly influenced. The feedforward compensator reduces to a static gain as shown in Equation 5.12.
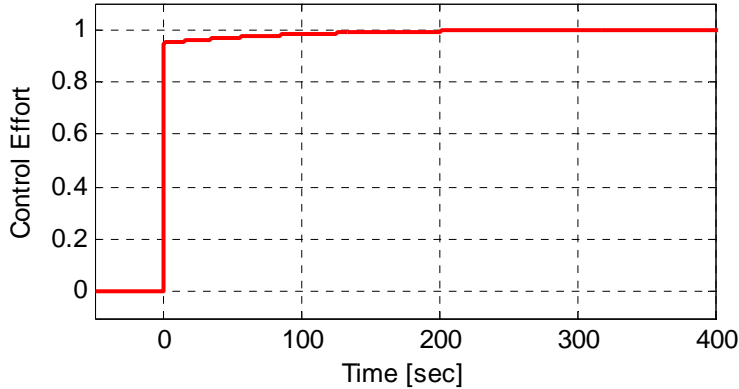
Figure 5.18   Feedforward control effort from dynamic compensator

$$G_{FF} = \frac{-M_\omega(\omega)}{11} \qquad (5.12)$$

Now that the feedforward compensator has been reduced, the time delay of each model is introduced. Equation 5.13 shows the feedforward compensator for increasing compressor speed, and Equation 5.14 shows the feedforward compensator for decreasing compressor speed. There are two different compensators for increasing and decreasing compressor speeds since the dynamics are different as shown in Chapter 4.

$$G_{FF\uparrow} = \frac{-M_\omega(\omega) \cdot e^{-10s}}{11} \qquad (5.13)$$

$$G_{FF\downarrow} = \frac{-M_\omega(\omega) \cdot e^{15s}}{11} \qquad (5.14)$$

The increasing feedforward compensator has a time delay of 10 seconds. In this case, the valve is adjusted 10 seconds following a compressor speed fluctuation. On the other hand, the decreasing feedforward compensator adjusts the valve opening 15 seconds prior to a compressor speed fluctuation. Adjusting the valve prior to a compressor speed fluctuation is not practical

since a priori information of the compressor speed is not available to the controller. The time advanced portion of Equation 5.14 is therefore omitted and the decreasing feedforward compensator is taken to be a static step as shown in Equation 5.15.

$$G_{FF\downarrow} = \frac{-M_\omega(\omega)}{11}$$
(5.15)

5.5.3 Mapping Development

The magnitude of the transfer function between compressor speed and superheat, shown in Equation 5.12, depends on the compressor speed as shown in Chapter 4. The nonlinear dynamics of the vapor compression cycle must be appropriately accounted for by scheduling the feedforward compensator with compressor speed. Figure 5.19 shows the feedforward gain as a function of the compressor speed. This correlation was identified using the identification from Chapter 4 along with Equation 5.12. At small compressor speeds the feedforward gain is large since the coupling between compressor speed and superheat is relatively strong at small compressor speeds.
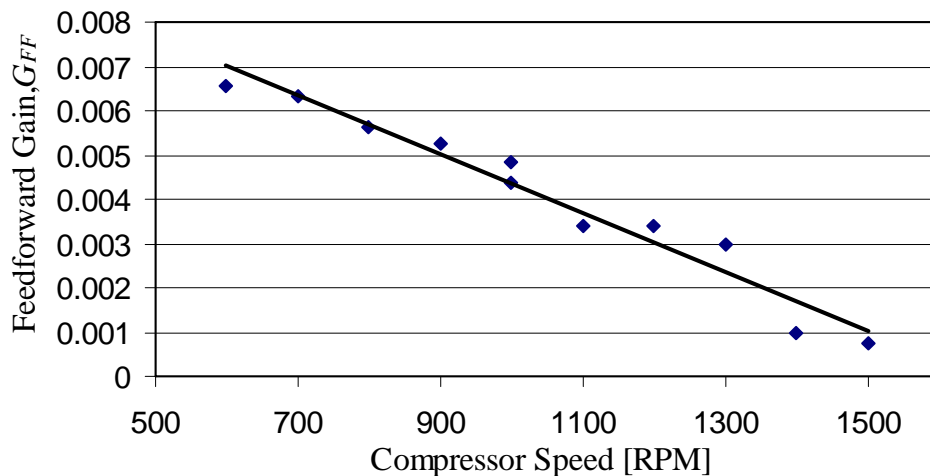
Figure 5.19   Scheduled feedforward compensator gain

The feedforward gain relation shown in Figure 5.19 was extrapolated from data obtained by stepping the compressor speed in 100 RPM increments. If a disturbance occurs where the compressor speed changes by less than 100 RPM the feedforward gain may be taken directly from Figure 5.19 since this will provide good compensation as long as the change in compressor speed is less than 100 RPM. However, if a compressor disturbance is large (e.g. 400 RPM) then

using the feedforward gain directly from Figure 5.19 will provide an inaccurate prediction of the change in superheat.
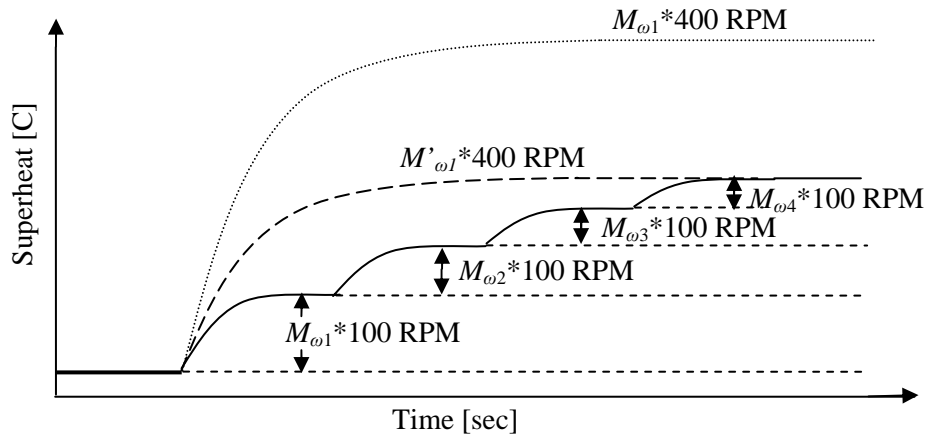
**Figure 5.20   Using M to predict the change in superheat results in overestimation**

To explain this in detail, the solid line in Figure 5.20 shows how evaporator superheat responds to four consecutive 100 RPM steps in compressor speed. The variables $M_{\omega 1}$, $M_{\omega 2}$, $M_{\omega 3}$, and $M_{\omega 4}$ represent the magnitude of the transfer function between compressor speed and superheat at those specific compressor speeds. If the system is operating at the initial condition and the compressor speed changes by 400 RPM, one method to estimate the change in superheat is to multiply the change in compressor speed by $M_{\omega 1}$ (the magnitude at the current compressor speed). This method overestimates the change in superheat and is shown as the dotted line, $M_{\omega 1}$*400 RPM, in Figure 5.20. This method overestimates the change in superheat since the nonlinear relation between compressor speed and superheat is ignored.

To accurately estimate the change in superheat for a compressor speed disturbance larger than 100 RPM, the gain must not be taken directly as $M_{\omega 1}$. However, a modified gain $M'_{\omega 1}$ must be used instead to accurately predict the change in superheat, where $M'_{\omega 1}$ is calculated as the average of $M_{\omega 1 \to 4}$ as shown in Equation 5.17. The dashed line in Figure 5.20 shows that $M'_{\omega 1}$ accurately predicts the change in superheat during a compressor speed change larger than 100 RPM.

$$400 * M'_{\omega 1} = 100 * M_{\omega 1} + 100 * M_{\omega 2} + 100 * M_{\omega 3} + 100 * M_{\omega 4} \qquad (\,5.16\,)$$

$$M_{\omega 1}^{'} = \frac{M_{\omega 1} + M_{\omega 2} + M_{\omega 3} + M_{\omega 4}}{4} \qquad (5.17)$$

Using the linear fit for M_{ω} from Chapter 4, a mapping for M'_{ω} is created using Equation 5.17. Figure 5.21 shows the mapping of M'_{ω}, where the magnitude is dependent upon initial compressor speed, RPM_{IC}, and the magnitude change of the compressor speed disturbance, referred to as ΔRPM.
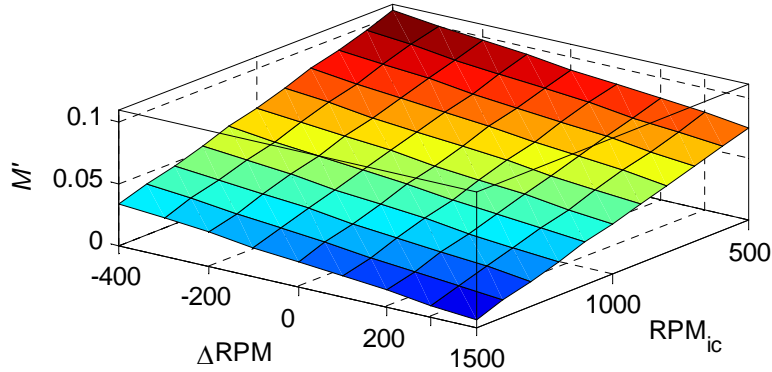
Figure 5.21   Mapping of magnitude M'

The magnitude of the feedforward compensator is now calculated using Equation 5.12. Figure 5.22 shows the magnitude of the feedforward compensator as a function of ΔRPM and the initial compressor speed, RPM_{IC}. During a compressor disturbance the controller finds the magnitude of the feedforward compensator by using Figure 5.22 as a lookup table.
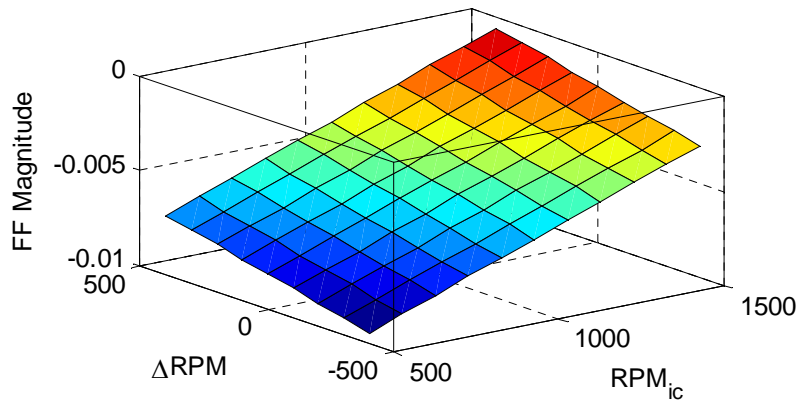
Figure 5.22   Feedforward magnitude mapping

As discussed earlier, if the compressor speed disturbance is equal to or smaller than a 100 RPM the mapping in Figure 5.19 is sufficient to use for the scheduled feedforward compensator.

More specifically, if the slope of the compressor disturbance is equal to or less than 100 RPM/sampling interval then the mapping in Figure 5.19 is sufficient. For most applications the mapping in Figure 5.19 is sufficient since it is unlikely that the compressor will change by more than 100 RPM over the course of the sampling interval. Therefore, the mapping shown in this section may not be required for some AC&R applications. However, it is required while testing the performance of the developed controllers to 400 RPM step changes in compressor speed.

5.5.4 Feedforward Results

The feedforward mapping shown in the previous section is tested at various initial compressor speeds and compressor speed changes. The following results compare scheduled feedforward control of superheat with that of a PID controller. For ease of comparison, a compressor speed step change of 400 RPM is used to test the performance of the developed controllers. A 400 RPM change in compressor speed is representative of the change in compressor speed during a temperature set point change for a variable speed system. The PID controller is tuned with SIMC rules while regulating superheat to 8°C. All figures show the compressor speed disturbance at 0 seconds.

Figure 5.23 shows superheat regulation during a compressor speed disturbance from 1000 RPM to 600 RPM. The feedforward magnitude is determined to be -0.0062 from the look-up table. The feedforward compensator adjusts the valve opening by an amount of -2.48 % during the compressor speed change at 0 seconds. This result illustrates how scheduled feedforward control significantly reduces the risk to compressor damage during transients.
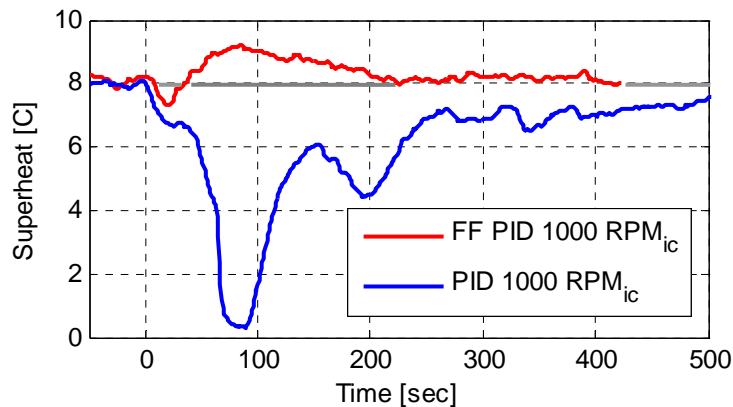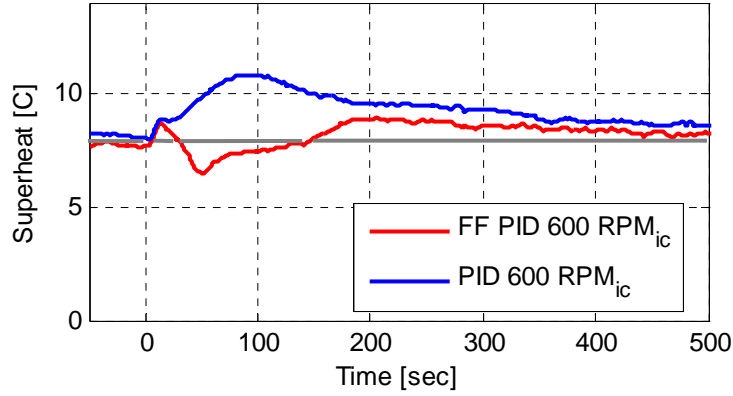

Figure 5.23   Superheat response to a 400 RPM step decrease

Figure 5.24 shows the scheduled feedforward compensator regulating superheat during a compressor speed disturbance from 1400 RPM to 1000 RPM. In this case the initial compressor speed, RPM_{IC}, is at a larger level of 1400 RPM. The feedforward magnitude is determined to be -0.0037 from the lookup table. During the compressor disturbance the feedforward compensator closes the valve by 1.48%. In this case the valve is closed by a smaller amount since there is less coupling between compressor speed and evaporator superheat at larger compressor speeds. Again, the PID controller allows superheat to deviate to an unsafe level, while the scheduled feedforward controller effectively compensates the disturbance.
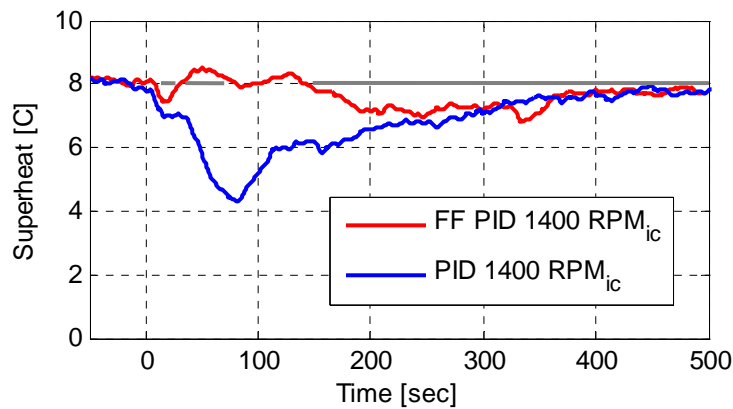
**Figure 5.24   Superheat response to a 400 RPM step decrease**

A 400 RPM compressor speed increase disturbance is shown in Figure 5.25, where the compressor speed is changed from 600 to 1000 RPM. The feedforward compensator takes the form of Equation 5.13 with a 10 second time delay. The PID controller allows superheat to substantially increase above the set point of 8°C. In contrast, the feedforward controller significantly reduced set point deviation during the compressor speed disturbance.

Figure 5.25   Superheat response to a 400 RPM step increase

To quantitatively evaluate the feedforward control performance, the maximum deviation from set point and root mean squared (RMS) error are used as performance indicators. These variable are used since they capture the amount superheat has deviated from the set point during operation. The root mean squared error is calculated as shown in Equation 5.18. The root mean squared error is the mean error during the test and is illustrated in Figure 5.26.

$$RMS\ error = \sqrt{\frac{\sum \left(SH - SH_{Desired}\right)^2}{n}} \tag{5.18}$$
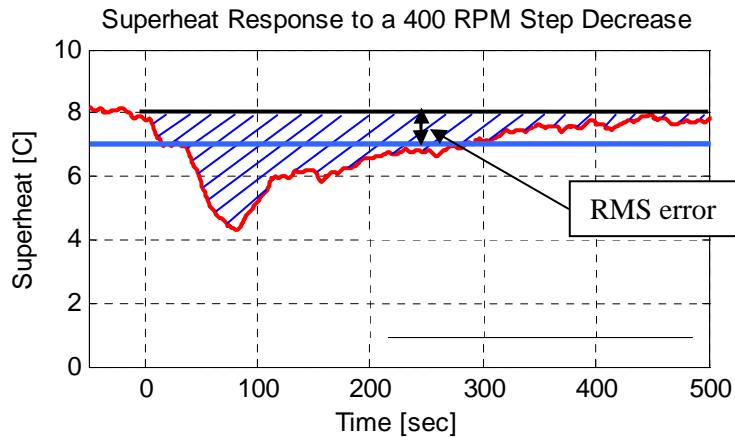
Figure 5.26   Illustration of RMSE

Table 5.2 presents the performance metrics for the responses shown in the previous results. The scheduled feedforward PID controller is capable of regulating superheat with a

significantly smaller maximum deviation and RMS error for each case. Figure 5.27 visually compares the maximum superheat deviation of each case.

**Table 5.2   Evaluation of controller performance**

	400 RPM Decrease 1000 RPM$_{ic}$		400 RPM Decrease 1400 RPM$_{ic}$		400 RPM Increase 1000 RPM$_{ic}$	
Metric	PID	FF PID	PID	FF PID	PID	FF PID
Max. Deviation	7.65°C	1.24°C	3.73°C	1.22°C	2.89°C	1.54°C
RMSE	2.52°C	0.46°C	1.43°C	0.51°C	1.46°C	0.57°C
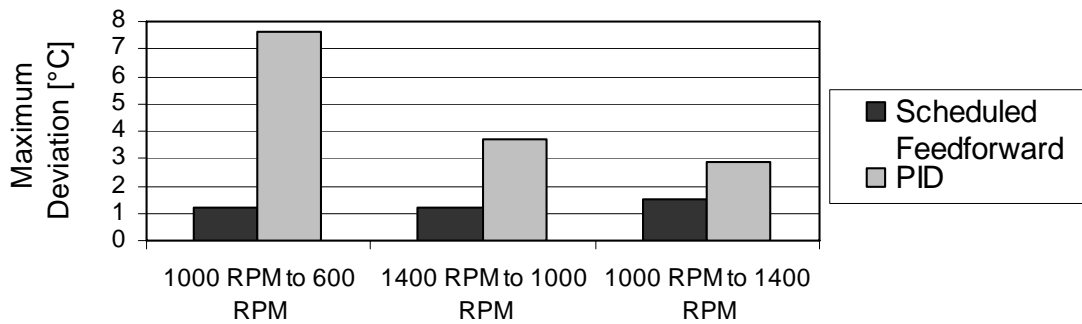
Figure 5.27   Control performance comparison

To emphasize the importance of a scheduled feedforward controller, results from an unscheduled feedforward compensator are shown in Figure 5.28. Here the feedforward compensator is tuned at 1400 RPM for a 400 RPM step decrease in compressor speed. The responses shown in Figure 5.28 are results from a 400 RPM step decrease in compressor speed at 0 seconds with the initial compressor speed, RPM$_{IC}$, shown in the legend.

When the initial compressor speed is 1400 RPM, the feedforward compensator regulates superheat precisely. However, when the initial compressor speed is less than 1400 RPM the feedforward control under compensates the disturbance, and when the initial compressor speed is larger than 1400 RPM the feedforward control over compensates the disturbance. This result illustrates the need for a scheduled feedforward compensator to account for the nonlinear dynamics of the vapor compressor cycle.
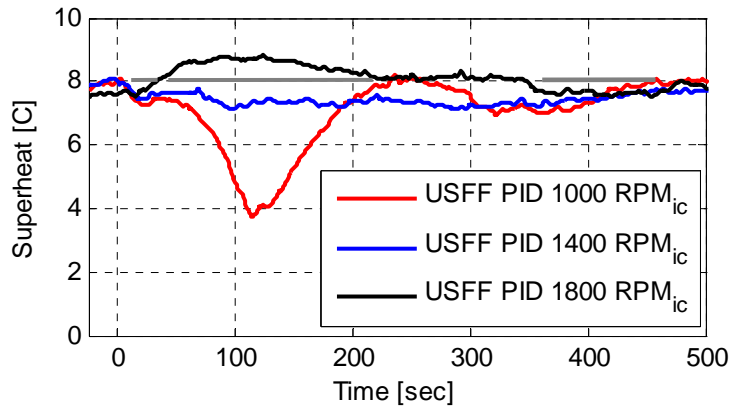
Figure 5.28   Unscheduled feedforward compensator

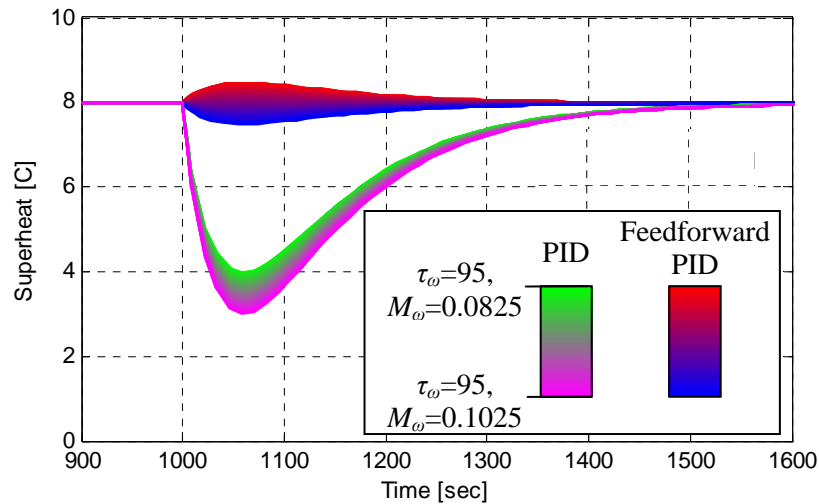## 5.5.5 Sensitivity Analysis

In this section the sensitivity of the PID controller and the feedforward controller are examined in a simulation environment. This simulation environment is derived from the empirical models identified in Chapter 4. The disturbance response of the PID and feedforward controller are evaluated during changes in the plant dynamics. For this investigation the magnitude and time constant of the model between compressor speed and superheat are varied by $\pm$ 10%. Figure 5.29 shows the feedforward and PID controller response during a change in the time constant, τ_ω, of compressor speed to superheat model. A compressor speed disturbance is simulated at 1000 seconds where the speed changes from 1200 RPM to 800 RPM. The tracking performance of the feedforward controller is decreased as the time constant deviates from its nominal value. Overall, the PID controller and feedforward controller are both relatively insensitive to uncertainty in the time constant. More importantly, the feedforward controller has substantially improved superheat regulation compared to the PID controller even with the presence of plant uncertainty.
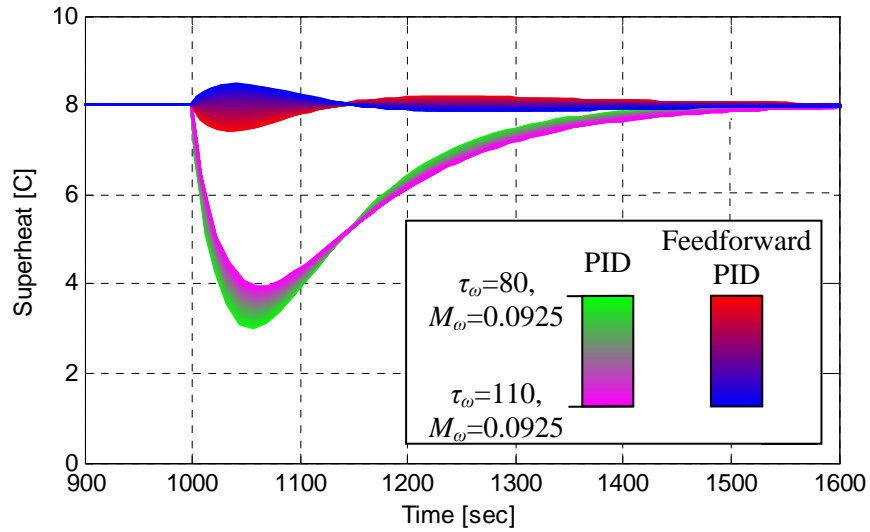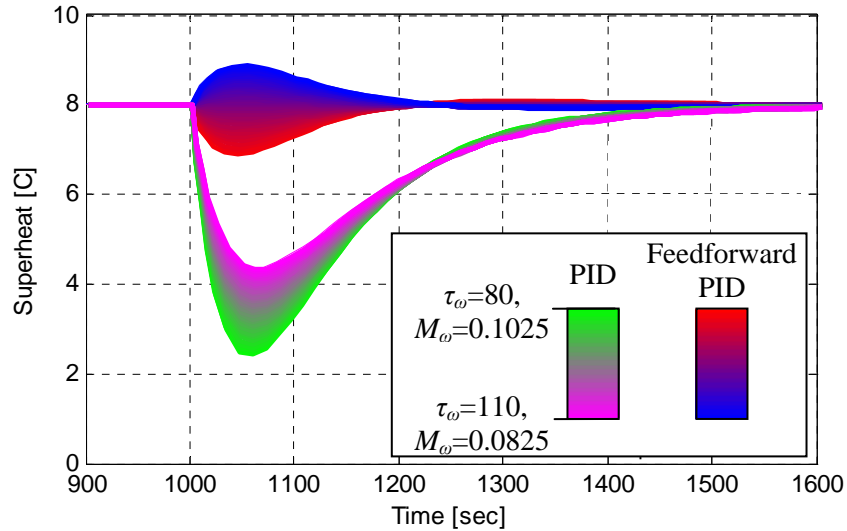
Figure 5.29   Sensitivity to change in time constant.

Figure 5.30 shows the sensitivity of the feedforward and PID controller to changes in the magnitude, M_ω, of the compressor to superheat model.   Again, both controllers are rather insensitive to plant uncertainty.

Figure 5.30   Sensitivity to change in gain

Figure 5.31 shows the sensitivity of the PID and feedforward controller to both a change in time constant and change in magnitude of the parameters of the model between compressor speed and superheat. Again, this result indicates that even with plant uncertainty the feedforward control retains a higher degree of disturbance rejection compared to the PID controller.

101

Figure 5.31   Sensitivity to both a change in gain and time constant

This section studied the robustness of the feedforward and PID controller in a simulation environment. The simulation results indicated that the PID and Feedforward controller have a similar robustness to plant uncertainty.   This result gives the designer confidence that implementing a feedforward control structure will not harm performance in the case of uncertain plant dynamics.

5.5.6 Feedforward Control Discussion

Due to the strong coupling between compressor speed and superheat the PID controller does not sufficiently regulate superheat to its desired level during compressor speed fluctuations. Feedforward control may be implemented to decouple the dynamics between compressor speed and superheat, allowing for better superheat regulation.

However, due to the strong nonlinear dynamics of the vapor compression cycle the feedforward compensator must be scheduled to allow for system-wide operation. The results shown in this section shows that a simple scheduled feedforward compensator effectively improves superheat regulation over the range of compressor speeds typically experienced by a variable speed system. Overall, scheduled feedforward control reduces the risks associated with regulation at low superheat and allows the designer to specify a low superheat set point for improved system efficiency.

5.6   Gain Scheduled Feedback Control

This section develops a gain scheduled feedback controller to maintain transient performance over system-wide operating conditions. As originally shown in Figure 5.15, this control method should be considered to account for the nonlinear dynamics of the vapor compression cycle if the transient performance is not sufficient with a PID Controller. In some cases, if the operating range of the system is sufficiently small where a fixed gain controller may be tuned to respond with the desired specifications (e.g. disturbance response, settling time, overshoot, etc.) in a small linear range about some nominal condition. However when a fixed gain controller is used at off-design points the controller response may fall short of the design specifications.

Feedback gain-scheduling is one control method that may be used to maintain the performance specifications during system-wide operation. The feedback gain scheduled controller is constructed by interpolating between a family of local controllers depending on the state of the scheduling variable. These local controllers are designed at different operating conditions through the use of linear control techniques (e.g. Ziegler Nichols, pole placement, etc.). This method of control has previously been referred to as a "divide-and-conquer" methodology where the nonlinear control problem is divided into many linear problems [13].

The results shown in this report use this "divide-and-conquer" technique where the models identified in Chapter 4 are used to develop local controllers. Linear control techniques are used to tune these local controllers to meet similar performance specifications. Consistent controller performance is desirable since the superheat set point is based on the superheat deviation during an anticipated disturbance. If each local controller has a similar performance the superheat set point may be set with a similar confidence that a disturbance will not risk component damage at different operating conditions.

Many parameters in the vapor compression cycle influence the dynamics between valve opening and superheat. Variables such as level of superheat, evaporator air inlet temperature, compressor speed, evaporator mass flow rate, and more may be considered for the scheduling variable. However, not all of these variables may be ideal for certain applications. An ideal scheduling variable is one which changes during normal operation and significantly influences the plant dynamics.

Figure 5.32 shows experimental results where a fixed gain controller, tuned for regulation at 18°C superheat, is used to regulate superheat over a large range of superheat levels. At the design point of 18°C superheat, this controller has a fast response with small overshoot. For this case, a response such as this is considered to meet the design specifications. When this controller is used to regulate superheat at larger levels the controller response shows slightly less overshoot. On the other hand, when this controller is used to regulate superheat at a smaller level the response becomes very oscillatory to the point where marginal stability is observed. This result demonstrates one possible need for feedback gain scheduling. In this case local controllers would be interpolated between depending on the state of the superheat measurement.
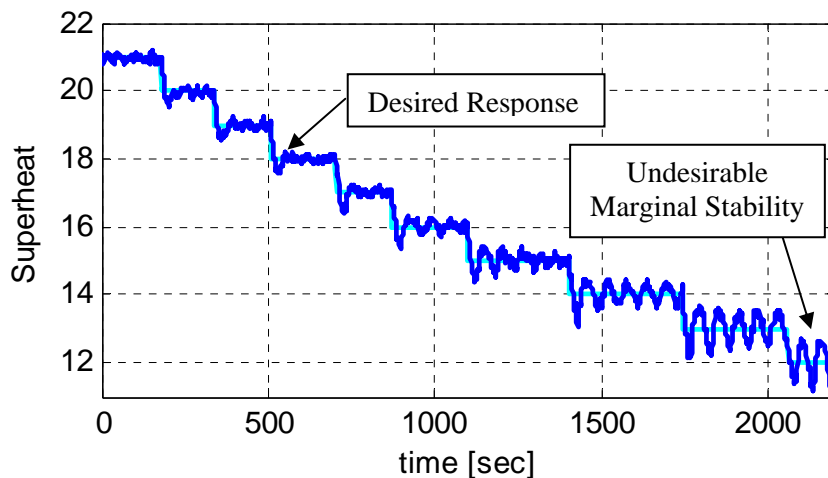
Figure 5.32   Change in closed loop dynamics depending on level of superheat

Feedback gain scheduling based on the level of superheat is applicable for certain situations in air conditioning and refrigeration systems such as during the defrost cycle. However, in many cases the superheat is maintained at a constant level during the majority of the system's cycle. Therefore this report considers a scheduling variable which changes more often during the normal operation of an AC&R system.

One system parameter that is likely to change in many air conditioning and refrigeration systems is the load on the evaporator. The load on the evaporator depends on such parameters as fan speed, humidity, and inlet air temperature (some of which are dependent upon ambient conditions while others depend on user set points). In this report the scheduling variable is taken as the evaporator air inlet temperature.

Evaporator air inlet temperature is an ideal scheduling parameter since in many cases the evaporator air inlet temperature is large at startup and decreases as the container is cooled. The evaporator fan pulls air in from the cooled space, making the evaporator air inlet temperature strongly correlated to the cooled space, or container, temperature. For example, in transport refrigeration the unit may reach temperatures well above 100°F before system startup. After system startup the temperature may be controlled to a level much below freezing. A change this large in evaporator air inlet temperature may significantly influence the dynamics between valve opening and superheat. The following sections describe the development of a gain scheduled feedback controller which is designed to maintain transient performance over system-wide operation.

5.6.1 Local Controller Design

This section discusses methods that may be used to tune local controllers to provide consistent performance. The main goal of gain scheduling feedback is to maintain system-wide stability and performance metrics. Therefore, a tuning method is investigated which provides similar stable closed loop performance.

One possible tuning method for the local controller design is through the use of simple tuning rules. The tuning procedures such as Ziegler-Nichols or SIMC rules have been shown in Section 5.4 to effectively tune a PID controller for superheat regulation. The SIMC tuning rule is used here to tune a PID controller for an evaporator superheat regulation at two different operating conditions: an inlet air temperature of 12°C and 25°C. Both of these design points have different dynamics which are shown in Chapter 4. The details of the SIMC tuning is not shown here, the reader is referred to Equation 5.6 and Equation 5.7. Figure 5.33 shows a step change in the desired superheat while using the tuned PID controllers at 12°C and 25°C inlet air temperatures. The blue curve in the figure shows the SIMC tuned controller designed at 12°C evaporator inlet air temperature regulating evaporator superheat with an evaporator inlet air temperature of 12°C. The red curve shows the SIMC tuned controller designed at 25°C evaporator inlet air temperature regulating evaporator superheat with an evaporator inlet air temperature of 25°C. It is clear that the performance of these two controllers is not consistent even though the same tuning method is used. Therefore, simple tuning rules are not ideal for the

tuning of the local controllers for the gain scheduled feedback controller since they do no provide consistent performance for the nonlinear system.
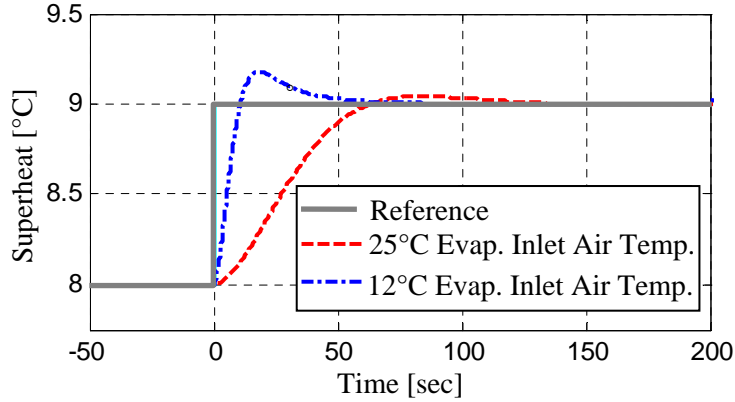
Figure 5.33   Simple tuning methods

Another tuning method that may provide consistent performance is pole placement. With this method the closed loop poles of the system are specified and the gains are determined to place the poles in a specified location. The dynamics of a system depends strongly on the location of the poles. Therefore, if the poles of each local closed loop controller are placed in the same location the system-wide performance will be consistent.

Using the Pade approximation a second order model is developed to account for the time delay between valve opening and superheat as shown in Equation 5.19. Equation 5.20 shows the closed loop transfer function where C is the controller of a PID type.

$$\frac{T_S}{U_V} = \frac{M_V(T_I)e^{-T_d s}}{\tau s + 1} \approx \frac{M_V(T_I)}{\tau s + 1}\frac{1}{T_d s + 1} = \frac{M_V(T_I)}{(\tau \cdot T_d)s^2 + (\tau + T_d)s + 1} \tag{5.19}$$

$$\frac{C\dfrac{T_S}{U_V}}{1 + C\dfrac{T_S}{U_V}} = \frac{\dfrac{M_V(T_I)}{\tau \cdot T_d}\left(K_D \cdot s^2 + K_P \cdot s + K_I\right)}{s^3 + \left(\dfrac{\tau + T_d}{\tau \cdot T_d} + \dfrac{K_D \cdot M_V(T_I)}{\tau \cdot T_d}\right)s^2 + \left(\dfrac{1}{\tau \cdot T_d} + \dfrac{K_P \cdot M_V(T_I)}{\tau \cdot T_d}\right)s + \dfrac{K_I \cdot M_V(T_I)}{\tau \cdot T_d}} \tag{5.20}$$

Since K_P, K_I and K_D show up in three out of the four coefficients in the characteristic equation it is possible to arbitrarily place the poles of the system. The closed loop poles of the system are placed at -0.06, -0.09, and -0.12 by choosing K_P, K_I, and K_D. These pole locations were chosen based on locations that have been shown experimentally to perform well.

106

Figure 5.34 shows the local controller responses during a step change in the reference. The dashed curve shows the PID controller tuned with pole placement at the local design point corresponding to an evaporator inlet air temperature of 25°C. The dash-dot curve shows the PID controller tuned with pole placement for the local design point corresponding to an evaporator inlet air temperature of 12°C. It is evident that the performances (rise time, overshoot, and settling time) of these controllers are very consistent. The slight difference in performance is due to a difference in the zero locations as shown in Table 5.3.
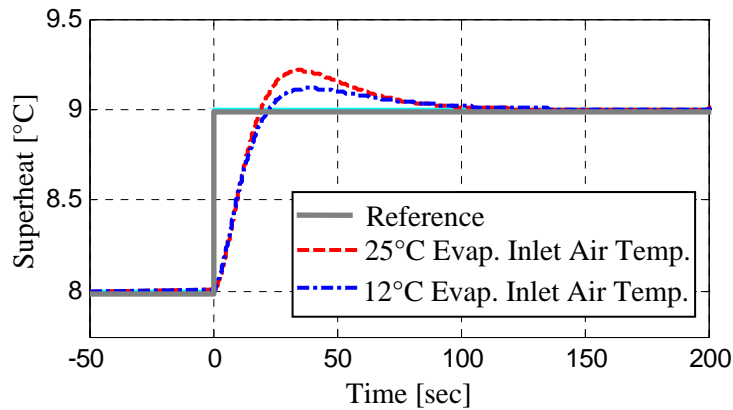
Figure 5.34   Pole placement

Pole placement in simulation has been shown to provide a good method of tuning local controllers to meet similar performance specifications. Table 5.3 shows the PID gains, pole locations, and zero locations of the controllers at the different operating conditions. The controller tuned for 25°C with pole placement has relatively large gains. These large gains may amplify the measurement and process noise causing an oscillatory control action at steady state during implementation. The large derivative gain is also of main concern during implementation due to the estimate of the derivative being sensitive to high frequency noise. This indicates that there may be experimental implementation issues while using the pole placement tuning method.

Table 5.3   Pole locations

Inlet Air Temperature	Pole Locations	Zero Locations	K_P	K_I	K_D
25°C	-0.12, -0.09, -0.06	-.08, -.05	5.58	0.16	45.09
12°C	-0.12, -0.09, -0.06	.33,-.03	0.74	0.02	-2.51

Pole placement does give consistent performance characteristics but it does not give gains that are practical for implementation. Therefore a model matching technique is pursued where a desired trajectory is first identified which is used as a reference for tuning the PID gains of the local controllers. This reference trajectory is first designed using a linear quadratic regulator (LQR) technique.

Below is the first order model between valve opening and superheat. It is important to note that the time delay is omitted from this analysis to allow a set of proportional and integral gains to be derived from the state feedback gains.

$$\frac{T_S}{U_V} = \frac{M_V(T_I)}{\tau s + 1} = \frac{M_V(T_I)/\tau}{s + 1/\tau} \tag{5.21}$$

The transfer function is put into state-space in the controllable canonical form. Where u is the control input to the valve and where y is the output superheat.

$$\dot{x} = \left[-\frac{1}{\tau} \right] x + [1] u \tag{5.22}$$

$$y = \left[\frac{M_V(T_I)}{\tau} \right] x \tag{5.23}$$

For the regulation problem a desired superheat is defined to formulate the error problem.

$$e = y_{ref} - y = y_{ref} - \frac{M_V(T_I)}{\tau} x \implies x = \frac{\tau}{M_V(T_I)} \left(y_{ref} - e \right) \tag{5.24}$$

$$\dot{e} = -\dot{y} = -\frac{M_V(T_I)}{\tau} \dot{x} \implies \dot{x} = -\frac{\tau}{M_V(T_I)} \dot{e} \tag{5.25}$$

$$-\frac{\tau}{M_V(T_I)} \dot{e} = \left[-\frac{1}{\tau} \right] \cdot \frac{\tau}{M_V(T_I)} \cdot \left(y_{ref} - e \right) + [1] u \tag{5.26}$$

$$\dot{e} = \left[-\frac{1}{\tau} \right] e + \underbrace{\left(-\frac{K}{\tau} u + \frac{1}{\tau} y_{ref} \right)}_{\bar{u}} \tag{5.27}$$

An integrated state is augmented to the state equation which allows both a proportional and integral gain to be derived using the LQR method.

$$z = \int_0^t e(t)dt \qquad (5.28)$$

$$\dot{z} = e \qquad (5.29)$$

$$\begin{bmatrix} \dot{e} \\ \dot{z} \end{bmatrix} = \underbrace{\begin{bmatrix} -1/\tau & 0 \\ 1 & 0 \end{bmatrix}}_{A} \begin{bmatrix} e \\ z \end{bmatrix} + \underbrace{\begin{bmatrix} 1 \\ 0 \end{bmatrix}}_{B} \bar{u} \qquad (5.30)$$

The quadratic cost function is used, where R and Q are tuned based on there interactions with error, integrated error, and control input. The LQR command in Matlab is used to determine the optimal state feedback gain K_1 and K_2.

$$J = \int_0^\infty \left[\bar{x}^T Q \bar{x} + \bar{u}^T R \bar{u} \right] dt \qquad (5.31)$$

$$\bar{u} = -\bar{k}\bar{x} = \begin{bmatrix} \bar{K}_1 & \bar{K}_2 \end{bmatrix} \begin{bmatrix} e \\ z \end{bmatrix} = -\bar{K}_1 e - \bar{K}_2 z \qquad (5.32)$$

Equation 5.33 shows the method in which the PI gains are derived from the optimal state feedback gains.

$$\bar{u} = -\frac{M_V(T_I)}{\tau} u + \frac{1}{\tau} y_{ref} = -\bar{K}_1 e - \bar{K}_2 z \;\Rightarrow\; u = \underbrace{\frac{1}{M_V(T_I)} y_{ref}}_{\text{static term}} + \underbrace{\frac{\tau}{K} \bar{K}_1 e}_{K_P} + \underbrace{\frac{\tau}{K} \bar{K}_2 z}_{K_I} \qquad (5.33)$$

After many simulations evaluating step response characteristics, the values of Q and R are chosen and shown in Equation 5.34. There is considerable weighting on the control action to ensure that there is minimal valve actuation at steady state to prolong valve life. There is also significant weighting on the error relative to the integrated error since an oscillatory control response is not desirable.

$$Q = \begin{bmatrix} 100 & 0 \\ 0 & .031 \end{bmatrix} \quad R = 10,000 \qquad (5.34)$$

Table 5.4   LQR gains for desired trajectory

Pole Locations	Zero Locations	K_P	K_I
-0.124, -0.014	-0.0138	2.42	0.03

Figure 5.35 shows the LQR tuned PI controller response to a change in set point. The red dashed line in Figure 5.35 is used as the desired trajectory for the model matching shown later. Specifically, each local controller is tuned to have a step response similar to the dashed line in Figure 5.35, referred to as the desired trajectory.
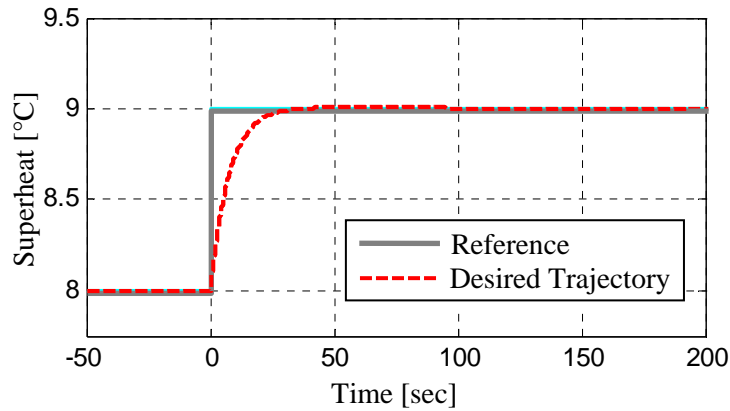

Figure 5.35   Desired closed loop superheat response

A technique called model matching is used to tune the PID gains for each local controller. The model matching technique tunes the gains of each local PID controller so that the response closely matches that of the desired trajectory shown in Figure 5.35. Liu and Daley have developed the model matching technique where a PID controller response is matched to the desired trajectory through an optimization routine where the error between the desired trajectory and the actual trajectory is minimized [45]. Here, the objective of model matching is to find the PID gains which make the first order plus time delay respond similar to the desired trajectory. A cost function is used to evaluate the error between the PID controller response and the reference trajectory. The cost function is shown in Equation 5.35 where y_d is the desired trajectory (shown in Figure 5.35) and where y_s is the response of the local first order plus time delay system with the set of gains K_P, K_I, and K_D.

$$J = \int_0^\infty \left(y_d(t) - y_s(t, K_P, K_I, K_D) \right)^2 dt \qquad (5.35)$$

The gains that minimize this cost function are found using a built in optimization routine, fminsearch, in Matlab. The optimization algorithm varies the three PID gains and calls a function which returns the cost. The cost is calculated within the function by running a simulation of the closed loop system and calculating the cost as shown in Equation 5.35. The optimization routine determines the set of gains (Kp, Ki, and Kd) which locally minimize the cost function. The global solution is irrelevant since the gains must be in a reasonable range for implementation. The gains which provide the minimal global cost may not be realistically implemented on an experimental system due to the size of the gains. In this optimization, the gains are restricted between 0 and 10. This range is chosen based on the dynamics of the experimental system. The local optimal solution is practical since gains much large than 10 will severely amplify system noise during experimental implementation.

It is important to note that the filter acting on the superheat feedback path and the filter on the derivative term are included in the simulation and optimization routine. This provides the most accurate representation of the experimental system. Figure 5.36 shows the magnitude and phase plot of a low pass filter which is used on the derivative term of the PID controller. The phase lag and magnitude attenuation influence the closed loop system performance. Therefore, including the feedback and derivative filters in the simulation further improves the ability to determine the controller gains which allow for the most consistent performance during system-wide operation.
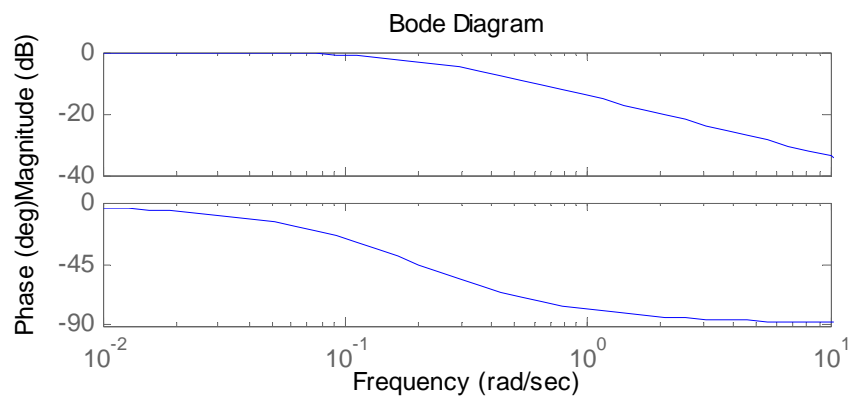

Figure 5.36   Derivative filter

During the model matching process the response of the local controller is designed to match a time shifted desired trajectory response. The desired trajectory is time shifted by the time delay of the local plant model. The model is matched to a time shifted desired trajectory since an oscillatory response would be obtained. Figure 5.37 shows the optimized PID controller response and the time shifted desired trajectory for a local plant at 25°C evaporator inlet air temperature.
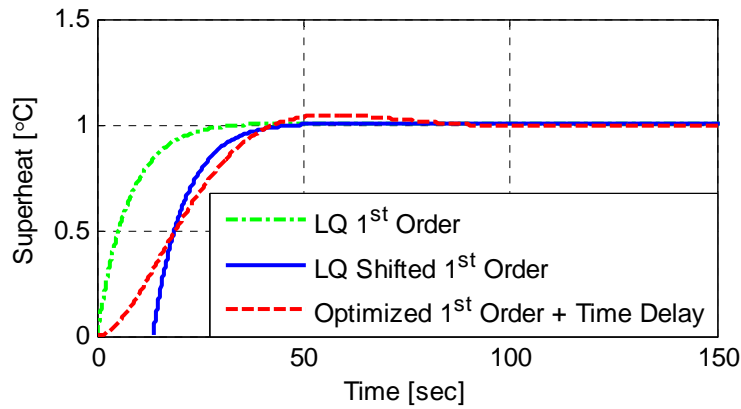
Figure 5.37   Shifted desired trajectory and model matched response

This process is used to design each local controller. Figure 5.38 shows the desired trajectory and the model matched controllers tuned at 25°C, 18°C, and 12°C evaporator inlet air temperatures.
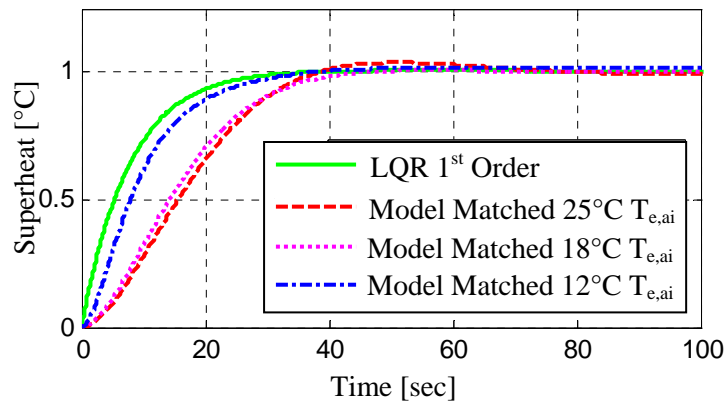
Figure 5.38   Model matched controller responses

Table 5.5 shows the gains of the local PID controllers tuned through model matching. The model matching method gives controller gains with reasonable magnitudes that are ideal for experimental implementation.

112

Table 5.5   Gains from LQ and model matching

Method, Inlet air temp	System Type	K_P	K_I	K_D
LQR, 25°C	1st Order	2.42	0.03	n/a
Model Match, 25°C	1st Order + Delay Time	1.14	.0107	6.22
Model Match, 18°C	1st Order + Delay Time	.72	.0083	1.68
Modal Match, 12°C	1st Order + Delay Time	.93	.0083	1.02

For comparison purposes, Figure 5.39 shows simulation results of a fixed gain controller used for superheat regulation at different evaporator inlet air temperatures. The simulation environment is derived from the identified models in Chapter 4. The PID controller response at different evaporator inlet air temperatures is significantly different from one another compared to the response trajectories shown in Figure 5.38. It is important to note that the range of temperatures tested is very small, ranging from 12°C to 25°C evaporator inlet air temperature, since only a small range may be experimentally tested. However, an AC&R system may experience much larger temperature fluctuations while operating in the field. Evaporator inlet air temperatures may reach far above 100°F to temperatures much below 0°F. For a scenario such as this, a gain scheduled feedback approach may be necessary for stability.
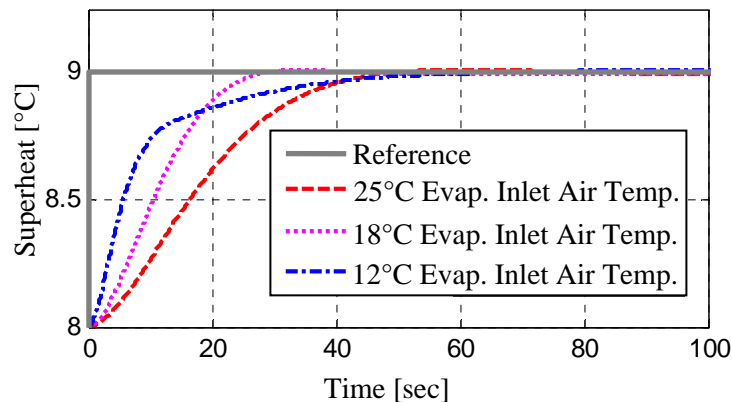

Figure 5.39   Fixed gain controller response

5.6.2 Controller Interpolation Development

Now that the local controllers have been designed, a method to switch between the local control outputs is designed. The four types of scheduling methods investigated here are the

switching, linear interpolation, ramp, and the arc-tan methods. The switching scheduling method is shown in Figure 5.40 where this method discretely switches between controllers midway between the design points. The sum of all control efforts must sum to 1 independent of the state of the scheduling variable. The dotted orange lines in the figures shown in this section represent the location of the locally designed controllers.
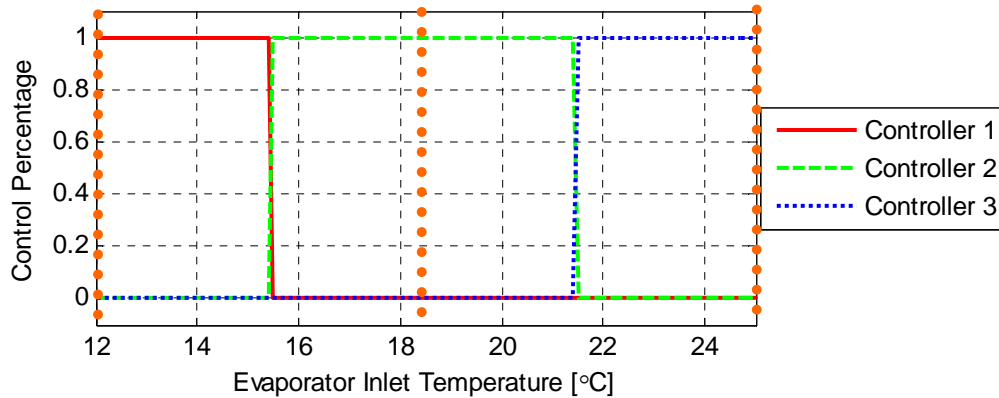

Figure 5.40   Switching gain scheduling

The linear interpolation method is shown in Figure 5.41 where the controller gains are simply interpolated when between design points. The ramp scheduling method is shown in Figure 5.42. This method is slightly different than the linear interpolation method where the designer specifies the slope of the ramp. Figure 5.43 shows the arc-tan scheduling method. This method is the most complex; however the transitions are always smooth unlike the other methods. The arc-tan method also has a design variable, m, which influences the transition width. Again, the output percentage of all controllers must sum to 1.
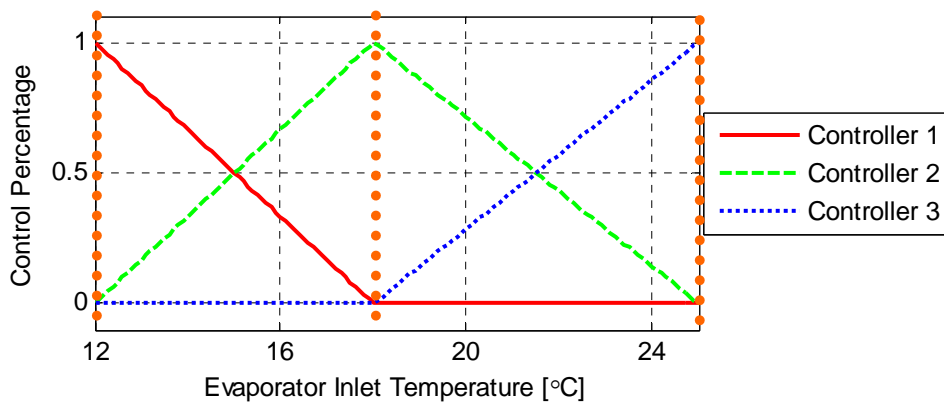
Figure 5.41   Linear interpolation gain scheduling

114
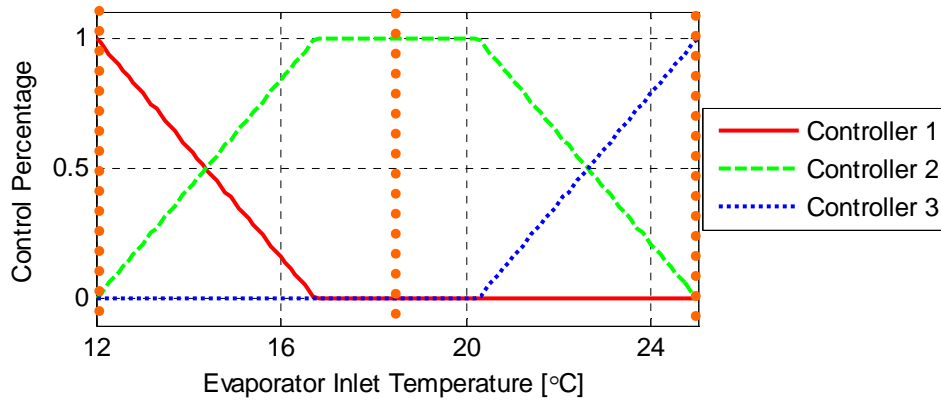
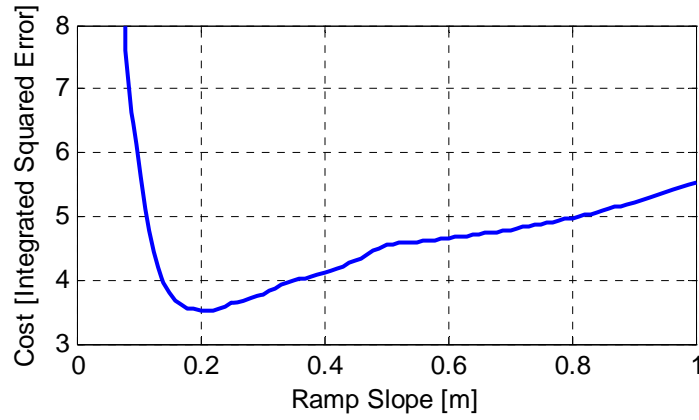**Figure 5.42   Ramp interpolation**
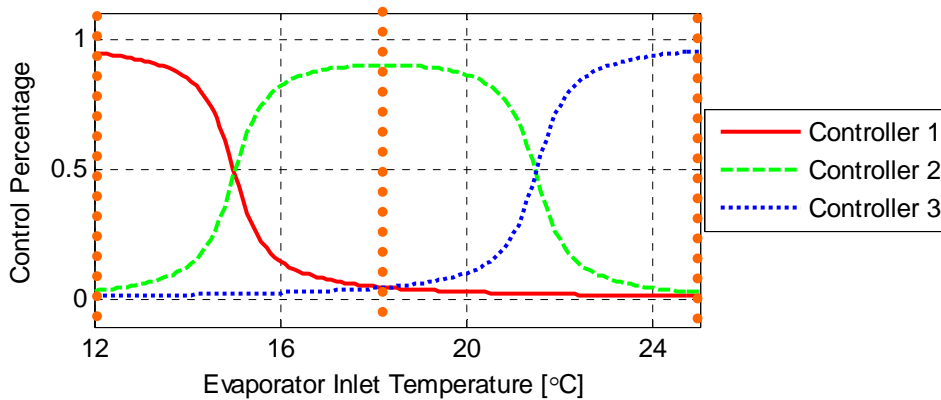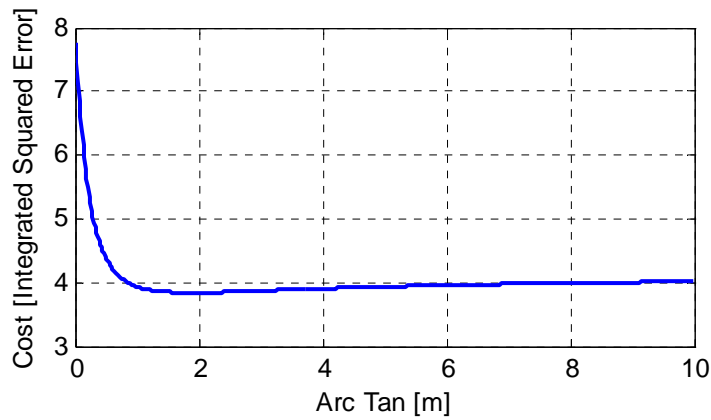

Figure 5.43   Arc-tan scheduling method

To evaluate which interpolation method performs most consistently the cost function shown in Equation 5.35 is used to determine how well each global control framework matches that of the desired trajectory shown in Figure 5.35. The simulation first calculates the global controller gains by using one of the scheduling methods. The plant coefficients are then determined using the identified models shown in Chapter 4. The closed loop step response is simulated and the cost is calculated.

Since there are no tuning parameters with the linear interpolation method and switching method there is a single cost. The cost of the linear interpolation method is equal to 3.7, and that of the switching method is 8.2. The tuning parameters that influence the ramp and arc-tan methods are varied to find the optimal design choice. The optimal slope of the ramp method and the optimal m of the arc tan method are determined to be 0.21 and 1.98 respectively as shown in Figure 5.44 and Figure 5.45. The cost corresponding to the optimal points are 3.53 and 3.84 for

the ramp and arc tangent methods respectively. Table 5.6 shows the cost of each scheduling method.

Figure 5.44   Optimal ramp slope

Figure 5.45   Optimal arc-tan slope

**Table 5.6   Scheduling method comparison**

Interpolation Method	Cost	Optimal Slope
Square	8.20	n/a
Linear Interpolation	3.70	n/a
Ramp	3.53	.21
Arc Tan	3.84	1.95

The scheduling method with the lowest cost is the ramp method with a cost of 3.53. It is important to note that the linear interpolation and arc tan methods also have a relatively low cost.

Of these scheduling methods, the linear interpolation method is most simple to implement since the controller gains are linearly based depending on the state of the scheduling variable.

5.6.3 Feedback Gain-Scheduling Results

This section presents experimental results obtained from the experimental test stand in the Mechanical Engineering Lab at the University of Illinois. The evaporator inlet air temperature is controlled via the emulation unit described in Chapter 3. First, the performance of a fixed gain controller is experimentally investigated. A fixed gain controller is tuned for regulation at an evaporator inlet air temperature of 25°C. This controller is used to regulate at off design points of 12°C, 18.5°C, 25°C, and 34°C evaporator inlet air temperature. The results presented in Figure 5.46 show a change in the reference superheat from 8°C to 9°C at 0 seconds. At the design point (25°C evaporator inlet air temperature) the controller performs well with small overshoot. When this controller is used at an off design point the response is either more sluggish (12°C $T_{e,ai}$) or more oscillatory (34°C $T_{e,ai}$). The difference in response is not substantial for the range of temperatures shown here. However, for certain AC&R applications the inlet air temperature fluctuations may be much larger and may require gain scheduling feedback control to maintain stability and performance. Also, it may be difficult to specify a superheat set point while using a fixed gain controller since the performance is not consistent.
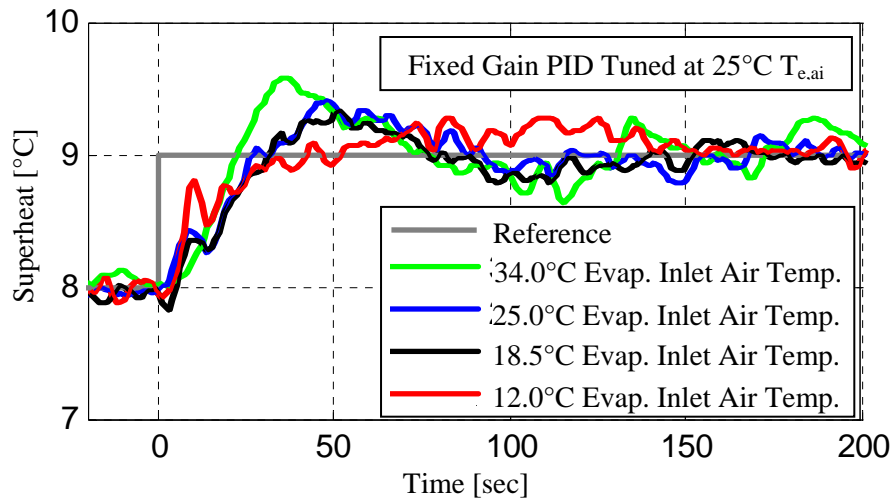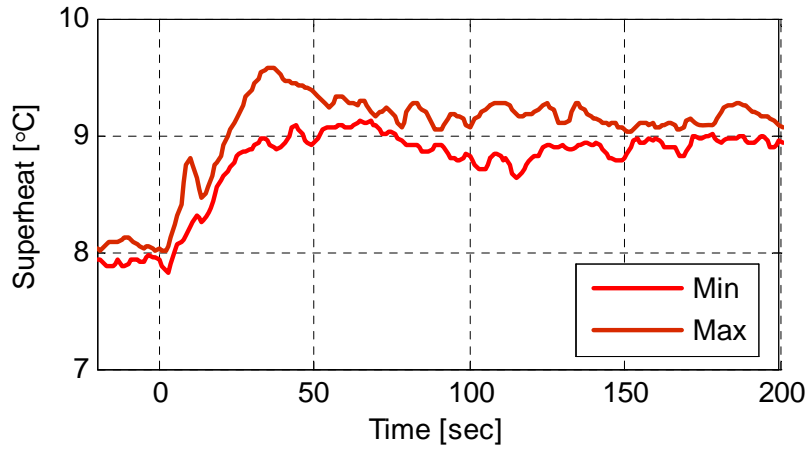

Figure 5.46   Fixed gain controller response

Figure 5.47 shows the experimental results of the switching type gain scheduled feedback controller while tracking a step change in reference at 0 seconds. The response trajectories at different evaporator inlet air temperatures are more consistent compared to the response shown in Figure 5.46. The gain scheduled feedback controller provides more consistent performance allowing the designer to be confident of the control loop's ability to regulate superheat to a low level for improved efficiency.
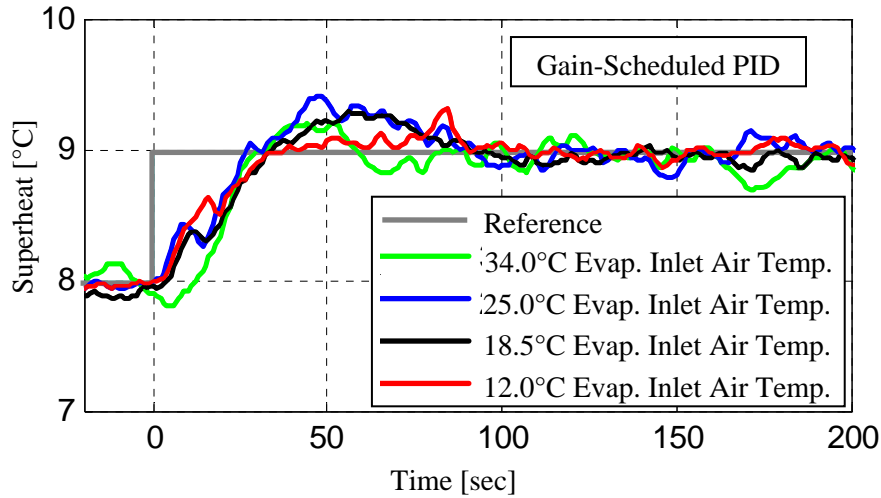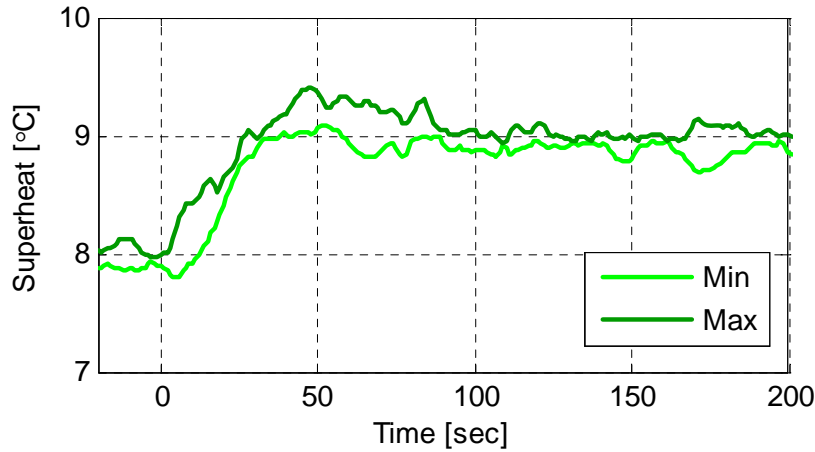

Figure 5.47   Gain scheduled controller response

To quantitatively compare the consistency of the gain scheduled feedback control framework a cost function is formulated to calculate the area between the responses. Specifically the area between the minimum and maximum points of the response is calculated using Equation 5.36. A small cost is desirable since a low cost indicates a higher degree of performance consistency. Figure 5.48 and Figure 5.49 shows the minimum and maximum points for the fixed gain and gain scheduled control response respectively. The cost function calculates the area between the two curves in these figures. Figure 5.50 visually compares the cost of the fixed gain and gain scheduled superheat controllers. The cost of the gain scheduled response is 54.16 where the cost of the fixed gain response is 68.45. As expected the gain-scheduled controller has a lower cost indicating that it has more consistent performance.
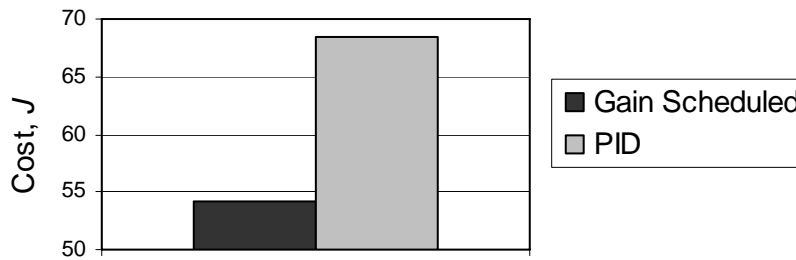
$$J = \int_{t=0}^{t=200} \left(T_{S\,\text{max}} - T_{S\,\text{min}}\right) dt \tag{5.36}$$

118

Figure 5.48   Fixed gain minimum and maximum response

Figure 5.49   Gain scheduled minimum and maximum response


Figure 5.50   Controller consistency

5.6.4 Gain Scheduled Feedback Discussion

Due to the nonlinear dynamics of the vapor compression cycle a nonlinear control method is implemented to allow for stable and consistent system-wide operation. This section

detailed the development and implementation of a gain scheduled feedback controller for superheat regulation. The results have shown that more consistent performance is possible with a gain scheduled feedback approach. This ultimately allows the design engineer to specify a low superheat set point without the risk to compressor damage during certain operating conditions.

5.7   Multiple Controller Regulation

Thus far, the scheduled feedforward controller and gain scheduled feedback controller have been developed to improve transient performance. As originally shown in Figure 5.15, the multiple feedback control configuration is developed to improve the steady state performance of the PID controller. The multiple feedback control configuration is designed to mitigate the tradeoff between performance and robustness that is inherent to the PID controller. Figure 5.51 illustrates the tradeoff that is inherent while tuning a PID controller. The PID controller can be tuned aggressively to be very responsive to disturbances and set point changes at the cost of heavy valve utilization. Large valve actuation will prematurely wear the EEV and shorten its effective lifetime. The PID controller may also be tuned conservatively for minimal valve actuation which would result in sluggish operation. The multiple feedback control configuration is designed to mitigate this tradeoff. The multiple feedback control configuration is designed to be responsive to disturbances while also having minimal valve actuation during steady state regulation. The tradeoff curves shown in Figure 5.51 are intended to illustrate the tradeoffs of the PID and multiple feedback controllers; these curves are not necessarily linear.
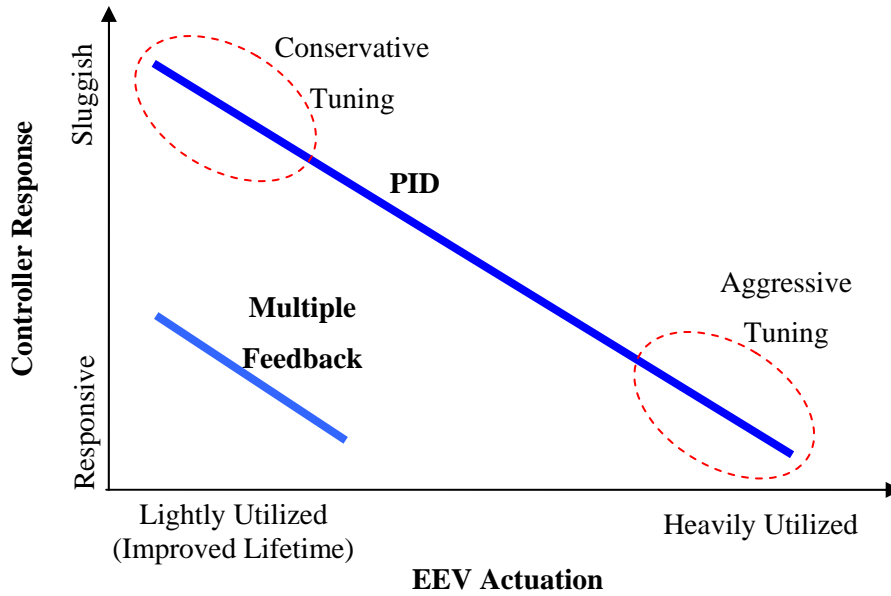
Figure 5.51   Performance tradeoff

In theory the steady state performance of a detuned controller and an aggressive controller are identical as long as both closed loop systems are designed to be stable. Figure 5.52 shows experimental steady state superheat regulation with an aggressive and detuned controller. In this work, the detuned controller is also referred to as a conservative controller. Both controllers maintain superheat in a similar error band of $16 \pm 0.25°C$.
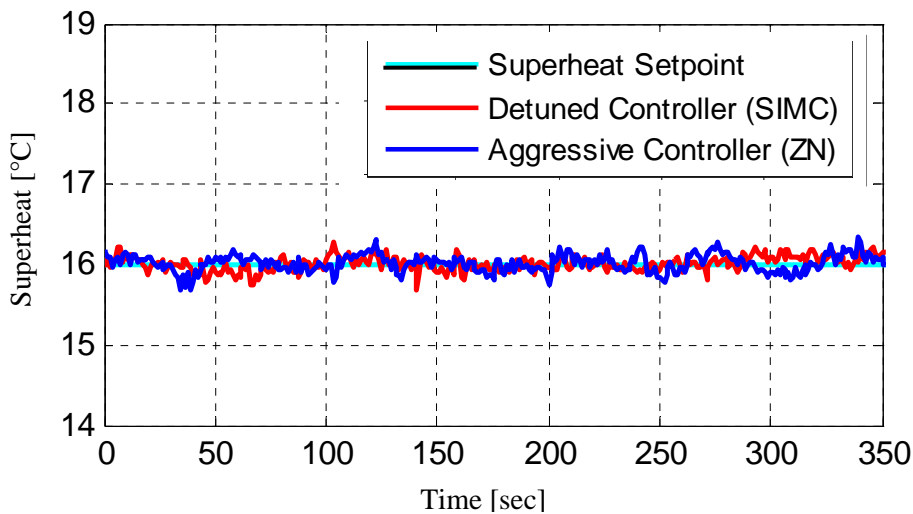

Figure 5.52   Steady state superheat regulation

The design engineer may be inclined to use an aggressive controller to regulate superheat due to fast reference tracking and good disturbance rejection. However, measurement and process noise from the system influence the steady state control effort. The aggressive controller has a control output that unnecessary actuates the EEV during steady state regulation as shown in Figure 5.53. This figure shows the control effort during the steady state superheat regulation shown in Figure 5.52. The process and measurement noise are amplified through the large gains of the aggressive controller which produces an oscillatory valve actuation signal at steady state. Figure 5.54 shows the power spectral density of the valve signal during steady state regulation. The valve signal corresponding to the aggressive controller has a larger power spectral density for the range of frequencies shown in Figure 5.54. This indicates that the aggressive controller utilizes the valve to a greater degree than the detuned controller. Control action during steady state regulation is an important consideration during the development of an EEV controller since AC&R systems must be designed to last decades. Therefore, it is paramount that the EEV controller minimally actuates the valve during steady state regulation to prevent premature valve degradation or failure.
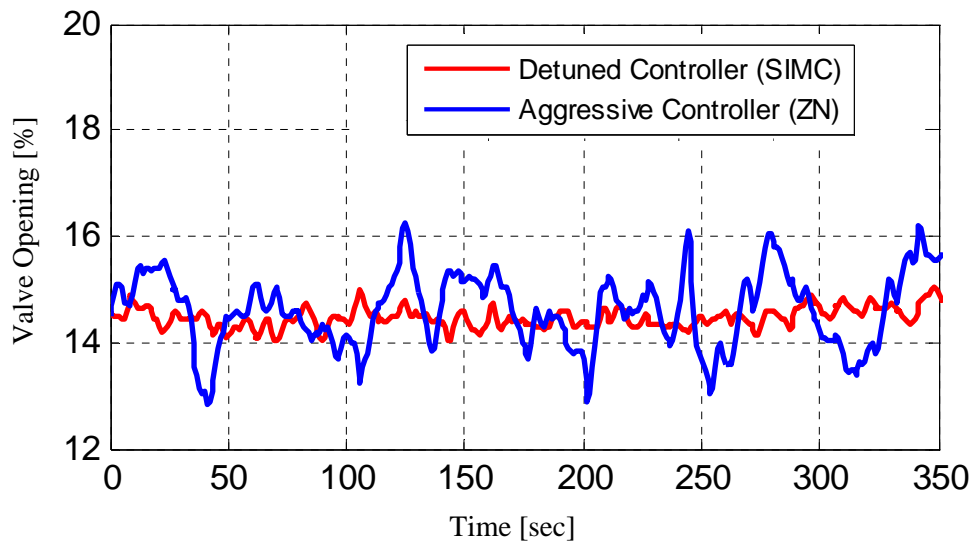

Figure 5.53   Steady state input actuation

122
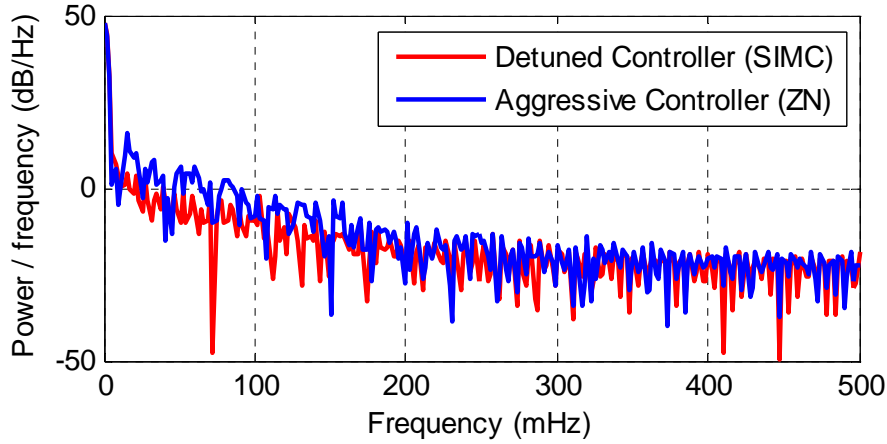
Figure 5.54   Power spectral density of the valve signal during steady state regulation

The transient performance of the control loop is also of great interest. Figure 5.55 shows experimental results showing the response of an aggressive and detuned controller during a compressor disturbance. The aggressive controller regulates superheat to a tighter degree during the compressor disturbance. The detuned controller has slower transients and is not desired for disturbance rejection or reference tracking.
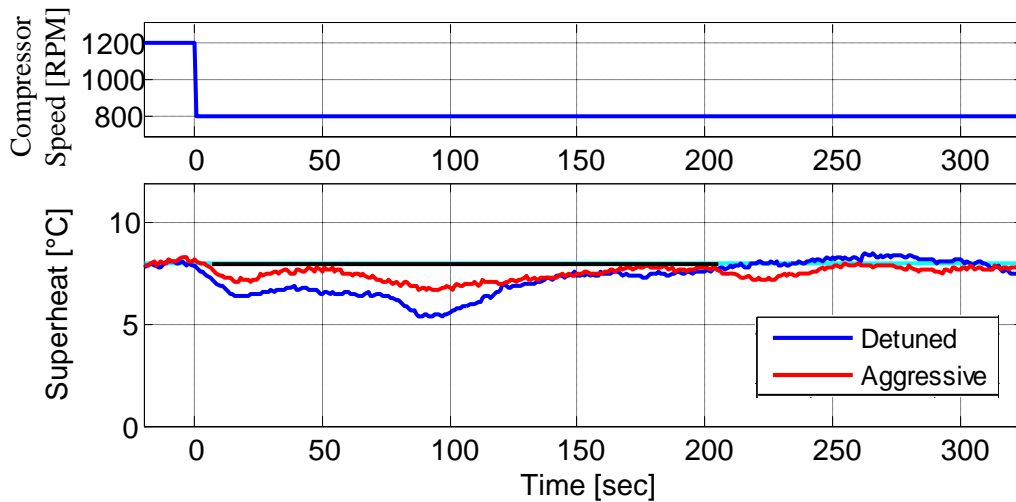

Figure 5.55   Controller disturbance response

The following sections develop a multiple feedback control configuration which combines the benefits of the aggressive and detuned controllers. A filtered approach is first pursued to achieve the desired transient and steady state performance. This method is shown to

be difficult to tune and an error based switching method is then developed to provide the desired performance.

5.7.1 Filtered Feedback Control

A filtered feedback multiple control framework has been designed with two controllers: an aggressive controller and a detuned controller. A low-pass and high-pass filter determines the percentage of aggressive and detuned control efforts. The filtered feedback control framework relies on the tuning of a low pass and high pass filter. The low pass filter is designed to allow the detuned controller to regulate superheat during steady state while the high pass filter is designed to allow the aggressive controller to regulate during transients. The high pass filter is implemented as a band pass filter to eliminate high frequency process and measurement noise from the aggressive feedback path during steady state regulation. Figure 5.56 shows the filtered feedback control configuration.
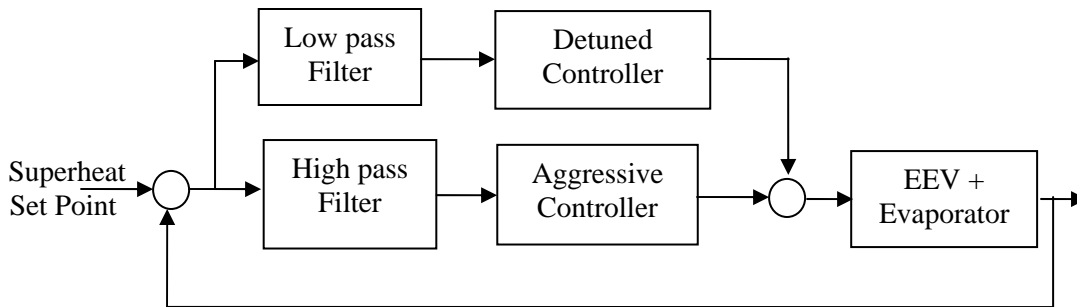

Figure 5.56   Filtered control structure

This control configuration is first developed in a simulation environment using a first order Butterworth filter for both the high pass and low pass filters. The cut-off frequency, ω_c, of each filter is set to be equal to one another to avoid completely attenuating frequency content. Figure 5.57 shows the response of the single detuned controller and the filtered feedback controller during a compressor speed disturbance from 1200 RPM to 800 RPM at 100 seconds. When the cut-off frequency of the filter is set large, the error signal input to the aggressive controller is attenuated to a higher degree making the response similar to the single detuned controller. When the cut-off frequency is set to a smaller frequency, a larger amount of the error signal is passed through the high pass filter to the aggressive controller which decreases the deviation from the set point during the compressor speed disturbance.

124
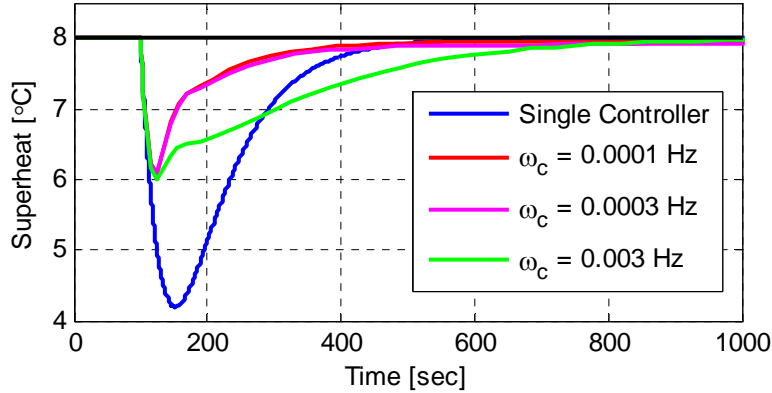
Figure 5.57   Simulation comparison of filtered feedback controller

Figure 5.58 shows the percentage of control effort from the detuned controller during regulation. This figure shows a larger portion of time on the x-axis to show the transients of the control percentage during the compressor speed disturbance. Once the compressor disturbance occurs the aggressive controller begins to contribute to the control signal. With a smaller cut-off frequency the aggressive controller contributes to the overall control signal for a longer period of time following the compressor speed disturbance.
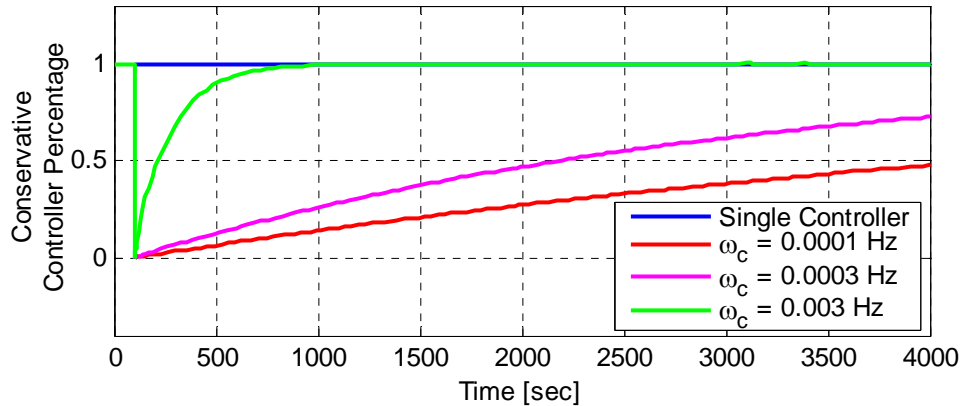

Figure 5.58   Simulation comparison of controller percentages

The filtered feedback concept has been shown to effectively work in the simulation environment. This concept is now implemented on the experimental test stand at the University of Illinois. The cut off frequency of each filter is first designed by analyzing the frequency content of measurement noise and system disturbances. Figure 5.59 shows open loop superheat data collected while running the experimental system in open loop with fixed inputs.
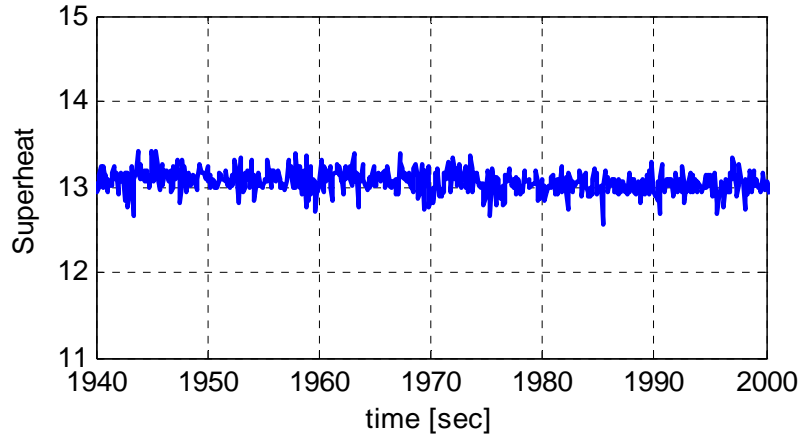
**Figure 5.59   Open loop steady state superheat measurement**

Figure 5.60 shows the frequency spectrum of the steady state superheat signal. The open loop superheat frequency content exhibits white noise characteristics since there is no dominant frequency content. Since there is no dominant frequency at which noise enters the feedback loop it makes it difficult to choose the high cutoff frequency of the band pass filter.
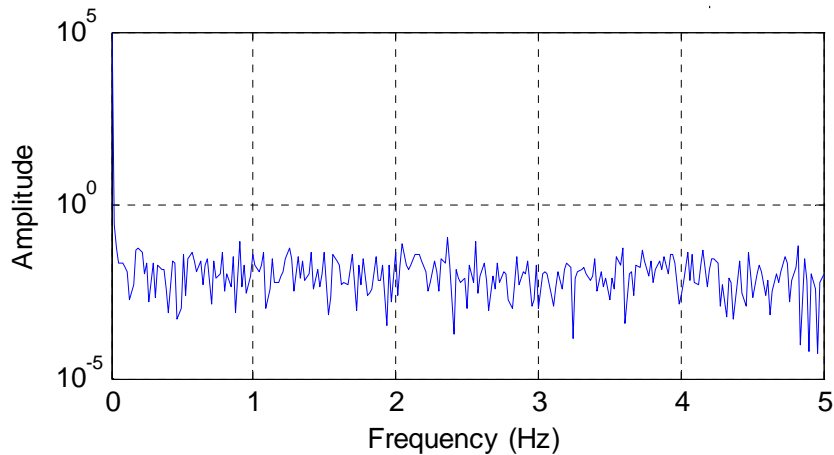
Figure 5.60   Frequency content of steady state superheat measurement

A common disturbance to the superheat control loop is a compressor disturbance. Open loop data is collected where the compressor speed is stepped by 100 RPM as shown in Figure 5.61. The frequency content of a compressor disturbance is determined from the experimental data and shown in Figure 5.62. There is more frequency content close to DC due to the large time constant of the first order response between compressor speed and superheat. Since there is

no dominant disturbance frequency it is difficult to design the cutoff frequency of the high and low pass filters.
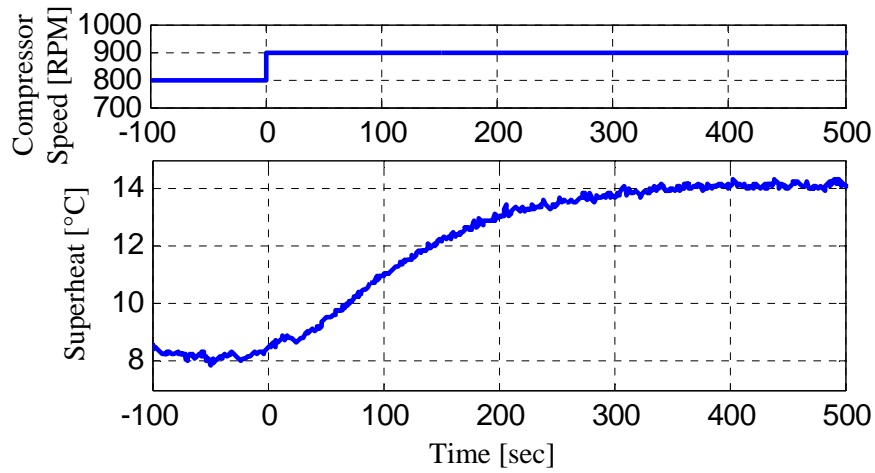
Figure 5.61   Open loop superheat disturbance response
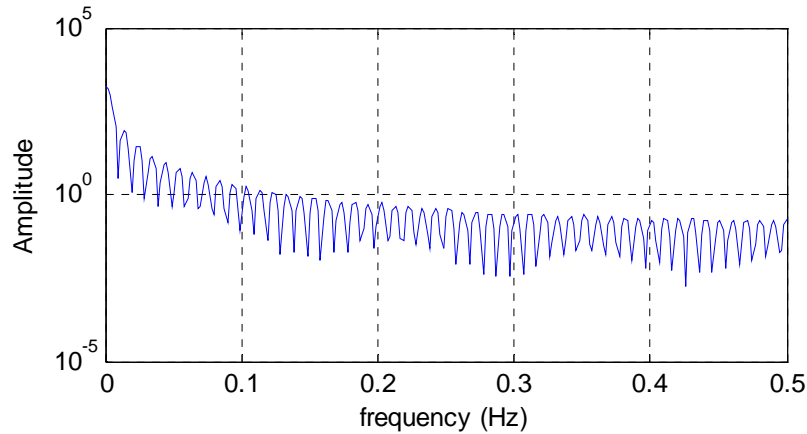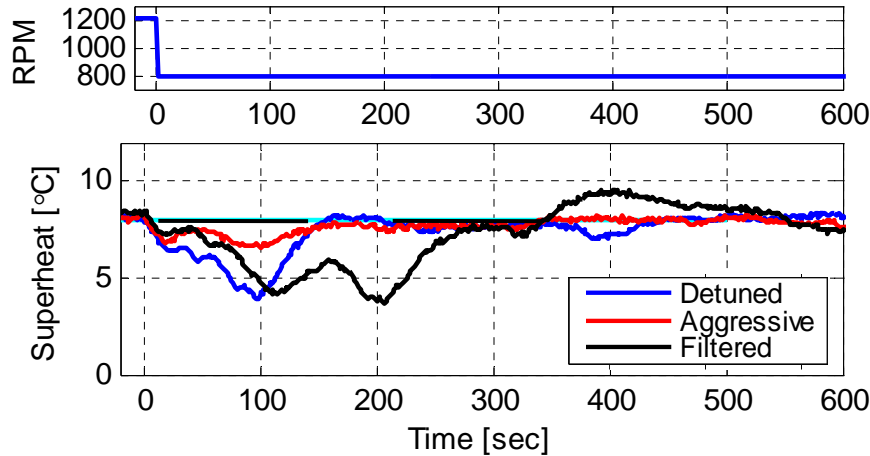

**Figure 5.62   Frequency content of superheat disturbance response**

Nevertheless, the filter parameters are heuristically taken to be 0.08 rad/sec (.012 Hz) for the low pass filter and 0.02 rad/sec (.003 Hz) for the high pass filters. Since it is difficult to choose these cut off frequencies they have been chosen based on simulation results shown in Figure 5.57.

Figure 5.63   Filtered controller performance during compressor disturbance

Figure 5.63 shows the detuned, aggressive, and filtered controller response to a 400 RPM compressor speed disturbance at 0 seconds. Overall, the filtered controller allows superheat to deviate the most of the three controllers to an error of nearly 4°C. The settling time of the filtered controller is also much greater than the detuned and aggressive controller.

Figure 5.64 shows the steady state response of the detuned, aggressive, and filtered controllers. Large oscillations are observed in the superheat measurement during steady state regulation using the filtered feedback controller. Figure 5.65 shows the power spectral density of the valve signal during steady state regulation. The valve signal corresponding to the aggressive and filtered feedback controllers have the largest power spectral density for the range of frequencies shown in Figure 5.76. This indicates that the filtered feedback controller utilizes the valve similar to that of the aggressive controller. In this case, the filtered feedback controller does not show improved steady state superheat regulation.
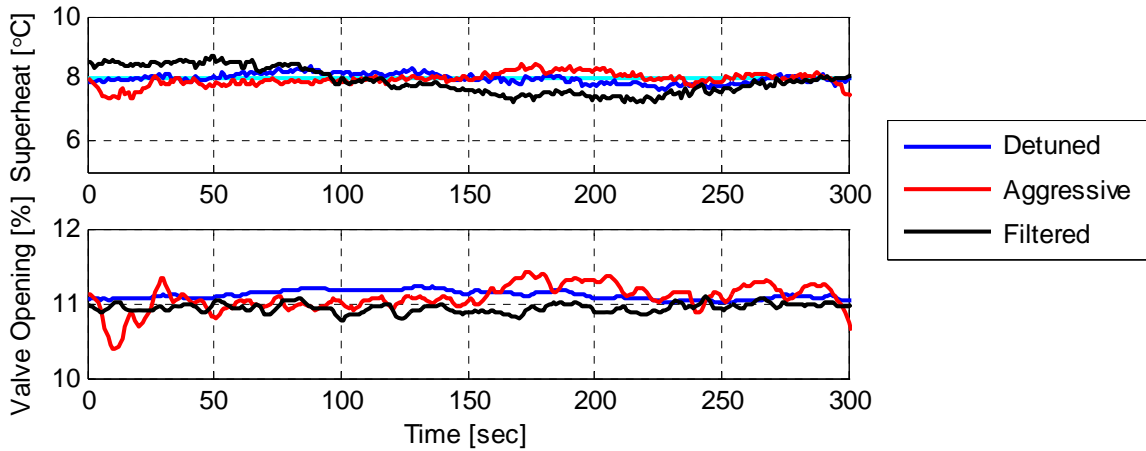
Figure 5.64   Filtered controller steady state performance
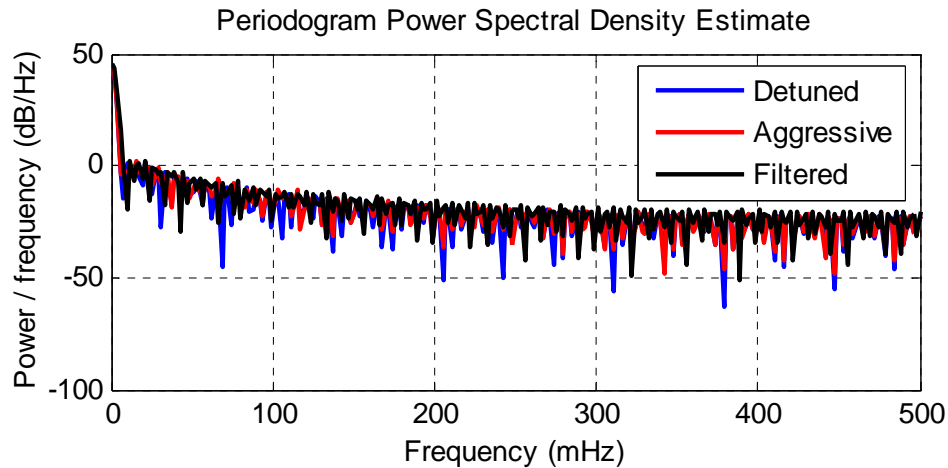
Figure 5.65   Power spectral density of valve opening signal at steady state regulation

Subsequent testing was completed with different filter parameters with the goal of improving the filtered feedback control performance. The testing resulted in similar results as that shown in Figure 5.63 and Figure 5.64. To conclude, the filtered feedback method does not improve superheat regulation due to the difficulty in designing the filters since there is no dominant noise or disturbance frequency. The filtered feedback framework is not recommended for superheat regulation. Therefore, another method is pursued where increased transient and steady state performance is achieved through discrete switching.

5.7.2 Error Based Switching

An error based switching controller is developed where an aggressive and detuned controller are switched between depending on the state of the error between the measured superheat and the desired superheat. This framework does not rely on the performance of any filters and is not subject to the difficulties shown in the previous section. This configuration places an aggressive controller in the feedback loop when the error is larger than a certain threshold and places the detuned controller in the feedback path when the error is smaller than the threshold. The threshold is designed to place the aggressive controller in the feedback loop during large transients that occur during system disturbances. The threshold is also designed to place the detuned controller in the feedback path during steady state regulation.
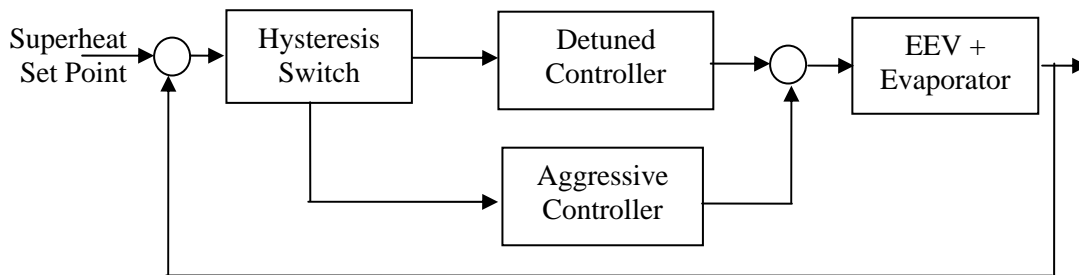
Figure 5.66   Error based feedback control

A hysteresis switching method is implemented to reduce the number of controller switches during a disturbance.   For experimental purposes the switching controller is implemented with an upper hysteresis switching point of 0.4°C. This upper switching point is set to ensure that sensor noise and smaller disturbances do not activate the aggressive controller during steady state regulation. The noise present in feedback path comes from a combination of temperature sensor noise and pressure sensor noise and measures approximately ±0.1°C. An upper hysteresis switching point of 0.4°C ensures that the aggressive controller is not activated during steady state regulation.   The lower hysteresis point is set half as large as the upper switching point to a value 0.2°C. This combination of hysteresis points minimizes the switching between the aggressive and detuned controllers. These hysteresis switching points are also used for the following simulation results.

130

Figure 5.67 shows the response of the switching controller and a detuned controller to compressor speed change from 1200 RPM to 800 RPM at 100 seconds. The simulation environment is developed using the empirical models identified in Chapter 4. In this case the upper hysteresis point is equal to 8°±0.4°C and the lower hysteresis point is equal to 8°±0.2°C. The switching controller does not deviate as far from the set point as the detuned controller. Although, as the superheat is regulated back towards the set point of 8°C, the lower hysteresis switch point of 7.8°C is crossed at 330 seconds. At this time the controller gains discretely switch, causing discontinuity in the control output and therefore in the valve opening. The discontinuity causes the superheat to deviate further from the set point causing the superheat to deviate past the upper hysteresis point of 7.6°C again. When this switching point is crossed the controller gains switch again causing another discontinuity in the valve opening which causes superheat to once again approach the set point and cross the lower hysteresis point of 7.8°C. The controller gains switch once more causing a discontinuous valve command signal which causes superheat to deviate yet again from the set point. This cycle repeats itself causing the oscillation that is observed in Figure 5.67. The superheat eventually settles below the lower hysteresis point at 1100 seconds and tracks the reference with zero error.
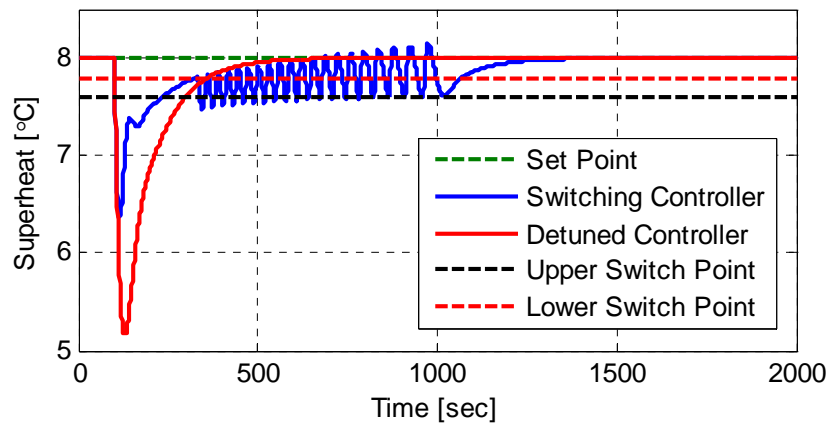
**Figure 5.67   Basic switching controller response**

Figure 5.68 shows the control effort during the disturbance shown in Figure 5.67. There is a considerable discontinuity in the control effort between 240 and 1000 seconds during the time the controller switches between the aggressive and detuned feedback paths. The discontinuity in the control output causes the superheat oscillation and the deviation further from

the set point. A less noticeable discontinuity in valve opening exists at 100 seconds when the aggressive controller is switched to from the detuned controller during the compressor speed disturbance.
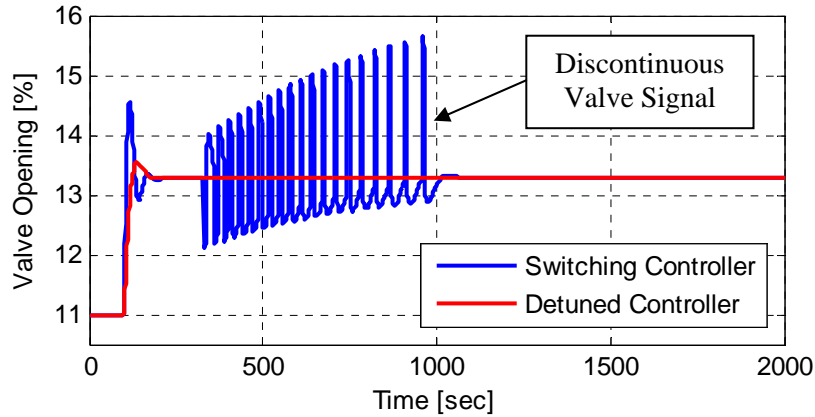
Figure 5.68   Control effort with basic switching

The discontinuous control action during switching is not desirable since it causes oscillation and further superheat deviate from set point. The discontinuous control output may be eliminated by implementing a bumpless transfer scheme [46]. The bumpless transfer scheme forces the aggressive and detuned control outputs to be equal before switching occurs. Specifically a bumpless transfer scheme is implemented to force the output of the *off* controller to have the same output as that of the *on* controller. This is accomplished by influencing the control action of the *off* controller through the integrator. Figure 5.69 shows the bumpless transfer structure where the difference between the output of the *off* controller and the *on* controller is multiplied by a gain and summed with the error on the integrator channel. This forces the output of the *off* controller to be equal that of the *on* controller. The bumpless transfer gain K_{BT} influences how fast the output of the *off* controller tracks the output of the *on* controller. Precise tuning of this gain is not necessary as a gain between 5 and 50 has been found to perform well for superheat regulation.
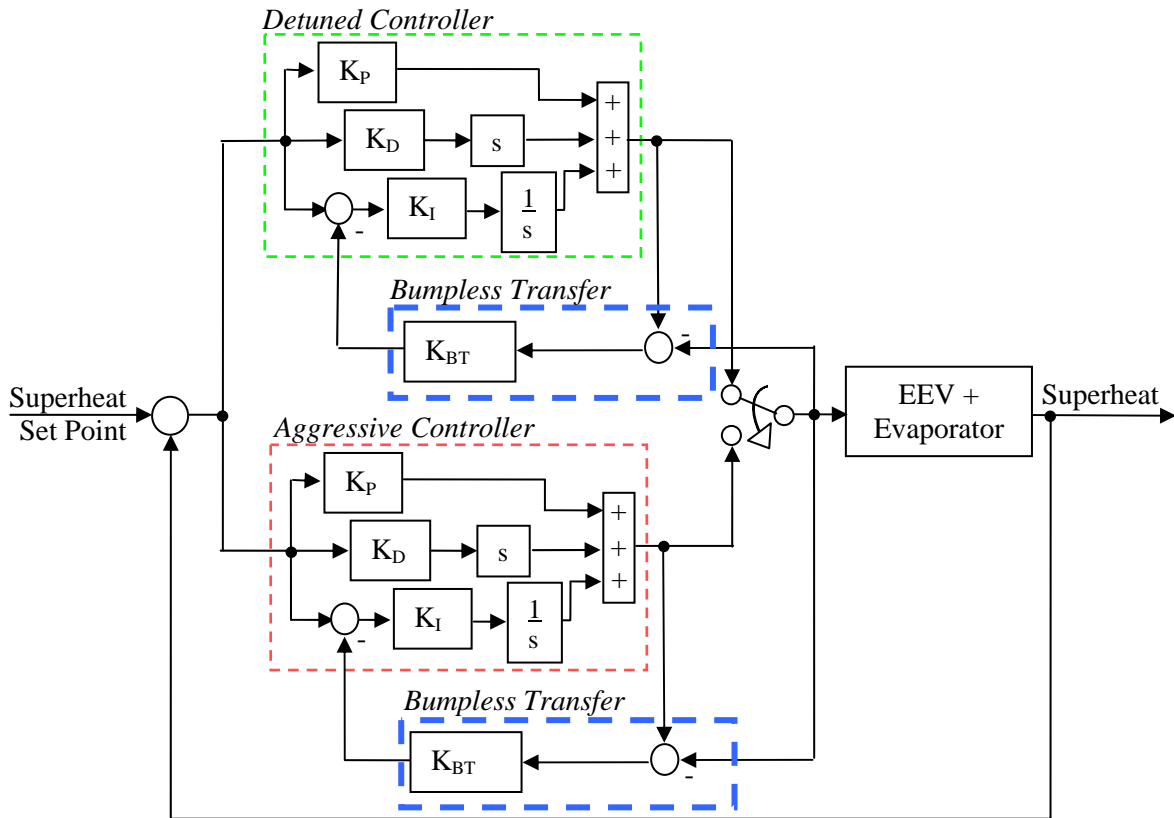
Figure 5.69   Bumpless transfer block diagram

Figure 5.70 shows the control effort of the switching controller and the bumpless transfer switching controller during a compressor speed change from 1200 RPM to 800 RPM at 100 seconds. The switching controller has severe discontinuities in the control effort between 330 and 1000 seconds due to the abrupt switching between the aggressive and detuned controllers. The bumpless transfer switching controller has a smooth transition between the aggressive and detuned controllers.
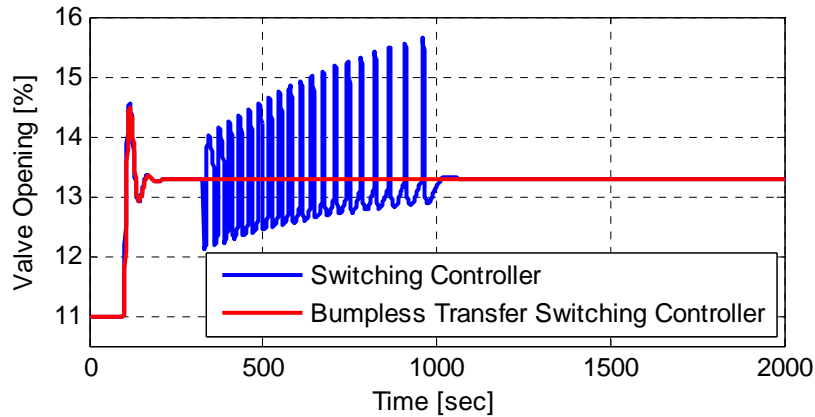
Figure 5.70   Switching and bumpless transfer control efforts

Figure 5.71 shows the response of the error based bumpless transfer switching controller and a detuned controller during a compressor speed fluctuation from 1200 to 800 RPM. The error based bumpless transfer switching controller regulates superheat more precisely compared to the single detuned controller.   The bumpless transfer scheme has eliminated the severe superheat oscillations observed in Figure 5.67 during the control transitions.
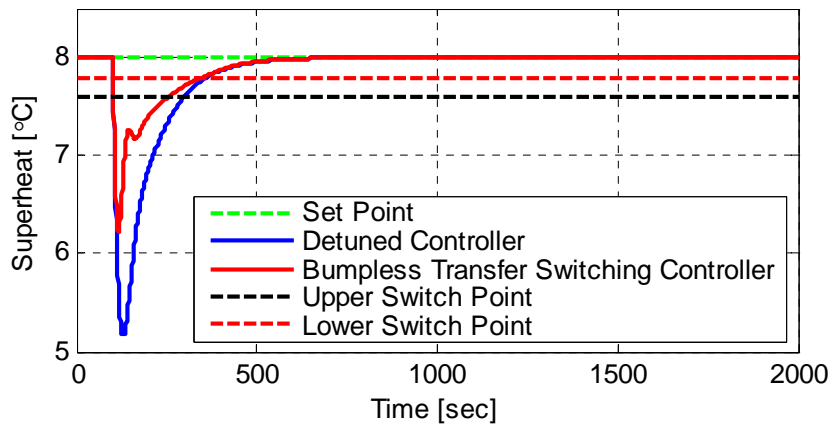
Figure 5.71   Error based feedback disturbance rejection

Figure 5.72 shows experimental results during superheat regulation on the experimental test stand at the University of Illinois. A detuned controller, an aggressive controller, and an error based bumpless transfer switching controller are tested during a compressor speed disturbance from 1200 to 800 RPM. The detuned controller allows superheat to deviate by 2.6°C during the disturbance while the aggressive controller allows superheat to deviate by only 1.3°C.

As expected the switching controller is able to regulate superheat similar to that of the aggressive controller allowing superheat to deviate by 1.5°C. Table 5.7 reports the maximum deviation and root mean squared error for each controller during the compressor speed disturbance. Figure 5.73 visually compares the maximum deviation of each controller during the compressor speed disturbance.
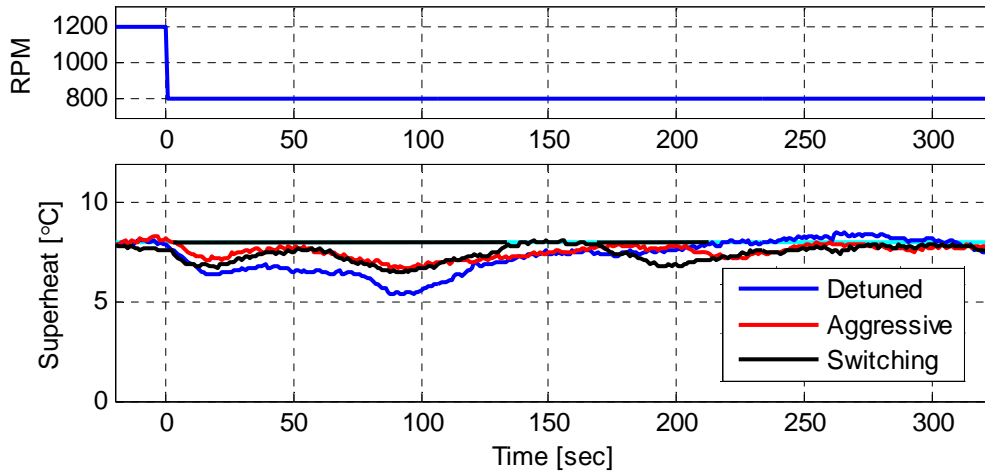
Figure 5.72   Controller response to a decrease in compressor speed

Table 5.7   Error based switching controller disturbance performance

	Detuned	Aggressive	Switching
Maximum Deviation	2.6°C	1.3°C	1.5°C
Root Mean Squared Error	0.82°C	0.42°C	0.35°C
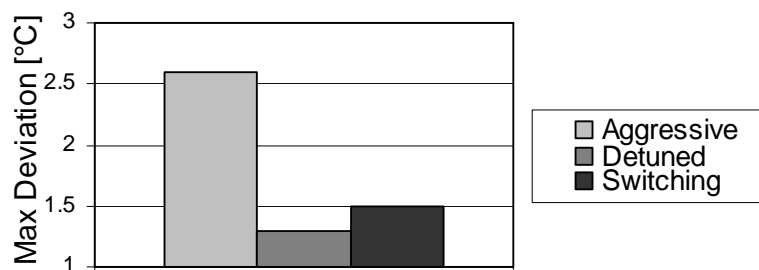
Figure 5.73   Transient performance

Figure 5.74 shows the response of the aggressive, detuned, and error based bumpless transfer switching controller to an increasing compressor speed disturbance. A similar trend is

135

observed in this response where the detuned controller allows superheat to deviate by a large amount. The aggressive controller precisely regulates superheat while the switching controller allows superheat to deviate slightly more than that of the aggressive controller and less than the detuned controller.
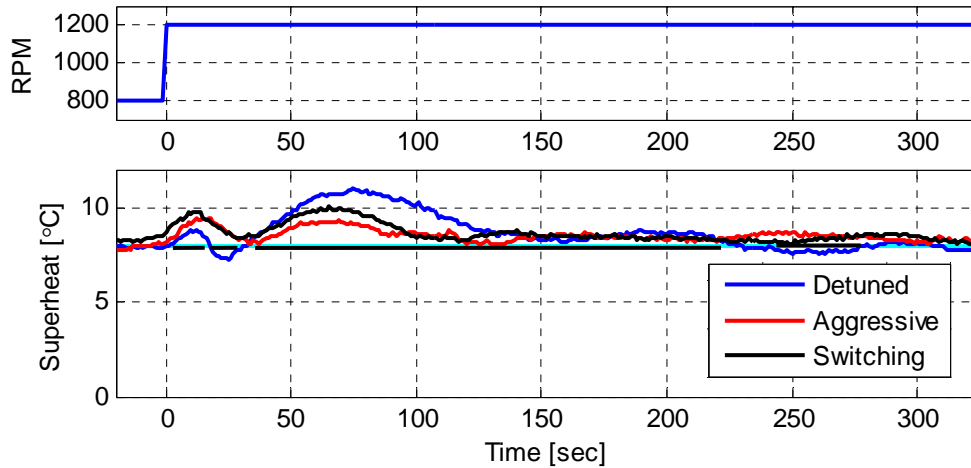
Figure 5.74   Compressor speed increase disturbance

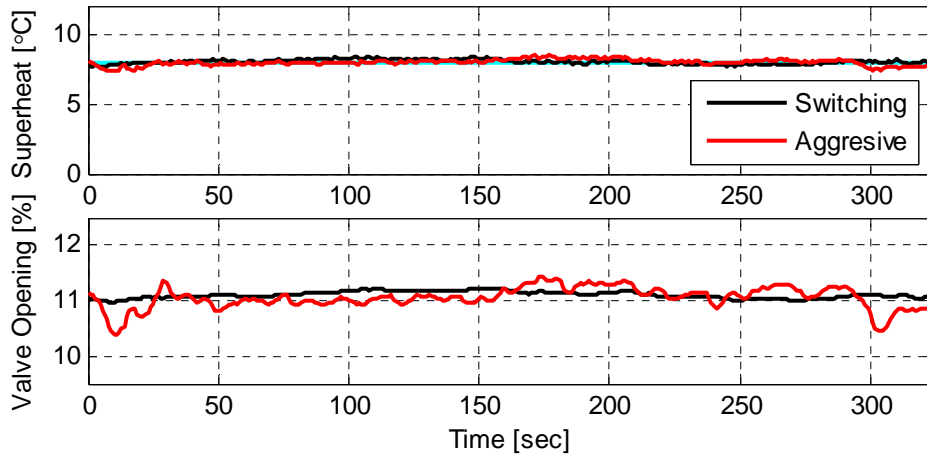Figure 5.75 shows the superheat and valve opening signals during steady state regulation. The detuned controller is not shown in Figure 5.75 since the switching controller allows the detuned controller to regulate at steady state since the error is within the defined thresholds. It is clear that both controllers equally regulate superheat to the set point during steady state operation. However, the main difference is noticeable while observing the control effort. The switching controller lightly utilizes the valve during steady state regulation which improves the valves lifetime. During the same regulation scenario the aggressive controller heavily utilizes the valve. Figure 5.76 shows the power spectral density of the valve signal during steady state regulation. The valve signal corresponding to the switching type multiple feedback controller has a smaller power spectral density for the range of frequencies shown in Figure 5.76. This indicates that the switching type multiple feedback controller utilizes the valve to a lesser degree than the aggressive controller during steady state regulation.

Figure 5.75   Steady state controller performance
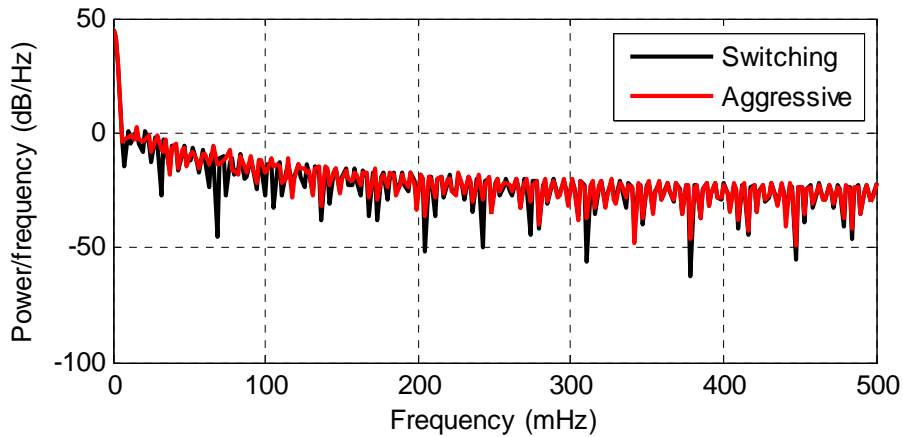
Figure 5.76   Power spectral density of valve opening signal at steady state regulation

The standard deviation of the valve signal and the root mean squared error of the superheat during steady state regulation are shown in Table 5.8. Figure 5.77 visually compares the standard deviation of the valve signal for each controller. The root mean squared error of the superheat signal during steady state regulation is comparative for both the switching controller and the aggressive controller. The standard deviation of the valve actuation for the aggressive controller is 3 times as large as that of the switching controller.

Table 5.8   Steady state comparison

	Switching	Aggressive
Valve Actuation Standard Deviation	0.06	0.19
Superheat Root Mean Squared Error	0.14	0.21
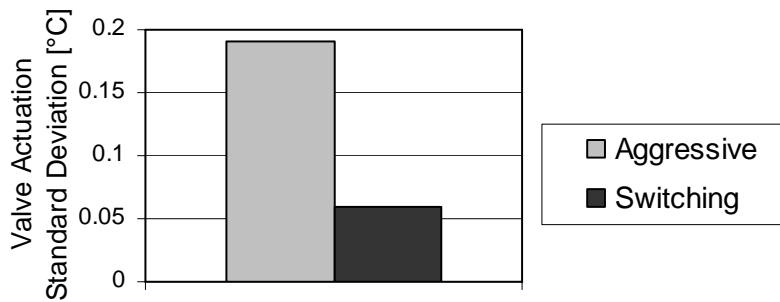
Figure 5.77   Steady state valve actuation comparison

The reduced valve actuation of the switching controller ultimately allows for improved valve life. The switching type multiple feedback configuration has the best of both worlds, the transients of an aggressively tuned controller while having the steady state performance of a conservatively tuned controller.

5.8   Superheat control during start up

This section describes a control configuration that has been developed to regulate superheat during system startup. This controller has been developed to ensure superheat is not lost during on-off load emulation. During system start up this algorithm first opens the valve to a preset position of 13% for a time period of 15 seconds. A bumpless transfer scheme is used to ensure smooth transitioning between the preset valve position of 13% and the PID superheat controller after the time period of 15 seconds has elapsed. This superheat control method is implemented during on-off temperature control and shown in Figure 5.78. While the system is turned from *off* to *on* the superheat controller positions the valve to 13% for the first 15 seconds. During this time the superheat rises to nearly 20°C. After 15 seconds has elapsed the PID controller is engaged and modulates the valve opening based on the error signal. When the system is turned *off* the valve is completely shut to help maintain the high and low side pressure. Further improvements may be made to improve tracking performance and are discussed in the

future research section in Chapter 7. The performance of this controller is adequate for the on-off load emulation testing.
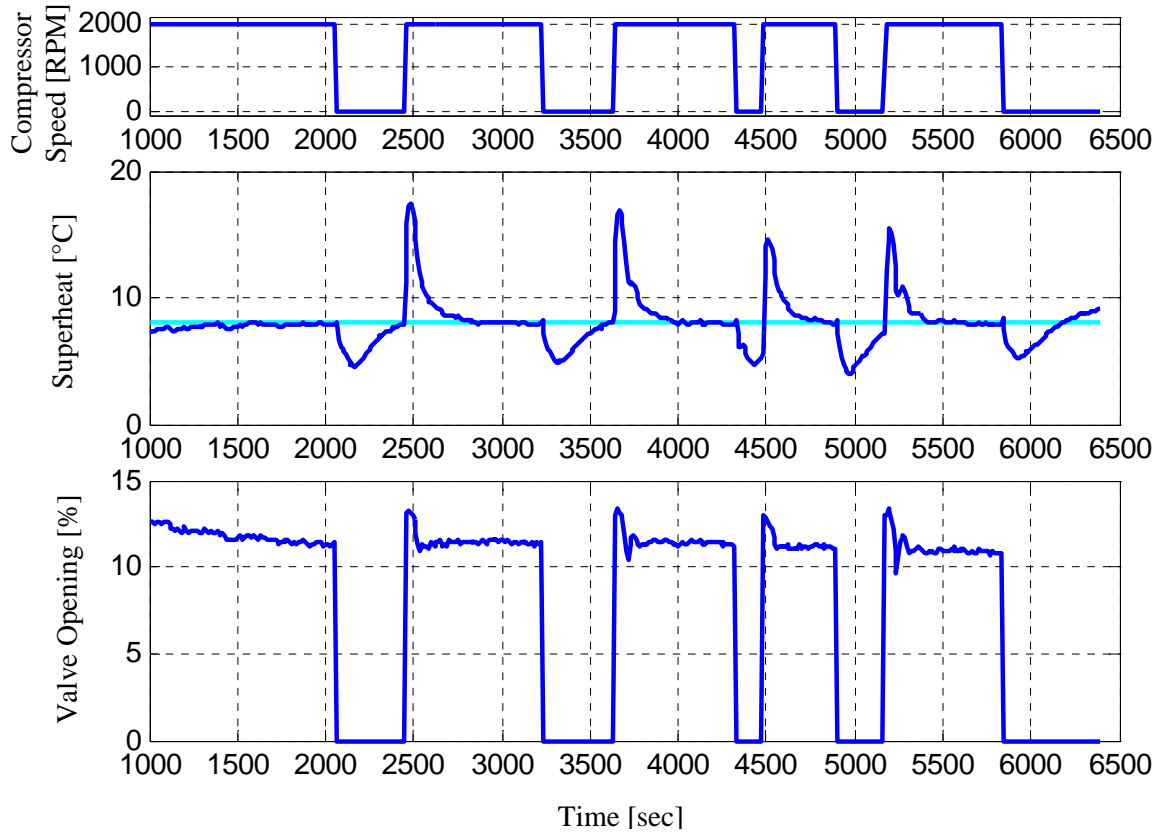
Figure 5.78   Superheat control during startup

5.9   Superheat Control Discussion

This chapter has presented the various control methods that have been investigated through the efforts of this research. These methods have been shown to improve the performance of superheat regulation for different AC&R applications. Table 5.9 presents the advantages and requirements for the control features developed in this chapter.

Table 5.9   Control summary

Control Type	Advantages	Requirements
Scheduled Feedforward	Improves disturbance rejection	Accurate system model
Gain-scheduled Feedback	Improves system-wide stability and performance	Accurate system model
Error Based Switching	Fast transient response while minimizing steady state valve actuation – improved valve life	Tuning of two controllers

It is important for the system designer to consider each control method based on the AC&R application since some of the developed control configurations may significantly improve performance while others may be of little benefit. The control methods presented in this chapter have been designed to supplement the PID control loop for additional performance. A combination of the presented control features may be used in parallel with the PID controller depending on the application. Overall, this chapter has presented various control methods which improve superheat regulation to ultimately improve system efficiency through a low superheat set point.
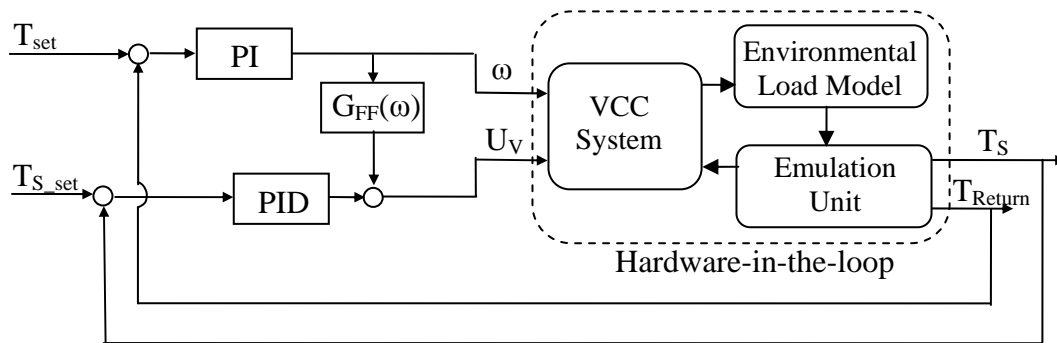
Chapter 6

Controller Validation

This chapter validates the superheat control configurations developed through this research. The developed controllers are subjected to common disturbances experienced in the field by air conditioning and refrigeration systems. Hardware-in-the-loop load emulation is used as a means to place representative disturbances on the experimental system while the developed control algorithms are analyzed. This chapter begins with the investigation of the scheduled feedforward superheat controller while virtually cooling a truck environment. In this case, the system is subjected to a change in temperature set point (a common system disturbance) and the performance of the superheat control loop is observed. Section 6.2 investigates the multiple feedback control configuration to a similar system disturbance. This chapter does not consider the analysis of the gain scheduled feedback control configuration developed in Chapter 5 since the experimental system does not undergo large dynamic variations over the small range of inlet air temperatures that are experimentally attainable during load emulation on the experimental test stand at the University of Illinois. Overall, this chapter validates the superheat control configurations developed in Chapter 5 while also demonstrating the flexibility of hardware-in-the-loop load emulation.

6.1 Scheduled Feedforward Control Validation

The scheduled feedforward compensator is implemented on the experimental system at the University of Illinois while virtually cooling a mid size truck environment through hardware-in-the-loop load emulation. The performance of the superheat control loop is considered during a change in temperature set point which represents a common disturbance that the end user may

frequently subject the system to. The temperature set point may depend on user comfort, types of cooled goods, the state of a manufacturing process, etc.

Scheduled feedforward control of superheat is configured with hardware-in-the-loop load emulation as shown in Figure 6.1. In this scenario, the compressor speed is used to control the container temperature and the electronic expansion valve is used to control the evaporator superheat. For the results shown in this chapter the compressor control loop is tuned heuristically to obtain acceptable temperature tracking performance. A heuristic method is sufficient for tuning the temperature control loop since this controller needs only to regulate the virtual container temperature to allow the superheat control loop to be analyzed.

Figure 6.1 **Scheduled feedforward load emulation control configuration**

The scheduled feedforward superheat control loop is subjected to a step change in desired container temperature from 14°C to 16°C. As discussed in Chapter 5, the feedforward mapping depends on both the compressor speed and the evaporator inlet air temperature. The results shown in Chapter 5 consider a constant evaporator inlet air temperature of 25°C for development purposes. In this testing scenario the virtual container is cooled to 15°C. Equation 6.1 shows the form of the feedforward compensator where the two dynamic models depend on compressor speed and the inlet air temperature. Figure 6.2 shows the feedforward gain as a function of compressor speed for an inlet air temperature of 25°C and 15°C where the two curves have different slopes. For the feedforward results shown in this chapter the lower curve corresponding to 15°C evaporator inlet air temperature is implemented since the inlet air temperature fluctuates between 14°C and 16°C. If the temperature during operation fluctuates a large amount, a mapping that accounts for both compressor speed and inlet air temperature may be implemented to preserve the performance of the feedforward control structure.

142

$$G_{FF} = \frac{T_S}{\omega}\left(\frac{T_S}{U_V}\right)^{-1} = \frac{-M_\omega(\omega)\cdot(90s+1)}{M_V(T_I)\cdot(95s+1)} \qquad (6.1)$$
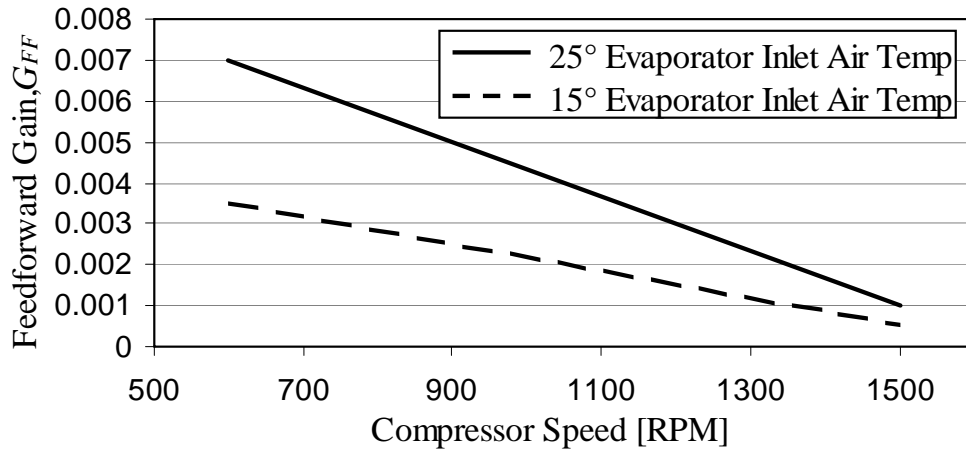
Figure 6.2   Inlet air temperature feedforward mapping

Hardware-in-the-loop load emulation is used to test the feedforward controller to a step change in set point temperature as shown in Figure 6.3. In response to the change in set point temperature the compressor speed initially decreases and briefly settles to the lower constraint of 500 RPM. This constraint is set to prevent the compressor from running at extremely slow speeds. As the compressor speed decreases the virtual load temperature begins to increase due to the decreased amount of cooling by the vapor compression system. The strong system coupling causes superheat to vary during this abrupt change in compressor speed.   The scheduled feedforward compensator prevents a large deviation in superheat, whereas the feedback only controller allows superheat to deviate substantially, risking compressor damage. The root mean squared (RMS) error and maximum deviation of evaporator superheat are calculated for this response and displayed in Table 6.1. The scheduled feedforward control framework reduces RMS error and the maximum deviation by a factor of 3 during this disturbance. Figure 6.4 visually compares the maximum deviation of the feedback and the scheduled feedforward controllers. Not only does this result validate the scheduled feedforward control method, it also demonstrates the usefulness of hardware-in-the-loop load emulation during controller development.
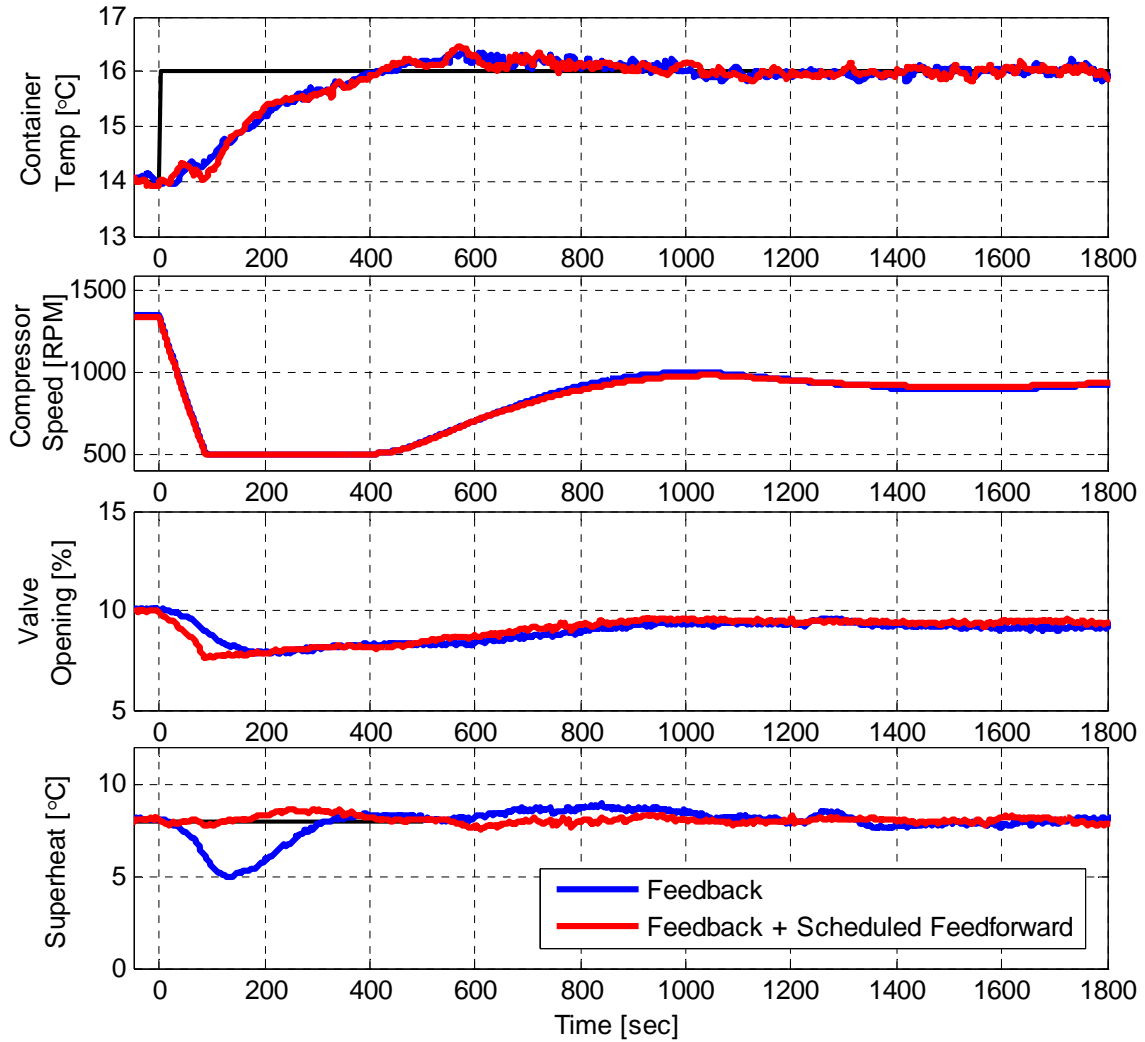
Figure 6.3   Performance comparison between feedback and scheduled feedforward control during increasing temperature load emulation

Table 6.1   Superheat tracking comparison between feedback and scheduled feedforward compensation during an increasing temperature load emulation

	Feedback Only	Scheduled Feedforward
RMS error [°C]	0.96°C	0.23°C
Max. Deviation [°C]	3.13°C	0.66°C
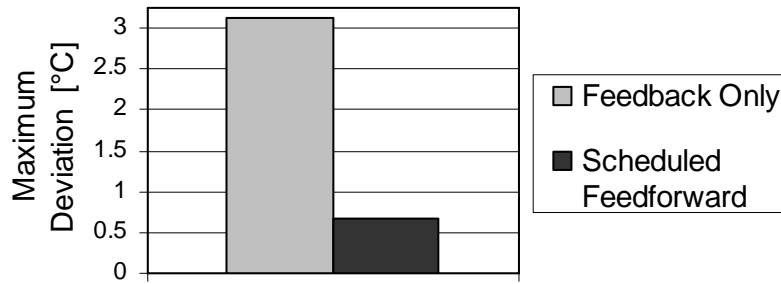
Figure 6.4   **Comparison of maximum deviation during temperature set point change**

To ensure controller performance, a step decrease from 16°C to 14°C in set point temperature is tested as shown in Figure 6.5. During the change in temperature set point the compressor speed rapidly increases to the upper constraint of 2000 RPM which is the limit set by the compressor manufacturer. As the compressor speed increases the supply air temperature decreases and the virtual load is cooled. The scheduled feedforward controller regulates superheat closer to the set point when compared to that of the feedback only controller. Table 6.2 shows the RMS error and maximum deviation during this test. Figure 6.6 visually compares the maximum deviation of the feedback and the scheduled feedforward controller. The scheduled feedforward controller has a significantly smaller maximum deviation and RMS error. This result validates the performance of the scheduled feedforward superheat controller during an abrupt compressor speed increase.

Figure 6.5   **Performance comparison between feedback & scheduled feedforward control during a decreasing temperature load emulation**
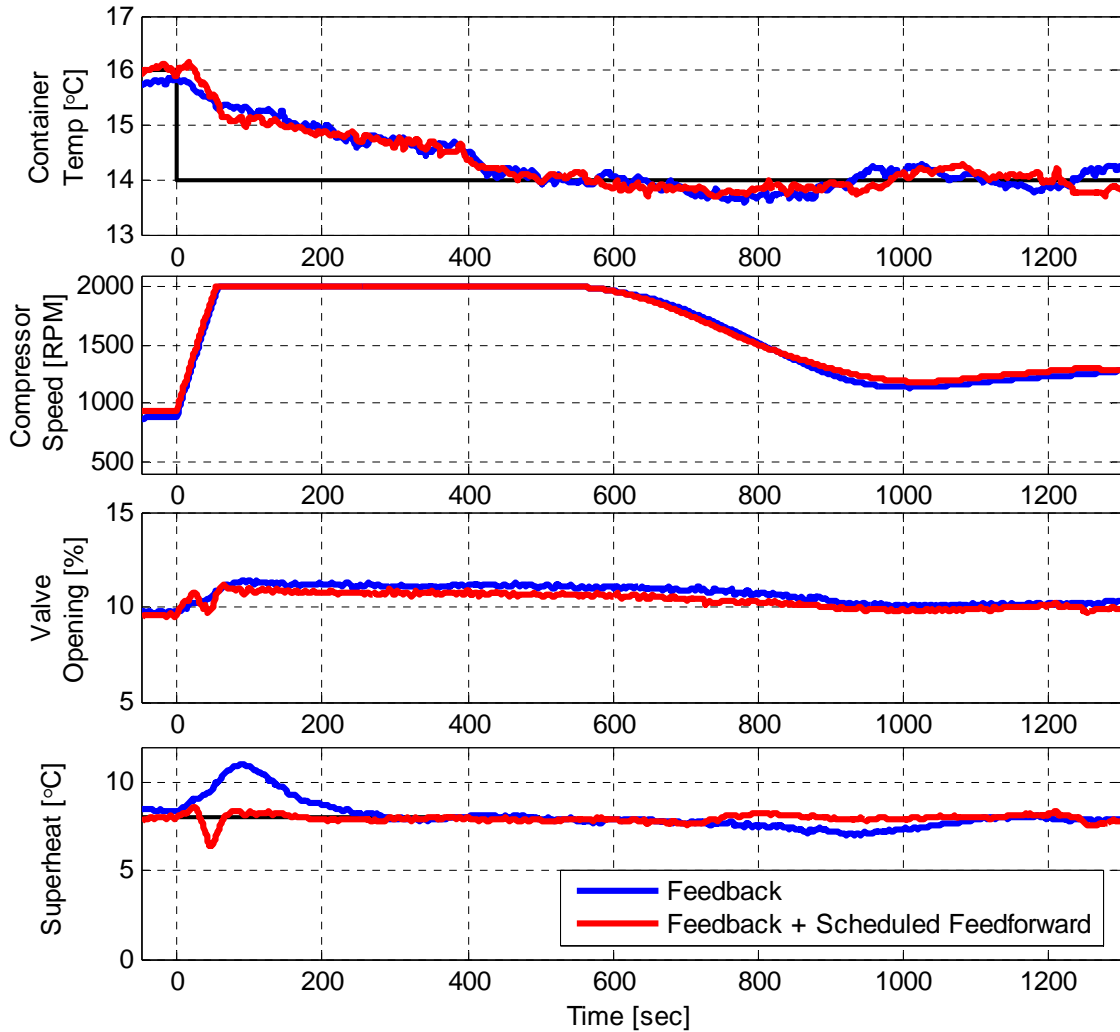
Table 6.2   **Superheat tracking comparison between feedback and scheduled feedforward compensation during a decreasing temperature load emulation**

	Feedback Only	Scheduled Feedforward
RMS error	0.82°C	0.24°C
Max. Deviation	3.05°C	1.60°C

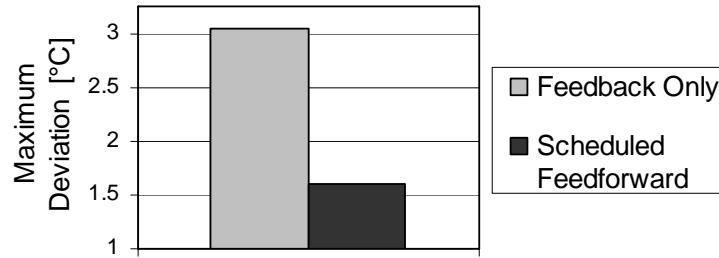**Figure 6.6   Comparison of maximum deviation during temperature set point change**

6.2   Multiple Feedback Control Validation

Similarly, the multiple feedback control configuration is implemented on the experimental test system at the University of Illinois while virtually cooling a mid size truck environment through hardware-in-the-loop load emulation. The performance of the multiple feedback control configuration is analyzed during the response to a step change in the desired container temperature. Details of the multiple feedback control configuration may be found in Chapter 5.

The multiple feedback controller is configured with hardware-in-the-loop load emulation as shown in Figure 6.7. In this scenario, the virtual container temperature is controlled via a proportional-integral control loop acting on the compressor speed. The proportional-integral controller is heuristically tuned to achieve stability to allow for the analysis of the superheat control loop. The expansion valve opening is controlled via the multiple feedback control configuration to regulate evaporator superheat.
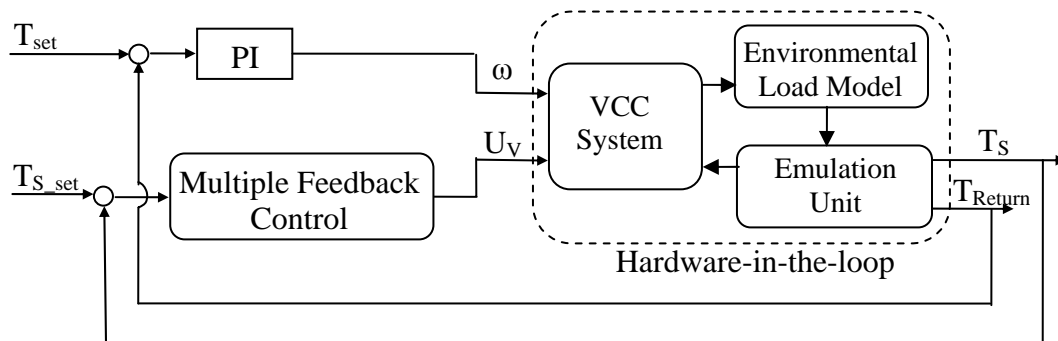
Figure 6.7   Multiple feedback load emulation control configuration

147

Figure 6.8 shows the multiple feedback control configuration regulating superheat while undergoing a change in temperature set point from 14°C to 13°C. Following the decrease in temperature set point the compressor speed immediately increases to cool the virtual container. The superheat response to the change in temperature set point of the aggressive, detuned, and switching type multiple feedback control configurations are shown in Figure 6.8. The transient performance of these controllers is quantitatively reported in Table 6.3. The aggressive controller allows superheat to deviate the least, while the detuned controller allows the superheat to deviate by nearly 2 times as much. The switching type multiple feedback controller allows superheat to deviate slightly more than the aggressive controller but considerably less than the detuned controller. Figure 6.9 visually compares the maximum superheat deviation of the detuned, aggressive, and switching type multiple feedback controller.
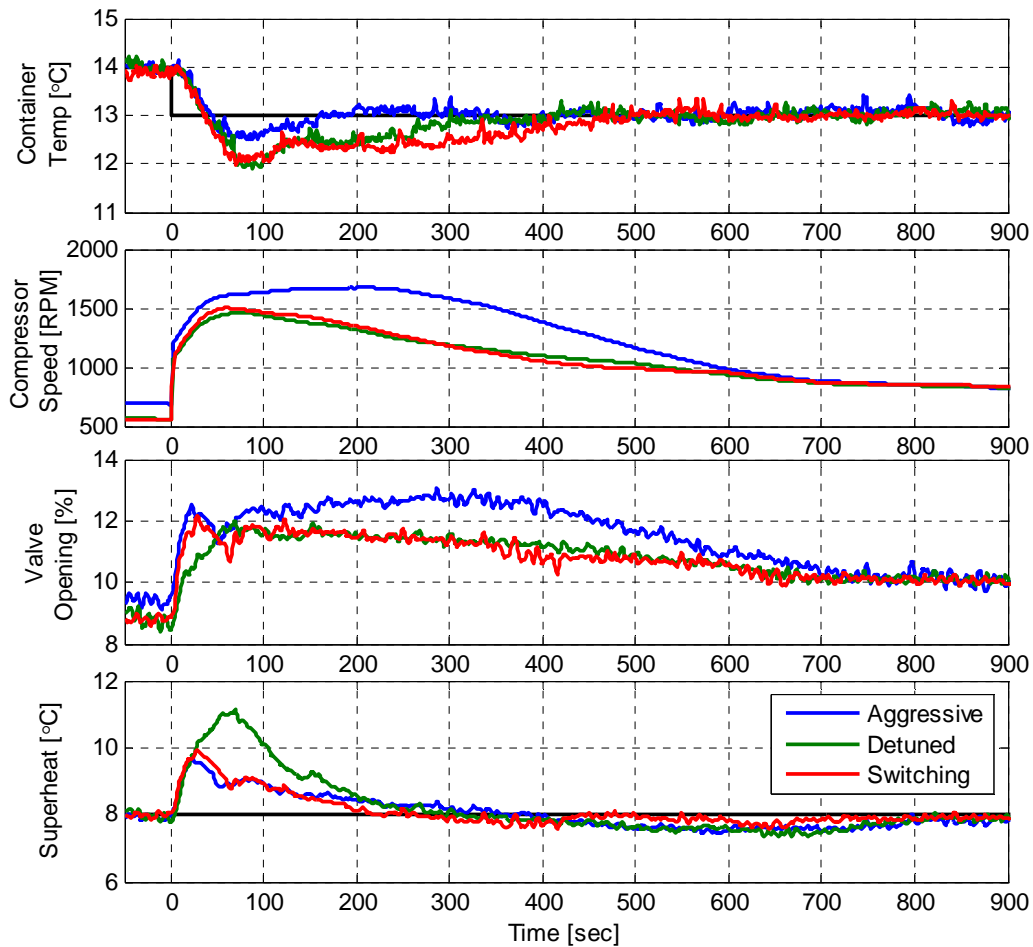
Figure 6.8 **Performance comparison of multiple feedback control configuration during a decreasing temperature load emulation**

148

Table 6.3   Transient superheat performance

	Aggressive	Detuned	Switching
Superheat RMS error	0.56°C	1.10°C	0.58°C
Superheat Max. Deviation	1.71°C	3.13°C	1.95°C
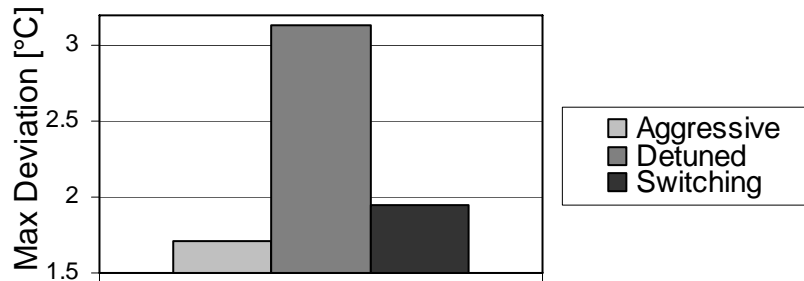
Figure 6.9   Comparison of maximum deviation during temperature set point change

Table 6.4 shows the steady state performance of the aggressive, detuned, and switching type multiple feedback control configurations. Each type of controller regulates superheat within a tight band during steady state regulation. However, a difference in the valve actuation is observed where the aggressive controller heavily utilizes the valve at steady state, and the detuned controller and switching controller conservatively actuate the valve at steady state. Therefore, the switching type multiple feedback control configuration has been shown to exhibit the transients (good disturbance rejection) of an aggressive controller and the steady state performance (minimal steady state valve actuation) of a detuned controller.

Table 6.4   Steady state performance

	Aggressive	Detuned	Switching
Standard Deviation of Valve Actuation [°C]	0.39	0.22	0.23
Valve Range	±0.82%	±0.45%	±0.55%
Superheat Max. Deviation [°C]	0.56	0.65	0.41
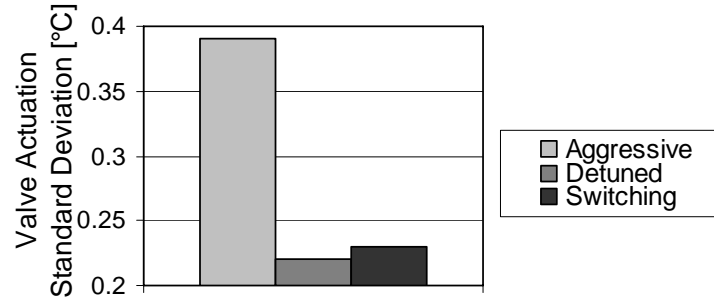
Figure 6.10   Steady state valve actuation comparison

6.3   Conclusion

This chapter validates some of the superheat controllers developed in Chapter 5 with the use of hardware-in-the-loop load emulation. This chapter serves to provide two main results. First, the superheat controllers developed in Chapter 5 are validated to realistic system disturbances. The scheduled feedforward method was shown to substantially eliminate the deviation of evaporator superheat from set point during a change in temperature set point during superheat regulation on a variable speed system. The multiple feedback control configuration was also shown to have improved transient performance and improved steady state performance while regulating superheat. Furthermore, this chapter demonstrates the flexibility which hardware-in-the-loop load emulation provides in terms of testing system and software control loop performance – such as that for superheat regulation.

Chapter 7

Conclusions and Future Work

7.1 Summary of Research Contributions

The research presented in this thesis makes contributions in two distinct areas. First, this thesis provides thorough insight into superheat control design for an array of air conditioning and refrigeration applications. The designed controllers have been developed to allow implementation in a modular fashion to fit the needs of the particular application at hand. Second, this work presents the development of hardware-in-the-loop load emulation for the testing of vapor compression systems. This method provides an alternative method for testing air conditioning and refrigeration systems and has been shown to be an effective technique to validate system controllers.

7.1.1 Superheat Control Design

This thesis makes contributions to the advancement of superheat control design. The nonlinear dynamics of the vapor compression cycle have been investigated experimentally and a sufficient understanding of the nonlinear relationships has been achieved to allow for controller design. A gain scheduled feedback controller has been designed to allow the feedback control loop to maintain stability and performance over system-wide operating conditions. A nonlinear scheduled feedforward controller has also been developed through this research to reduce the strong coupling effects inherent to the vapor compression cycle between compressor speed and superheat. Also, a multiple feedback control framework has been developed which is able to avoid the common performance vs. robustness tradeoff. The mentioned superheat control

frameworks have been shown throughout this thesis to improve superheat regulation. The superheat control features developed through this work may be used to supplement the commonly used PID controller. Depending on the application, a number of the developed control features may be implemented to improve superheat regulation performance. Ultimately, these control features allow the superheat set point to be set to a low level for increased efficiency.

7.1.2 Hardware-in-the-Loop Load Emulation

Hardware-in-the-loop (HIL) load emulation has been demonstrated by accurately enforcing a virtual load on an air conditioning and refrigeration system through a real-time simulation environment and an experimental emulation unit. This thesis shows that this alternative testing method may be used to investigate the performance of the physical AC&R system unit along with the software control loops. The development of this testing method is explained in detail in Chapter 3. In Chapter 6, hardware-in-the-loop load emulation has been used to replicate realistic system disturbances to validate the superheat control configurations developed in Chapter 5. While the hardware-in-the-loop load emulation approach is not a replacement for full scale environmental test chambers, it has been demonstrated that it may provide a valuable method to test preliminary performance of AC&R systems. This would then reduce the use of and reliance on expensive and time-consuming test chambers.

7.2 Future Work

The results shown in this thesis reveal a number of potential avenues for continued research. The most significant of these include the following.

7.2.1 Superheat Control

This thesis investigates many methods of superheat control. However, the results shown in Chapter 5 only briefly touch on superheat control during startup. In literature there have been few efforts which investigate superheat control during system startup. This is partly due to the difficulty to identify the dynamics at system startup since the refrigerant mass typically accumulates in certain components. One possible method to control superheat at startup might

include the investigation of an iterative learning approach. A controller such as this may be extremely useful for on-off system due to the repetitive nature.

7.2.2 Hardware-in-the-Loop Load Emulation

The hardware-in-the-loop load emulation results shown in the thesis demonstrate the usefulness of such a method. However, there exist a number of potential improvements and other possible research paths. One important feature that will enable future research is the addition of a device that controls the humidity of the inlet air to the evaporator. Currently the humidity is not controlled; rather it is determined by the central air conditioning system of the Mechanical Engineering Laboratory. The ability to control the inlet air humidity may increase the accuracy of the load emulation results. With humidity control, research efforts could focus on determining the frost build up rate at different evaporator coil temperatures or different inlet air temperatures. For example, it may be found that designing a controller to avoid certain coil temperatures may reduce the rate of frost buildup. Different control frameworks may also be investigated to determent the best method to defrost the evaporator.

Also, the addition of a second emulation unit on the condenser side during testing would increase the accuracy of the load emulation test by making it more realistic. An emulation unit attached to the condenser side of the system would allow the inlet temperature to the condenser to be experimentally controlled. The condenser inlet air temperature would ideally be controlled to the ambient temperature of the simulated conditions. Consider this case; a load emulation test is being completed where the simulated load is a truck environment in an ambient temperature of 80°F. Ideally the condenser air inlet temperature would be controlled to 80°F since this is temperature that the condenser would be subjected to while in the actual environment. In the current configuration, the condenser inlet air temperature is not controllable. The addition of an emulation unit on the condenser side would make load emulation more representative of the actual environmental conditions.

Another possible improvement to hardware-in-the-loop load emulation would be the redesign of the emulation unit itself to linearize the input/output relationship between blade angle and inlet air temperature. The current configuration has a strong nonlinear exit flow profile as shown in the computational fluid dynamic analysis performed in Chapter 4. A computational

fluid dynamic analysis such as this may aid in redesigning the emulation unit to ensure a uniform air flow profile at the outlet. Reducing the nonlinear flow profile of the outlet air may potentially simplify the blade angle control loop and allow for improved temperature tracking performance.

Another design consideration would be the addition of detachable insulation to the outer surface of the emulation unit. Insulation such as Styrofoam sheets would be ideal for this since they may be easily fastened to the exterior when needed, while being easily removable for other testing scenarios. The additional insulation is needed for certain low temperature load emulation testing to decrease the heat transfer rate between the emulation unit and surrounding environment.

Another potential research path that hardware-in-the-loop load emulation may examine is the investigation of the interactions between multiple zones. A second emulation unit may be placed on the second evaporator on the experimental system located at the University of Illinois. A simulation environment may be constructed to virtually account for the heat transfer between the two zones. For example, each emulation unit could virtually represent a single floor in a two level office building. The heat transfer between the two levels would be accounted for in the simulation environment where the emulation unit would then place the corresponding load on the respective evaporator. A configuration such as this would allow for the development of controllers (such as a superheat controller) to account for the coupling between the evaporators/floors.

7.2.3 Multiple Evaporator Systems

Past research efforts have investigated control methods for multiple evaporator systems. These studies typically investigate systems with three or fewer evaporators. However, systems with upwards of 10 evaporators are becoming feasible and are not uncommon in Europe and Asia [47]. Systems with a large number of evaporators such as this are referred to as variable refrigerant flow (VRF) systems. There are numerous studies in literature which investigate the efficiency of these systems comparing them to water chiller loops [48].

One potential investigation could examine how the degree of coupling between the evaporators of a VRF system is influenced by the number of evaporators. Many studies have determined that there is strong coupling in systems with two or three evaporators. However,

there is no study which investigates the coupling between a large number of evaporators as that seen in VRF systems. Research may be completed to determine what scenarios a single-input single-output control structure is sufficient and when a multi-input multi-output framework needed to account for system coupling.

List of References

[1] Goodwin, B.K., Grennes, T.J., and Craig, L.A., "Mechanical Refrigeration and the Integration of Perishable Commodity Markets," *Explorations in Economic History*, vol. 39, no. 2, pp. 154-182, 2002.

[2] "Residential Energy Consumption," http://www.eia.doe.gov/consumption/, 2010.

[3] Hua, L., Jeong, S.-K., and You, S.-S., "Feedforward Control of Capacity and Superheat for a Variable Speed Refrigeration System," *Applied Thermal Engineering*, vol. 29, no. 5-6, pp. 1067-1074, 2008.

[4] Keir, M., Rasmussen, B.P., and Alleyne, A., "Improving Energy Efficiency in Automotive Vapor Compression Cycles through Advanced Control Design," in *SAE 2006 World Congress and Exposition*, Detroit, MI.

[5] Changenet, C., Charvet, J.N., Gehin, D., Sicard, F., and Charmel, B., "Study on Predictive Functional Control of an Expansion Valve for Controlling the Evaporator Superheat," *Systems and Control Engineering*, vol. 222, no. 1, pp. 571-582, 2008.

[6] Qureshi, T.Q. and Tassou, S.A., "Variable-Speed Capacity Control in Refrigeration Systems,"16, no. 2, pp. 103-113, Feb, 1996.

[7] Rasmussen, B.P. and Alleyne, A.G., "Stable Gain-Scheduling on Endogenous Signals," in *2005 American Control Conference*, vol. 3, 2005, pp. 1895-1900.

[8] Rasmussen, B.P. "Thermosys Toolbox User's Manual," http://mr-roboto.me.uiuc.edu/thermosys, 2005.

[9] Li, B. and Alleyne, A., "A Full Dynamic Model of a HVAC Vapor Compression Cycle Interacting with a Dynamic Environment," in *American Control Conference*, St. Louis, MO.

[10] Lu, B., Wu, X., Figueroa, H., and Monti, A., "A Low-Cost Real-Time Hardware-in-the-Loop Testing Approach of Power Electronics Controls," *IEEE Transactions on Industrial Electronics* , vol. 54, no. 2, pp. 919-931, Apr, 2007.

[11] Isermann, R., Schaffnit, J., and Sinsel, S., "Hardware-in-the-Loop Simulation for the Design and Testing of Engine-Control Systems," *Control Engineering Practice*, vol. 7, pp. 643-653, 1999.

[12] ASHRAE Handbook: Fundamentals, Chapter 30. In: Anonymous Atlanta, GA: American Society of Heating, Refrigerating, and Air-Conditioning Engineers, 2005.

[13] Rasmussen, B.P., "Dynamic Modeling and Advanced Control of Air Conditioning and Refrigeration Systems," Dept. of Mechanical and Industrial Engineering, University of Illinois, Urbana, IL, Dec. 2005.

[14] Chia, P.K., Tso, C.P., Jolly, P.G., Wong, Y.W., and Jia, X., "Fuzzy Control of Superheat in Container Refrigeration using an Electronic Expansion Valve," *HVAC&R Research*, vol. 3, no. 1, pp. 81-98, 1997.

[15] Finn, D.P. and Doyle, C.J., "Control and Optimization Issues Associated with Algorithm-Controlled Refrigerant Throttling Devices," in *2000 ASHRAE Winter Meeting,* vol. 106

[16] Aprea, C. and Renno, C., "Experimental Analysis of a Transfer Function for an Air Cooled Evaporator," *Applied Thermal Engineering*, vol. 21, pp. 481-493, 2001.

[17] P. Mithraratne and N.E. Wijeysundera, "An experimental and numerical study of hunting in thermostatic-expansion-valve-controlled evaporators," *International Journal of Refrigeration*, vol. 25, no. 7, pp. 992-998, 2002.

[18] Cengel, Y. and Boles, M. Thermodynamics An Engineering Approach, New York, NY: McGraw-Hill, 2006.

[19] Long, J., inventor. Control for Refrigeration Systems. US. Patent no. 3577743, 1971.

[20] Gruhle, W.D. and Isermann, R., "Modeling and Control of a Refrigerant Evaporator," *ASME Journal of Dynamic Systems Measurement & Control*, vol. 107, no. 4, pp. 235-240, Dec, 1985.

[21] Ohya, S. and Ohta, H., inventors. System for Controlling Flow Rate of Refrigerant. US. Patent no. 4674292, 1987.

[22] Parkum, J. and Wagner, C., "Identification and Control of a Dry-Expansion Evaporator," in *IFAC System Identification*, Copenhagen, Denmark, 1994.

[23] Jolly, P.G., Tso, C.P., Chia, P.K., and Wong, Y.W., "Intelligent Control to Reduce Superheat Hunting and Optimize Evaporator Performance in Container Refrigeration," *HVAC&R Research*, vol. 6, no. 3, pp. 243-255, Jul, 2000.

[24] Li, X., Chen, J., Chen, Z., Liu, W., Hu, W., and Liu, X., "A New Method for Controlling Refrigerant Flow in Automobile Air Conditioning," *Applied Thermal Engineering*, vol. 24, pp. 1073-1085, 2004.

[25] Lin, J. and Yeh, T., "Modeling, Identification and Control of Air-Conditioning Systems," *International Journal of Refrigeration*, vol. 30, pp. 209-220, 2007.

[26] Elliott, M., Shenoy, B., and Rasmussen, B., "A Control Architecture Solution to Superheat Nonlinearity," in *American Control Conference*, Baltimore, MD, 2010.

[27] Tingrui, L., Guangqing, C., and Jidai, W., "Autocontrol of Electronic Expansion Valve Based on Optimal Fuzzy PD Controller," in *Second International Conference on Genetic and Evolutionary Computing*, Hubei.

[28] Seem, J., "A New Pattern Recognition Adaptive Controller with Application to HVAC Systems," *Automatica*, vol. 34, no. 8, pp. 969-982, 1998.

[29] Gruhle, W. and Isermann, R., "Modeling and Control of a Refrigerant Evaporator," *Journal of Dynamic Systems, Measurements, and Control*, vol. 107, pp. 235-240, Dec, 1985.

[30] Hewitt, N.J., Mcmullan, J.T., Murphy, N.E., and Ng, C.T., "Comparison of Expansion Valve Performance," *International Journal of Energy Research*, vol. 19, pp. 347-359, 1995.

[31] Rasmussen, H., "Nonlinear Superheat and Capacity Control of a Refrigeration Plant," in *17th IEEE International Conference on Control Applications*, Antonio, TX.

[32] Ohya, S. and Ohta, H., inventors. System for Controlling Flow Rate of Refrigerant. US. Patent no. 4674292, 1987.

[33] Chen, Y., Chen, J., Reifel, A., and Koesterer, D., inventors. System and Method for Controlling an Air Conditioner or Heat Pump. US. Patent Application 20080216500.

[34] Schmidt, F., inventor. Method for Controlling the Superheat Temperature of the Refrigerant in an Evaporator Arrangement of a Refrigeration System or Heat Pump System, and a Device for Implimenting the Method. US. Patent no. 6018959.

[35] Matsuoka, A., Honda, Y., and Takagi, M., inventors. Refrigeratin System. US. Patent no. 4807445, 1989.

[36] Beckey, T. and Nelson, L., inventors. Adaptive Refrigerant Control Algorithm. US. Patent no. 4848099, 1989.

[37] Jessen, L., inventor. Controller and a Method for Controlling an Expansion Valve of a Refrigeration System. US. Patent no. 6854285, 2005.

[38] Sibik, L., Leaver, D., and Goshaw, C., inventors. Feed Forward Control of Expansion Valve. US Patent no. 5632154, 1997.

[39] Lord, R., inventor. Mehtod and Apparatus for Controlling a Refrigerant Expansion Valve in a Refrigeration System. US. Patent no. 4523435, 1985.

[40] Schmidt, F., inventor. Control Arrangement for the Superheat Temperature of at Least One Evaporation of a Refrigeration System. US. Patent no. 5782103, 1998.

[41] Satoshi Ohya, O., Hiroshi Taniguchi, O., and Hiroshi Tamayama, O., inventors. Refrigerating Apparatus and Method of Controlling Refrigerating Apparatus in Accordance with Fuzzy Reasoning. US. Patent no. 5259210, 1993.

[42] Toshihiko Fukushima, I., Seigo Miyamot, K., Kosaku Sayo, K., and Kenji Emi, K., inventors. Refrigerant Flow Control Device. US. Patent no. 4617804, 1986.

[43] Franklin, G., Powel, J., Emami-Naeini, A., Anonymous. Feedback Control of Dynamic Systems, New Jersey: Prentice Hall, 2006.

[44] Skogestad, S., "Probably the Best Simple PID Tuning Rules in the World," in *AIChE Annual Meeting*, Reno, NV, Nov. 2001.

[45] Liu, G. and Daley, S., "Optimal-Tuning PID Control for Industrial Systems," *Control Engineering Practice*, vol. 9, no. 11, pp. 1185-1194, Nov, 2001.

[46] Peng, Y., Vrancic, D., and Hanus, R., "Anti-Windup, Bumpless, and Conditioned Transfer Techniques for PID Controllers," *IEEE Control Systems*, vol. 16, no. 4, pp. 48-57, Aug, 1996.

[47] Amarnath, A. and Blatt, M., "Variable Refrigerant Flow: Where, Why, and How," *Engineering Systems*, vol. pp. 54-60, Feb, 2008.

[48] Goetzler, W., "Variable Refrigerant Flow Systems," *ASHRAE Journal*, vol. pp. 52-55, Apr, 2007.